Cyclist Drag Reduction through the Manipulation of the 3D Flow Topology

An investigation by means of numerical simulations and robotic volumetric PTV

Master of Science Thesis

H.M. van der Waals

TU Delft

Cyclist Drag Reduction through the Manipulation of the 3D Flow Topology

An investigation by means of numerical simulations and robotic volumetric PTV

by

H.M. van der Waals

to obtain the degree of Master of Science
at the Delft University of Technology,
to be defended publicly on Monday October 9, 2023 at 13:30 PM.

Student number:	4437322	
Project duration:	October 31st, 2022 - October 9th, 2023	
Thesis committee:	Prof. Dr. S. Hickel	TU Delft, chair of the assessment committee
	Dr. A. Sciacchitano	TU Delft, supervisor
	Dr. W. Terra	TU Delft, daily supervisor
	Dr. D. Ragni	TU Delft, committee member

An electronic version of this thesis is available at http://repository.tudelft.nl/.

TU Delft

Preface

Achieving performance in sports through aerodynamic optimization is something that has become a passion of mine over the past couple of years. This passion started during the year between my BSc. and MSc. Together with an incredible team, we developed an extremely efficient solar car named NunaX with which we participated in the World Solar Challenge in Australia. For my internship during my MSc, I worked with another great team at Mercedes F1, contributing to the development of the CFD simulations. For this thesis, I was very happy to be given the opportunity by Andrea and Wouter to study again sports aerodynamics.

Something I have enjoyed is the combination of the many aspects of aerodynamic research that this thesis has included. The development of drag reductions in cycling, both numerically and experimentally, has given me insight into the many elements that such a problem consists of. Moreover, this project has taught me a great deal about the significance of both methods and how each can complement the other in aerodynamic development. Finally, this project has allowed me to study a sport that I find both interesting and enjoyable.

For this incredible opportunity and their guidance throughout the project, I would like to thank Dr. Andrea Sciacchitano and Dr. Wouter Terra. I would like to express my gratitude to both for their great advice and help with the realization of this project.

I would like to thank Peter Duyndam, Frits Donker Duyvis, and Dennis Bruikman for their help with the development of the wind tunnel setup. With their help, we have been able to successfully run the wind tunnel experiment.

Then, I would also like to thank Domas, Victor, Tim, Bruno, Maxime, Emie, and Josée for their help with the preparation and running of the wind tunnel experiment. Finally, I would like to thank my friends and family for their help, support, and encouragement during this project.

H.M. van der Waals
Delft, September 2023

Abstract

The importance of aerodynamic efficiency in the cycling sport is well known. Simple calculations demonstrate the considerable impact of just a few percentages in drag savings on the outcome of a competition where the margins can be incredibly small. Achieving a drag reduction can, however, be challenging as the flow topology of a cyclist is extremely complex. Nonetheless, the manipulation of flow structures in other research areas is proven to be an effective method for reducing aerodynamic resistance. Hence, the potential of achieving a drag reduction for a cyclist in a time trial position through the manipulation of the 3D flow topology is investigated.

Two devices are introduced named the Hip Vortex Control (HVC) and wingsuit aiming to reduce the streamwise vorticity at the hips and upper arms respectively. A reduction of a crosswind-dependent weighted drag area of -1.35% for the HVC and -5.45% for the wingsuit is measured experimentally. RANS simulations and robotic volumetric PTV provide the trends in the drag-reducing mechanisms. The HVC promotes separation on the lower back of the cyclist, reducing the presence of the hip vortices leading to an increase of the pressure on the lower back. The wingsuit limits the formation of the streamwise vortices around the upper arms, slightly increasing the wake and increasing the pressure on the upper arms resulting in the drag reduction.

The numerical and experimental results largely agree on the variations in the flow topology for each configuration. The results indicate that a reduction in streamwise vorticity in the wake of a bluff body can reduce the drag considerably. Both devices lead to an expansion of the wake which should be kept to a minimum to effectively reduce the drag. The results motivate the continuation of the research into the reduction of streamwise vortices in the development of cycling equipment and in other high-velocity sports.

Contents

List of Tables

List of Figures

Nomenclature

Abbreviations

Abbreviation	Definition
CAD	Computer-aided Design
CFD	Computational Fluid Dynamics
CVV	Coaxial Volumetric Velocimetry
DES	Detached Eddy Simulation
FDM	Fused Deposition Modeling
GCM	Generic Cyclist Model
HB	Handlebar
HFSB	Helium-Filled Soap Bubbles
HTM	Homogeneous Transfer Matrix
HVC	Hip Vortex Control
IPR	Iterative Particle Reconstruction
LDA	Laser Doppler Anemometry
LES	Large Eddy Simulation
LHS	Left Hand Side
LPT	Lagrangian Particle Tracking
MDF	Medium Density Fibreboard
PIV	Particle Image Velocimetry
PLA	Polylactide
PTV	Particle Tracking Velocimetry
RANS	Reynolds Average Navier-Stokes
RHS	Right Hand Side
RMS	Root-Mean-Square
RP	Rapid Prototyping
STB	Shake-The-Box
TT	Time-trial
UCI	Union Cycliste Internationale

Symbols

Symbol	Definition	Unit
β	Tomographic aperture	[°]
Γ	Circulation	[m^2/s]
ϵ_u	Uncertainty of velocity u	[m/s]
ϵ_F	Uncertainty of drag force	[N]
θ	Crank angle	[°]
λ	Wavelength	[nm]
ρ	Density	[kg/m^3]
σ_u	Velocity standard deviation	[m/s]
$\mathbf{\Omega}$	Vorticity tensor	[1/s]
ω	Vorticity	[1/s]
A	Reference area	[m^2]
A_n	Area between four nozzles	[cm]
b	Bit depth	[-]

Symbol	Definition	Unit
C	Contour	[m]
C_D	Drag coefficient	[-]
C_{HFSB}	Bubble concentration	[bubbles/cm^3]
C_p	Pressure coefficient	[-]
C_X	Force coefficient in x-direction	[-]
C_Y	Force coefficient in y-direction	[-]
c	torso length	[m]
D	Drag	[N]
d_{y_n}	Horizontal distance between two nozzles	[cm]
d_{z_n}	Vertical distance between two nozzles	[cm]
F	Acquisition Frequency	[Hz]
F_x	Drag force	[N]
f_i	Focal length	[mm]
$f_\#$	Camera aperature	[-]
I_p	Particle image intensity	[W/m^2]
L	Measurement domain	[m]
M	Magnification factor	[-]
$\dot{N}$	Nozzle bubble rating	[bubbles/s]
P_{aero}	Power losses to aerodynamic forces	[W]
P_f	Power output to mechanical losses and friction	[W]
P_T	Total power out	[W]
p	Static pressure	[N/m^2]
p_t	Total pressure	[N/m^2]
p_∞	Free-stream static pressure	[N/m^2]
Q	Q-criterion	[1/s^2]
R	Rotation matrix	[rad]
Re	Reynolds number	[-]
r	Digital image resolution	[pixels/mm]
$\mathbf{S}$	Strain rate tensor	[1/s]
S	Closed surface	[m^2]
T	Translation vector	[mm]
U_∞	Free-stream velocity	[m/s]
U_w	Wind speed	[m/s]
u	Velocity component along x-direction	[m/s]
$\vec{u}$	Velocity vector	[m/s]
$\dot{V}$	Volume flow rate	[cm^3/s]
v	Velocity component along y-direction	[m/s]
w	Velocity component along z-direction	[m/s]
w_j	Weight factor	[-]
y^+	Dimensionless wall distance	[-]
z_{max}	Maximum object distance for CVV	[mm]
z_{min}	Minimum object distance for CVV	[mm]

1

Introduction

Cycling aerodynamics reveals itself to be a complex topic. There are countless variables affecting the aerodynamic performance of a cyclist. Flow structures appear abundantly in the wake of a cyclist resulting in turbulent flows which can be challenging to measure both numerically and experimentally. Nonetheless, the correct characterization of this wake can act as an effective framework for aerodynamic optimization. In the past, this has shown to be successful in a wide variety of applications. In Formula 1 for example, engineers optimize the car's aerodynamic performance for maximum downforce through careful manipulation of the flow topology. Whilst in aircraft design, minimizing the drag results in large amounts of fuel savings benefiting both the cost and carbon emissions. And, in sports aerodynamics, a lower drag coefficient could be the deciding factor in becoming a world champion.

The essence of aerodynamics in cycling is best illustrated with an example. For a 40 km time-trial stage, like stage 20 of the 2022 Tour de France, it is found that a 2% reduction in drag area would result in finishing the stage 20 seconds earlier[1]. Moreover, the time difference between the first and second place was only 19 seconds indicating the relevance of achieving just a 2% improvement in aerodynamic efficiency.

The velocity at which professional cyclists ride has gradually increased since the introduction of the sport. Reaching an average velocity of 40 km/h for a stage spanning more than 150 km during a professional cycling tour is not unusual. More importantly, research shows that the aerodynamic drag[2] in cycling can reach 90% of the total resistance force (Grappe et al., 1997; Kyle and Burke, 1984). With the increasing capability of aerodynamic research in finding more information on flow features, flow mechanisms, and their effect on the aerodynamic forces it has become both feasible and favorable for cycling teams to further optimize their aerodynamic performance.

Over the years, more effort has gone into the development of aerodynamic efficient frames, wheels, and bike positions. However, all of these elements are also regulated by the UCI[3], the international governing body for cycling sports. This influences, for example, the freedom engineers have in designing the bike's frame. Nonetheless, for this thesis, it was decided to leave the UCI regulations to the side and focus on generating a broader understanding of drag-reduction methods in cycling.

The literature discusses the topological flow features in the wake of a cyclist (Crouch et al., 2014; Griffith et al., 2014; Terra et al., 2020; among others). Crouch et al., 2014 discuss that it is expected that flow mechanisms have a great impact on the overall drag force experienced by a cyclist. More importantly, Crouch et al., 2014 mention a variation in the drag coefficient of 15% which is attributed to the varying 3D flow topology as a result of a changing crank position. Although Crouch et al., 2014

[1] The full derivation of this example can be found in Appendix A.

[2] Hereafter referred to as drag

[3] The UCI oversees all international cycling competitions like the World Championships. It also regulates these events.

discuss the effect of a changing flow field and its effect on drag, the manipulation of the flow topology to achieve drag reductions has not been investigated. This poses a gap in the available research. To contribute to this knowledge gap the focus of this thesis will be to evaluate the possibility of achieving drag reductions through the manipulation of the near wake flow structures. This leads to the following research objective.

To evaluate the potential of achieving drag reductions by manipulating the near-body 3D flow topology of a cyclist in time trial position by means of numerical simulations and robotic volumetric PTV

The report is set out as follows. First, chapter 2 discusses the background of the 3D flow topology of a cyclist as is examined in the literature. Then, chapter 3 explains the methodology behind the proposed drag reduction methods and the flow visualization techniques. Next, the setup of the numerical simulations is discussed in chapter 4. This is followed by chapter 5, which explains the experimental setup. Next, the results are discussed in chapter 6. Finally, the conclusions and recommendations are given in chapter 7.

2

Theoretical Background on the 3D Flow Topology of a Cyclist

Characterizing the complex flow field in the wake of a cyclist is challenging and time-consuming. Nonetheless, several encouraging attempts have been made. An analysis of these flow structures and their contribution to the drag is discussed in this chapter providing a general overview of the flow field of a cyclist. First, the definition of aerodynamic drag and methods to characterize flow structures are discussed. Then, an overview of the available literature on the 3D flow topology of a cyclist is given. Next, the flow field is compared to other research fields to explore and analyze existing drag reduction methods. This is followed by a discussion on the effect of vorticity on the surface pressure distribution contributing to the drag. Then, a brief description of the benefits of a generic cyclist model is provided. The chapter concludes with the research questions for this thesis.

2.1. Definitions of aerodynamic drag and flow structures

The definition of aerodynamic drag and its relation with the flow mechanisms will be discussed before discussing the flow field of a cyclist. The equation for aerodynamic drag is given in Equation 2.1.

$$D = \frac{1}{2}\rho U_{\infty}^2 A C_D \tag{2.1}$$

In this equation, $\frac{1}{2}\rho U_{\infty}^2$ is referred to as the dynamic pressure and A is a reference area which, in cycling, is usually the projected frontal area. And, C_D is the drag coefficient. Since the reference area is not always well defined in the literature, it was decided to refer to the drag area $(C_D A)$ measured in m^2, when discussing results instead of using the drag coefficient. The computed drag area in the numerical and experimental simulations are provided in subsection 6.1.4 and subsection 6.2.4 respectively. An estimate of the frontal area of the cyclist model used in the experiment in this research is provided in subsection 5.2.4.

The coordinate system used throughout this thesis assumes that the drag component always follows the direction of the bike unless a crosswind result is discussed. The drag area in the direction of travel will be referred to as $C_X A$. An overview of the coordinate system is provided in Figure 2.1. A positive crosswind angle, which is the angle between the freestream and the bike's direction of travel, is oriented in a counterclockwise direction following the right-handed coordinate system shown in Figure 2.1.

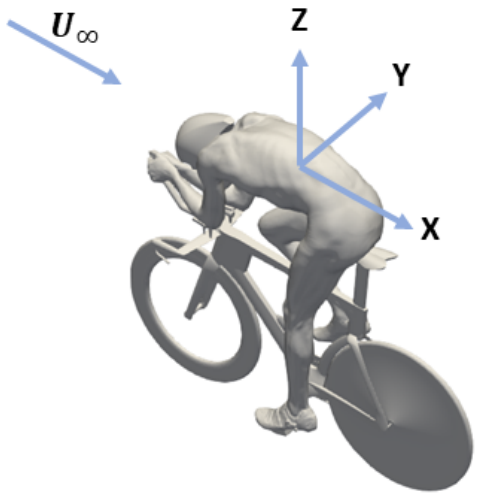

Figure 2.1: Default coordinate system fixed to the cyclist

2.1.1. Viscous and pressure drag

The drag can be further decomposed into different components. First, a boundary layer develops on all of the surfaces the flow is in contact with, resulting in shear stress acting on the cyclist. When integrated, this force contributes to the drag and is defined as *viscous drag*. Second, the variation in pressure between the front and rear sides of the cyclist will result in a force contributing to the drag. This is referred to as *pressure drag*.

A cyclist is a non-aerodynamic object (i.e. a bluff body)[1] resulting in a large pressure drag component ($\approx 90\%$ of the total drag) [2] compared to the contribution of the much smaller viscous component. Gibertini and Grassi, 2008 confirm that the majority of the drag in cycling is a result of pressure drag. Crouch et al., 2014 introduce evidence that the complex flow field in the wake of a cyclist was found to influence the local pressure distribution and therefore affect the drag. Hence, this motivates us to focus on the 3D flow topology itself when developing drag reduction methods.

2.1.2. Definitions of flow structures

To characterize the flow structures in the wake of a cyclist different variables can be used. One method to define coherent flow structures is with vorticity. This is used to define the rotation in the flow. Mathematically it is defined as the curl of the velocity field as is shown in Equation 2.2. Additionally, we can express the vorticity with scalars for the individual axis where the streamwise vorticity (ω_x) will be most important in the discussion of aerodynamic drag as it defines the rotation of the flow around the x-axis along which the drag is measured.

$$\begin{aligned} \vec{\omega} &= \nabla \times \vec{u} \\ &= \begin{bmatrix} \frac{\partial u_z}{\partial y} - \frac{\partial u_y}{\partial z} \\ \frac{\partial u_x}{\partial z} - \frac{\partial u_z}{\partial x} \\ \frac{\partial u_y}{\partial x} - \frac{\partial u_y}{\partial y} \end{bmatrix} = \begin{bmatrix} \omega_x \\ \omega_y \\ \omega_z \end{bmatrix} \end{aligned} \tag{2.2}$$

Additionally, the strength of the vortices can be evaluated with the circulation (Γ). Mathematically,

[1] Can also be described as a blunt body. In this thesis, this is referred to as an object where the majority of the drag can be attributed to the pressure drag

[2] Approximated with CFD results which will be discussed later.

circulation is defined as the line integral evaluating the velocity field around a closed surface (S) with contour (C). Using Stoke's theorem this can, however, be rewritten as a surface integral of the vorticity as is shown in Equation 2.3.

$$\Gamma = \oint_C \vec{u} \cdot d\vec{l} = \iint_S = \nabla \times \vec{u} \cdot d\vec{S} = \iint_S \omega \cdot d\vec{S} \tag{2.3}$$

More techniques exist to define coherent vortex structures, one of which is the Q-criterion. Iso-surfaces of positive values of this variable give context to the position of vortex structures and help with determining their presence. Jeong and Hussain, 1995 provide the definition of the Q-criterion, which can be found in Equation 2.4. Furthermore, Jux, 2017 uses it for the identification of flow structures in the context of cycling aerodynamics.

$$Q = \frac{1}{2}(||\mathbf{\Omega}||^2 - ||\mathbf{S}||^2) \tag{2.4}$$

Jux, 2017 mentions that the variable describes the local balance between the vorticity tensor ($\mathbf{\Omega}$) and the shear strain rate tensor (**S**). Hence, positive values of Q indicate the presence of a vortex. Often iso-surfaces of the Q-criterion are colored by vorticity helping to visualize the strength of the vortex.

Other visualization techniques (such as the λ_2-criterion and Γ_2) exist to detect flow structures. However, in the literature, the use of vorticity and the Q-criterion were found to be used frequently when discussing the flow topology in the wake of a cyclist. Hence, it was decided to focus on these variables to describe the flow field for this thesis allowing the results to be easily compared with other literature sources.

2.2. The 3D flow topology of a cyclist discussed in literature

With the definitions discussed in the previous section now, the focus shifts to the 3D flow topology of a cyclist. An overview is presented of the available literature. From these results, a discussion on the flow topology of a cyclist is provided to identify the primary structures that are found in various studies.

2.2.1. Outline on the available literature on the 3D flow topology of a cyclist

Several literature sources describe the common flow structures found in the wake of a cyclist. An overview of the most relevant in the search for drag reduction methods can be found in Table 2.1. By analyzing these results it becomes possible to identify the flow structures which appear most often using different cyclist models.

Table 2.1: Overview of the most relevant experimental and numerical investigations in the discussion on the 3D flow topology of a cyclist

Experimental studies	Measurement/ visualisation technique	Position	Crank angle	Dimension
Crouch et al., 2014	Wake rake, pressure taps, oil flow visualization	TT	Full cycle	3D
Crouch et al., 2016	Wake rake, pressure taps	TT	Full cycle	3D
Barry et al., 2016	PIV	TT	Low-drag	2D
Jux et al., 2018	Robotic volumetric PIV	TT	High-drag	3D
Terra et al., 2019	PTV measurements	TT	High-drag	2D
Spoelstra et al., 2019	Stereoscopic PIV	TT/HB	High/low-drag	2D
Terra et al., 2020	Robotic volumetric PIV	TT	High-drag	3D

Numerical studies	Numerical approach	Position	Crank angle	Dimension
Griffith et al., 2014	RANS	TT	Full cycle	3D
Griffith et al., 2019	RANS	TT	Full cycle	3D
Blocken et al., 2019	RANS	HB	Low-drag	3D
Javadi, 2022	DES	TT	High-drag	3D

Two parameters, which are expected to heavily influence the presence and position of the flow structures, are used to categorize these studies. These are the cyclist's position and the crank angle. For the cyclist's position a distinction between the handlebar (HB) position (Figure 2.2a) and time trial (TT) position (Figure 2.2b) is made. In the literature, often a clear distinction between these positions is made and both represent commonly researched positions in professional cycling. Additionally, two types of handlebar positions can be defined being the upright and dropped positions. For now, both positions will fall under the handlebar position to simplify the following discussion. However, when a variation in the flow topology and the effect on the drag between these two positions is too large this will be mentioned explicitly.

(a) Handlebar (dropped) position

(b) Time trial position

Figure 2.2: Overview of common bike positions

The other parameter, the crank position, was found to largely impact both the flow topology as well as the measured drag force (Crouch et al., 2014). This variation in the observed flow topology and measured drag force will be discussed in more detail later.

Of course, many other parameters such as geometrical features (e.g. bike specification or clothing) and Reynolds number effects will play a role in the formation and position of flow structures. However, their respective effect is considered small compared to the cyclist's position and crank angle. Nonetheless, in case another parameter is expected to influence the flow topology and this is relevant for the evaluation of the drag, this will be mentioned explicitly.

As Table 2.1 shows, most studies investigate a cyclist in TT position. It is expected that during regular stages of a cycling competition, the aerodynamic drag is minimized more effectively by drafting instead of optimizing the bike position. Spoelstra et al., 2020 found drag reductions up to 66% for the trailing cyclist in an in-line group. During individual TT stages, it is, however, not allowed for the rider to draft and therefore requires a different method to reduce the drag. Additionally, in the UCI World Tour during a TT stage, a different type of bike is allowed compared to the bike used during regular stages. The road bike and TT bike are shown in Figure 2.2a and Figure 2.2b respectively.

A TT bike allows the cyclist to be positioned in a far more aerodynamic position. Generally, this results in larger average velocities when comparing regular and TT stages assuming the TT stage has a relatively flat profile. The aerodynamic contribution to the total resistance is, therefore, greater since aerodynamic drag scales with the velocity squared as was shown in Equation 2.1 and as was explained before the individual TT stages do not allow the cyclist to draft.

The primary focus for this thesis will be on evaluating drag reduction methods in TT position given the previously discussed arguments as well as the availability of a broader range of literature allowing these results to be more accurately validated. Hence, the following discussion on the 3D flow topology will focus on the flow mechanisms found for a cyclist in TT position.

2.2.2. The 3D flow topology of a cyclist in time trial position

An outline of the general flow topology of a cyclist in TT will be provided based on the available literature. An explanation is given on the observed variation in flow topology attributed to different crank angles. In addition, similarities in the described flow topology between the different literature sources will be summarised to identify parts of the flow field that are expected to be less rider-dependent. The identification of these structures will become a basis for developing drag-reduction methods.

The variation in flow topology and drag throughout a changing crank cycle

A notable investigation on the 3D flow topology is the wind tunnel experiment by Crouch et al., 2014. Here, an extensive analysis of the flow field is provided. Flow information was captured using a wake rake, oil visualization, and surface pressure measurements. Crouch et al., 2014 define vortex structures originating from the hips and thighs as well as vortices emerging from the elbows, helmet, and calves.

Crouch et al., 2014 present a number of important conclusions. First, the authors emphasize the significance of the position of these vortices and their impact on the measured disparity in drag between what is defined as the low- and high-drag positions being the horizontal leg (Figure 2.3) and extended leg (Figure 2.4) positions respectively. Second, Crouch et al., 2014 show that this difference is linked primarily to a change in flow topology and its effect on the surface pressure distribution on the lower back. The low-drag position shows both a symmetrical development of the wake structures as well as symmetry in pressure recovery on the lower back. Progressing the crank angle to the asymmetric position, the authors discuss that the wake and pressure distribution become more asymmetrical. As a result, larger low-pressure regions on the lower back are observed. These are expected to contribute to the measured increase in drag coefficient being up to *15% larger*[3] compared to the low-drag position.

Based on this analysis it can be concluded that the presence and positioning of vortex structures largely influence the measured drag. This suggests that the manipulation of, for example, the asymmetric structures found in the high-drag position, towards a symmetric position observed in the low-drag position, could reduce the drag force assuming there is a relation between the two.

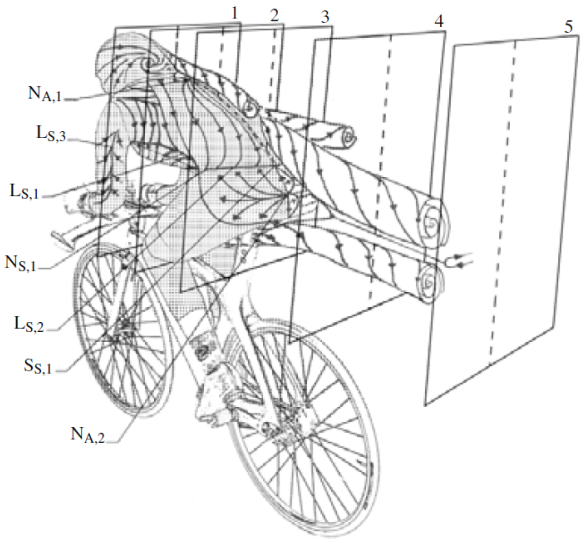

Figure 2.3: Overview of the flow structures observed in the symmetric low-drag position adapted from Crouch et al., 2014

To help structure this discussion on the flow topology, Crouch et al., 2014 define a number of flow structures for both the low and high-drag positions. First, for the low-drag position, the symmetric wake is described. Noteworthy are the vortices developing from the hips, thighs, and upper arms. Particularly

[3]The authors emphasize that the variation in the frontal area is less than 2%. Moreover, in the computation of the drag coefficient, this small difference in projected frontal area has been included.

the structures originating from the upper arm and hips are thought to be manipulable without obstructing the cyclist in its ability to output the required power while pedaling. An overview of these structures can be found in Figure 2.3.

For the high-drag position the asymmetry in the flow topology is clearly visible as is shown in Figure 2.4. Similar structures, positioned at the hips, thighs, and upper arms, are observed but positioned asymmetrically along the vertical axis. In this position, a counter-rotating vortex pair originating at the elbows is described. All these structures are thought to be manipulable without obstructing the cyclist, except the thigh structures as they are related to the movement of the legs. Manipulating these vortices through a geometrical change close to the legs could result in a reduced pedaling efficiency and is therefore not considered in the development of drag-reduction methods.

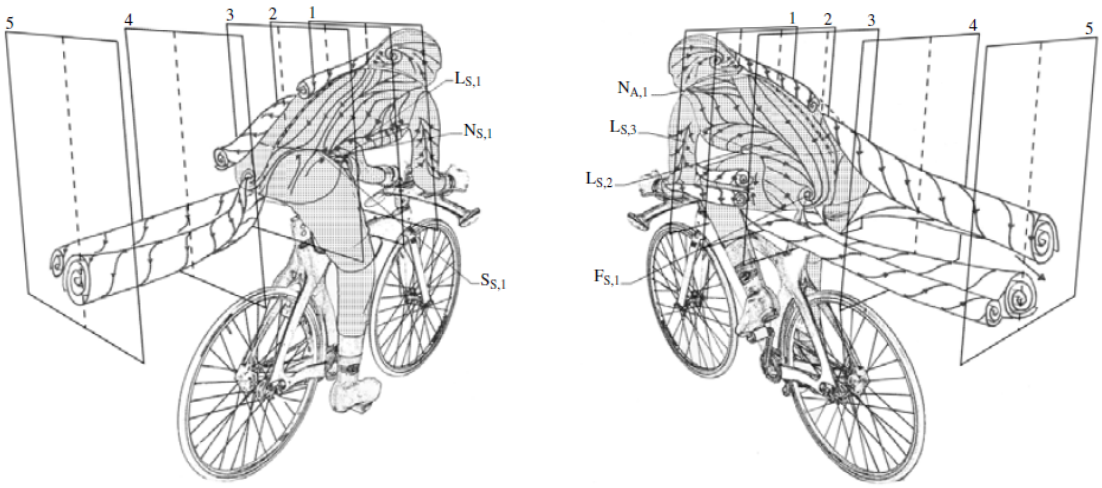

(a) RHS view **(b)** LHS view

Figure 2.4: Overview of the flow structures observed in the asymmetric high-drag position adapted from Crouch et al., 2014

From this analysis, it becomes clear that a few prominent vortex structures appear both between the high- and low-drag positions. These structures are the vortices originating from the hips, elbows, and helmet. The latter is, however, challenging to manipulate as it may be related to the helmet's geometry. Hence, this structure will not be tested in the development of the drag reduction methods. Instead, the focus lies on the manipulation of the elbow and hip vortex structures. However, before these structures are investigated in more detail, first a comparison between the different literature sources will be made to inspect and validate the presence of these structures.

Flow similarities between the different literature sources

Other sources that describe a similar flow topology are Griffith et al., 2014, Jux et al., 2018, and Spoelstra et al., 2019 amongst others. Griffith et al., 2014 discuss the results of a numerical study based on the model used by Crouch et al., 2014. The authors conclude that the wake topology of the numerical results agrees with the experimental measurements. Jux et al., 2018 discuss the results of a full-scale model of Tom Dumoulin[4] where the flow topology was measured using 3D Lagrangian particle tracking (3D LPT). The authors mention that the flow structures and their position are in agreement with the observations of Crouch et al., 2014 and other sources. Finally, Spoelstra et al., 2019 discuss that the results from an on-site PIV measurement also compare well with the results of Crouch et al., 2014.

The topological similarities observed between these different studies consolidate the opportunity to try to manipulate the upper arm and hip structures without limiting ourselves to a single athlete. However, it can be expected that the effectiveness or potential in drag reduction may vary between athletes.

[4]Tom Dumoulin is a former professional cyclist who has won the 2017 Giro d'Italia, two silver Olympic medals, and many other events. He is also well known for his successes in time trial events.

Nonetheless, the hypothesis and aerodynamic workings of a drag reduction method should show similarities irrelevant of the athlete.

To further strengthen the claims made on the presence of such structures independent of the athlete, use will be made of a Generic Cyclist Model in the development of the drag reduction methods. More details on this model will be discussed in section 2.5.

Effects of the dynamic leg motion on the 3D flow topology

Before continuing with a detailed discussion on the elbow and hip structures, first, the dependency of the motion of the legs on the general flow topology compared to a quasi-static position of the legs is discussed. So far, only the dependence of these structures based on the quasi-static position of the crank has been discussed. It was concluded that even the position of structures found close to the lower back is highly dependent on the crank angle.

Crouch et al., 2016 and Griffith et al., 2019 have both investigated the effect of the pedaling motion on the flow topology with experimental and numerical simulations respectively. Crouch et al., 2016 mention that the flow fields between both the static and dynamic experiments compare well and only small discrepancies are reported. Hence, the difference in the solution of the wake topology of a pedaling cyclist compared to the static crank position is found to be small.

Griffith et al., 2019 describe a similar result where the wake topology compares well between the static and dynamic simulations in a numerical study. Therefore, both of these results suggest that the effectiveness of drag reduction methods on a static level should translate to a pedaling cyclist. This allows a numerical and experimental study to be simplified while still being able to accurately capture the working mechanisms of the drag reduction methods.

2.2.3. Hip vortex structures

The first flow mechanism which is further investigated is the mechanism of the hip vortices. Descriptions from different sources will be used to sketch a brief outline of the position and strength of these vortices. Crouch et al., 2014 describe the hip vortices being a primary feature of the wake present for the majority of the leg positions. Crouch et al., 2014 make an analogy of the cyclist's torso with low-aspect-ratio wings comparing the development of streamwise vortices over wings with the hip vortices. The pressure difference between the lower side of the torso and the suction on the back is expected to generate a flow up and around from both sides of the torso towards the lower back of the cyclist resulting in the hip vortices.

The results of Crouch et al., 2014 show that the position of the hip vortices changes between the high- and the low-drag positions. In the high-drag position, it was found that the vortices are not symmetric anymore along the xz plane. These differences in the position of the flow structures for the high- and low-drag positions are shown in plane 4 in Figure 2.5. The numbered planes correspond to the plane positions shown in Figure 2.3 and Figure 2.4.

The presence of these hip vortices is also mentioned by Terra et al., 2019,Spoelstra et al., 2019, and Terra et al., 2020. The formation of the hip vortices starts on the side of the lower torso making its way toward the center line and the lower back. Because the hip vortex pair is counter-rotating a downwash component on the slanted back is created. As a result, separation of the flow on the lower back is delayed and the topology of the wake structures is influenced. An example of these structures can be found in Figure 2.6.

The presence of the hip vortices is widely discussed in the literature for both the high- and low-drag positions. This makes it a compelling case to investigate the possibility of manipulating these structures to find drag reductions. Furthermore, Crouch et al., 2014 provide an important conclusion, mentioning that over 75% of the variation in the back suction drag between the high- and low-drag positions, is a result of the surface pressures acting on the lower back. Additionally, these surface pressures are

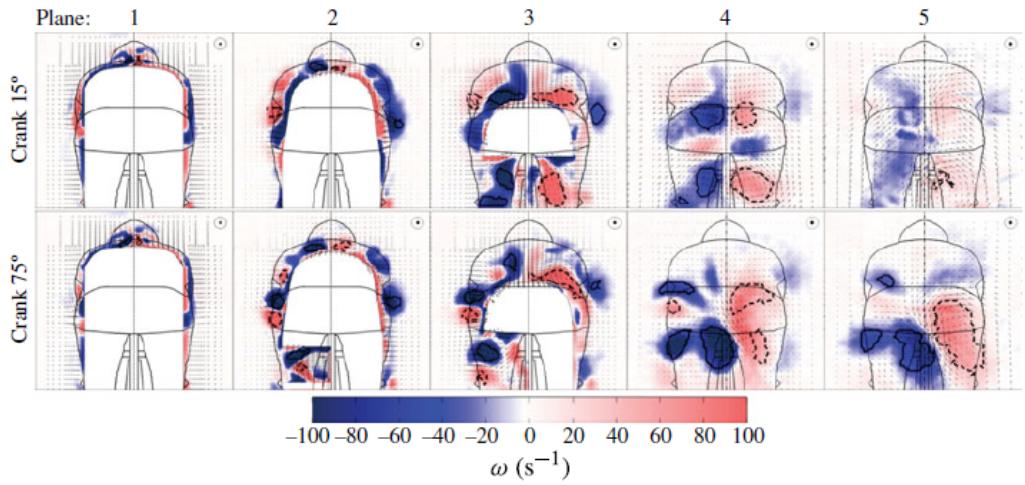

Figure 2.5: Development of vortex structures for both the low-drag (top) and high-drag (bottom) positions. Adapted from Crouch et al., 2014

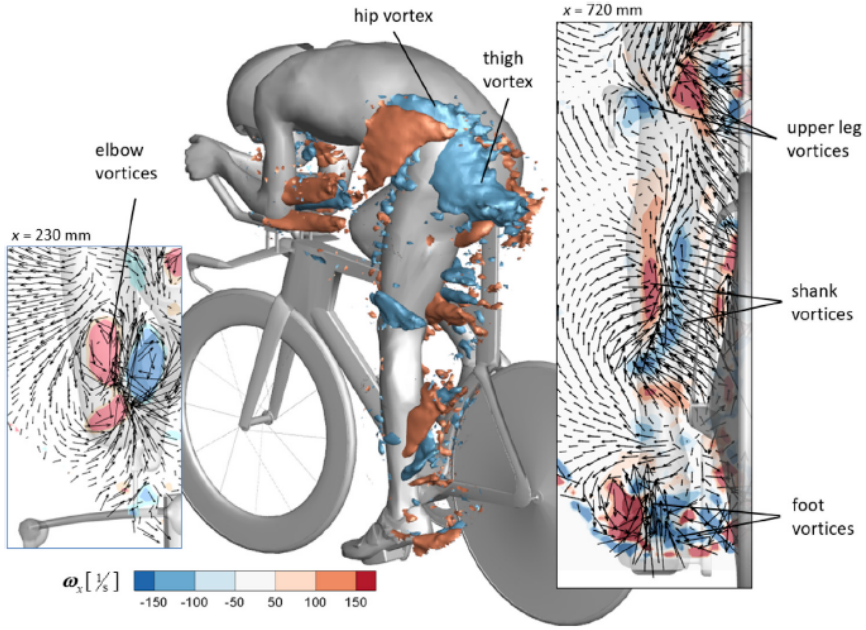

Figure 2.6: Overview of the time-average flow structures measured with 3D PTV shown with iso-surfaces of vorticity at -120 and 120 rad/s. Adapted from Terra et al., 2020

found to be dependent on the position and strength of the local flow structures. This suggests that the manipulation of these structures could result in measurable drag reductions and therefore consolidate the investigation of the hip vortices.

2.2.4. Elbow vortex structures

Another prominent pair of vortex structures described by Crouch et al., 2014 are the elbow vortices. Since a wake rake was employed to measure the pressure around the cyclist, limited information on these smaller and difficult-to-reach flow structures is available. Nonetheless, Crouch et al., 2014 do describe the presence of this vortex pair and how it contributes to an outwash around the side of the torso. Based on this it is assumed that this elbow vortex pair affects the local pressure distribution for multiple regions such as the upper arms, stomach, and sides of the torso.

Terra et al., 2020 also provide a visualization with iso-surfaces of vorticity of this vortex pair as can be seen in Figure 2.6. This pair originates just above the elbow on the upper arm. Furthermore, the vortex pair is counter-rotating, similar to the hip vortices, as can be seen from the figure.

2.3. Effect of vorticity on the local surface pressure distribution

As discussed briefly, the presence of vortex systems influences the local pressure distribution. The effect on the pressure distribution of the difference in the position of the hip vortices between the high- and low-drag positions has been measured using pressure taps on the lower back of a cyclist by Crouch et al., 2014. This is an important analysis and helps to explain why flow manipulation of these structures may result in drag reductions in cycling.

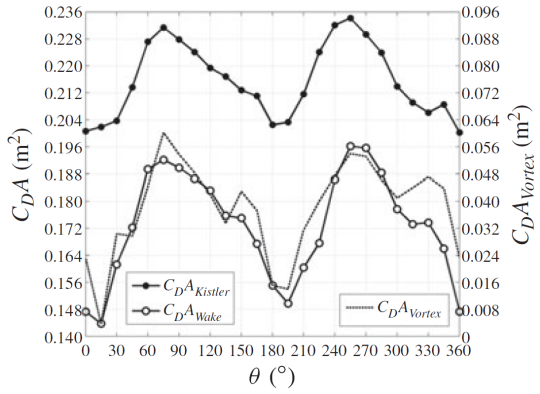

(a) Overview of the integrated wake and vortex drag approximations compared against the balance drag area measurements. Both axes have the same scale

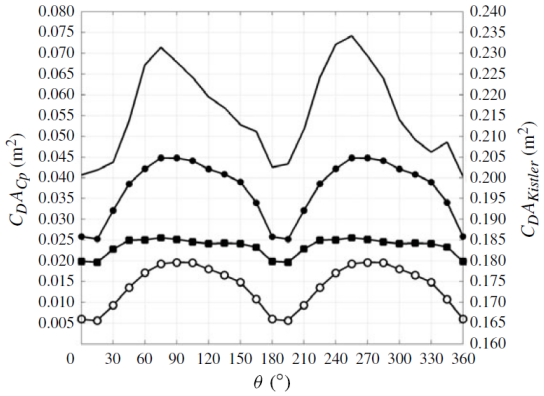

(b) Left-hand axis: suction drag area as a function of crank angle from back total $(- \cdot -)$, upper back $(-\blacksquare-)$, and lower back $(- \circ -)$. Right-hand axis: drag area $(-)$

Figure 2.7: Overview of the drag area measurements for a changing crank angle adapted from Crouch et al., 2014

The variation in drag area throughout a changing crank angle is highlighted in Figure 2.7a. Here, a comparison between the total drag area measured with a balance (C_DA_{Kistler}) for a changing crank angle is compared to the drag area resulting from a wake integral analysis (C_DA_{Wake}). This takes into account the wake's deficit in stagnation pressure, streamwise velocity, and the contribution of the in-plane velocity component to the drag (Hucho and Sovran, 1993). The wake integral analysis provided a drag area approximately 25% lower as a result of only taking into consideration part of the wake (Crouch et al., 2014).

The relation used to compute the drag area from the wake integral analysis can be found in Equation 2.5. Here, p_∞ and p_t are the freestream static pressure and total pressure respectively.

$$C_DA = \iint_A \frac{p_\infty - p_t}{\frac{1}{2}\rho U_\infty^2} \mathrm{d}a + \iint_A 1 - \left(\frac{u}{U_\infty}\right)^2 \mathrm{d}a + \iint_A \left(\frac{v}{U_\infty}\right)^2 + \left(\frac{w}{U_\infty}\right)^2 \mathrm{d}a \tag{2.5}$$

C_DA_{Vortex} was computed using a similar wake integral analysis, only taking into account the primary vortices identified using a swirling strength criterion. Crouch et al., 2014 conclude that C_DA_{Vortex} accounts for almost all of the variation in drag area between the high- and low-drag positions. This is highlighted in Figure 2.7a. These results provide strong evidence that the presence of vortex structures can indeed largely impact the drag area of a cyclist.

Figure 2.7b indicates that between the high- and low-drag positions a large variation in the surface pressure on the lower back of the cyclist is observed. This indicates the effect of a changing flow topology on the surface pressure distribution on the back of the cyclist.

Crouch et al., 2014 attribute the observed low-pressure regions to the primary vortex pair found in

the high-drag position. Compared to the low-drag position, an easily observable difference in surface pressure is found. This difference in surface pressure is shown in Figure 2.8.

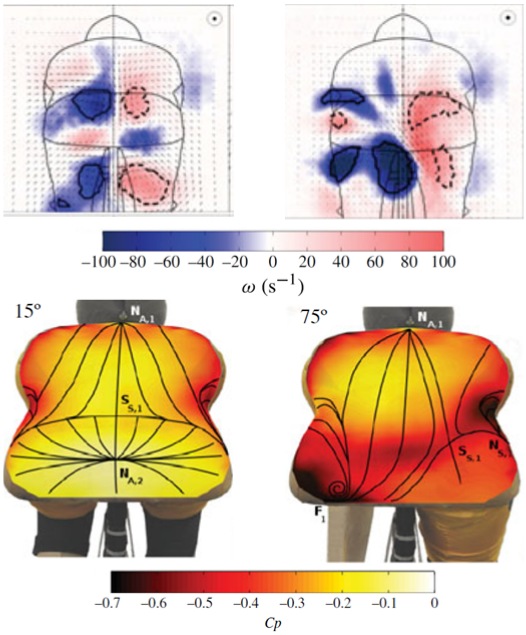

Figure 2.8: Streamwise vorticity (top) and pressure coefficient (bottom) for the low-drag (left) and high-drag (right) positions. Adapted from Crouch et al., 2014

Figure 2.8 shows that the vorticity in the wake of the asymmetric position has increased, especially for the left-hand side (LHS) thigh vortex. A significant reduction in pressure on the lower back of the cyclist is observed. Since the contribution to the drag force is driven by the force component in the direction of travel, the more the normal component on the surface of the cyclist is pointing along this axis the larger its contribution to the drag. Hence, it is especially the lower back which will largely affect the drag force. Therefore, the reduction in surface pressure on the lower back should be minimized to reduce the drag.

The difference in surface pressure can not only be attributed to the difference in vortex position. Other parameters such as flow separation also affect the surface pressure distribution. However, the conclusions by Crouch et al., 2014 highlight an interesting connection between vortex strength and position and its effect on the surface pressure distribution and therefore pressure drag. Although this relation has not been studied in cycling aerodynamics it was found that on other bluff bodies, this has been studied which will be explained in the next section.

2.4. Analogy with drag reduction methods on bluff bodies

Before further diving into drag reduction methods in cycling it is useful to evaluate proven concepts in other research fields. This could provide a helpful design direction and keep us from reinventing the wheel. A great example is the research done on an Ahmed body. The literature discusses the general flow topology (Vino et al., 2005) and the effect of cross-wind on the flow structures (Sciacchitano and Giaquinta, 2019). Additionally, Szodrai, 2020 discusses in a quantitative analysis the results of different literature sources focusing on drag reduction methods for blunt-shaped automobiles.

The analysis of bluff-shaped bodies like an Ahmed body is relevant in the discussion of cycling aerodynamics because similarities in the flow topology can be highlighted. An overview of the wake topology found in the wake of an Ahmed body can be found in Figure 2.9. Here it can be seen that the vortex structure forming on the slanted back - often referred to as c-pillar vortices - shows similarities with the hip vortices on a cyclist, previously discussed in subsection 2.2.3.

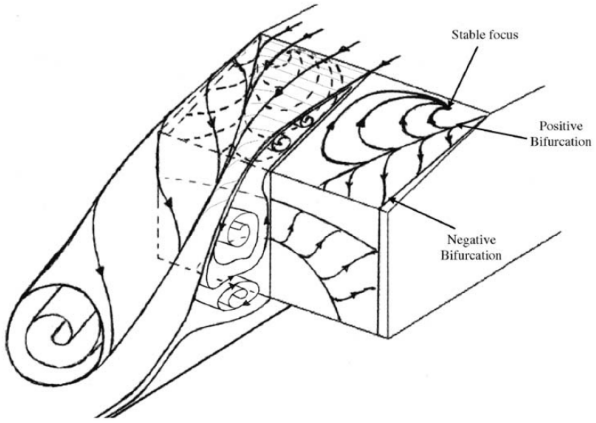

Figure 2.9: The flow topology in the wake of an Ahmed body. Adapted from Vino et al., 2005

Szodrai, 2020 suggests three types of drag reduction categories applicable to bluff bodies. These are active systems, shape modifications, and topological modifications. A distinction is made between modifying the object itself, referred to as a shape modification, and adding a winglet-type modification which falls under a topological modification. Since this thesis focuses on the manipulation of the near wake topology, all active systems are disregarded because the aim of this thesis is not to add a complex active aerodynamic system in requirement of an additional energy source. Instead, the focus is on adding devices to the system or changing for example the suit design to manipulate the flow topology in a passive manner. Based on the following analysis of drag reduction methods on bluff bodies a number of geometrical concepts for cycling will be proposed in chapter 3.

2.4.1. Passive drag reduction methods through topological modifications

The aerodynamic evaluation of winglets on an Ahmed body was investigated by Beaudoin and Aider, 2008 where they discuss that some configurations led to a drag reduction of 25%. Besides this impressive drag saving, their discussion on the aerodynamic mechanism behind this is very interesting and perhaps counterintuitive at first.

They discuss that for the baseline configuration, the presence of the c-pillar vortices contributes to a delay in separation on the slanted back. This is argued to be a result of a downwash component induced by these vortices. As was discussed previously, a similar effect is observed on the lower back of a cyclist in TT position as a result of the hip vortices. It is instrumental to compare the vortex strength between the Ahmed body and that of the cyclist so that we can better understand the possible drag reduction when targeting the latter case.

One may expect this to be a desired effect as the wake itself is reduced. However, after adding the winglets on the slanted back of the Ahmed body the vortices reduced in strength and size, separation happened further upstream and the wake increased in size. A comparison between the wake topology in the wake of the Ahmed body of the baseline and winglet configuration can be found in Figure 2.10.

The expansion of the wake is clearly captured in these results. However, Beaudoin and Aider, 2008 also measured a reduction in drag. It was found that even though the size of the wake had increased, the increase in back pressure because of the absence of the c-pillar vortices resulted in a net reduction of the drag.

Similar results were obtained by Aider et al., 2010 by applying vortex generators on a modified Ahmed body with a curved back. The authors suggest that the vortex generators in this case promote separation as they expect these to increase the boundary layer outflow compared to the inflow and hence, promote separation. Furthermore, a drag reduction of 12% was measured and it was observed that the wake had increased in size with a measurable reduction in longitudinal vortices. A comparison

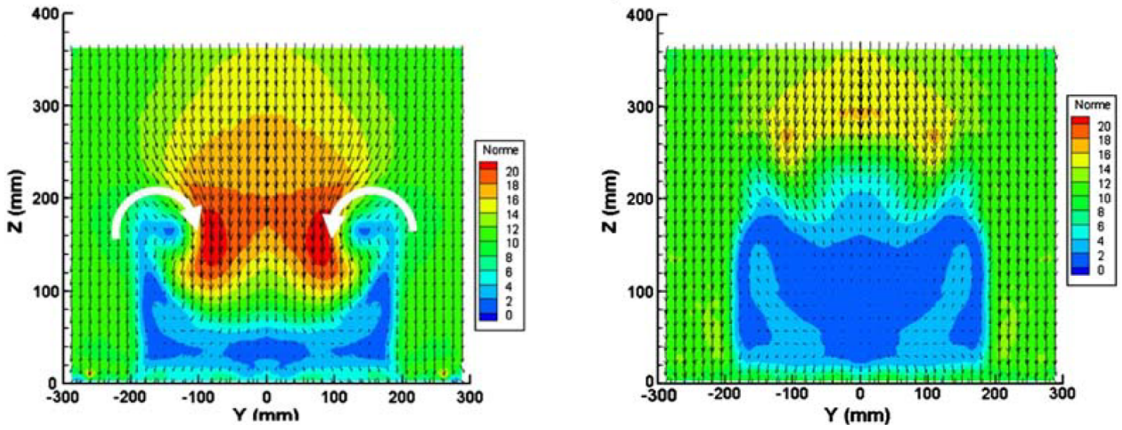

(a) Baseline configuration

(b) Added winglets resulting in larger wake with reduced vorticity

Figure 2.10: PIV measurements were taken at a plane 129 mm downstream of the model showing transversal velocity field. Comparison of the wake structures between the baseline and configuration with angled flaps installed on the slanted back in the longitudinal direction measured at $u_\infty = 20$ m/s. Adapted from Beaudoin and Aider, 2008

between the baseline and the configuration with the vortex generators can be found in Figure 2.11.

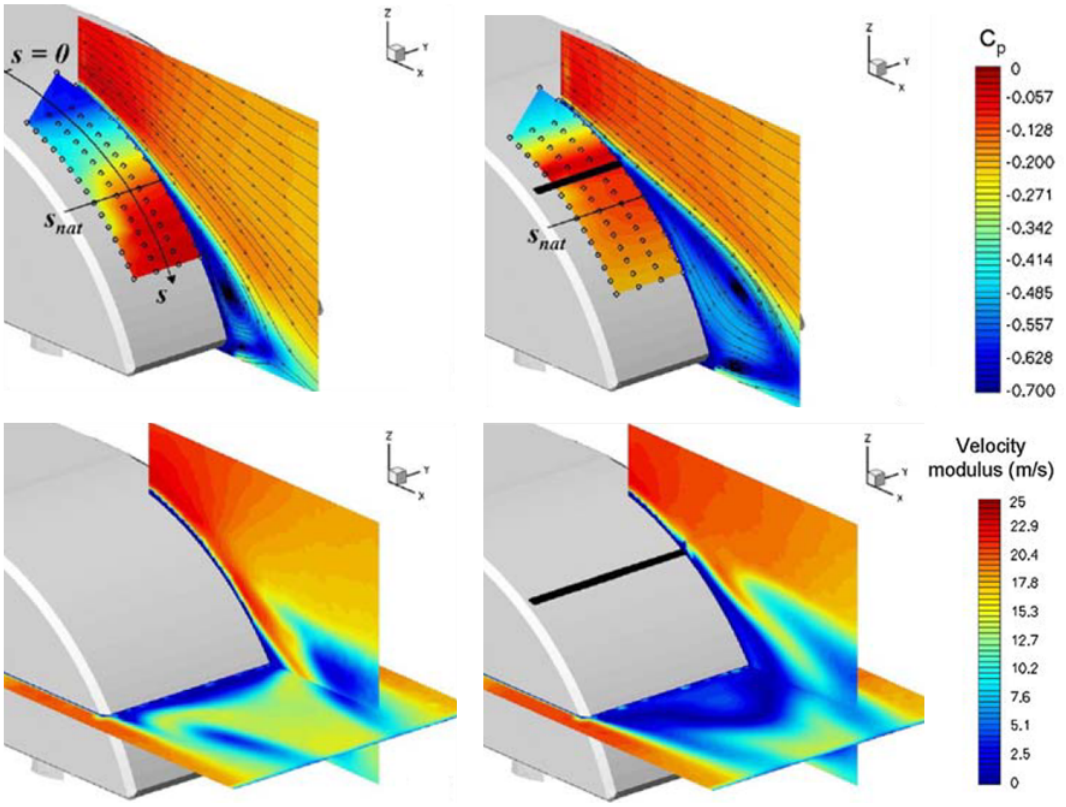

Figure 2.11: Baseline configuration (left) and added vortex generators (right) showing surface pressure and velocity (top). Velocity in other wake planes is shown in the bottom row. Adapted from Aider et al., 2010

The results show that the separation location has moved further upstream on the curved back and as a result, the size of the wake has increased. Furthermore, the pressure coefficient is plotted on the curved back which shows the increase in surface pressure contributing to the reduction in drag. Aider et al., 2010 highlight the connection between the weakening of the trailing vortices with the early separation and its effect on the drag reduction.

Aider et al., 2010 continue by mentioning that the total drag experienced by a bluff body includes contributions of a momentum and pressure deficit. A relation between the drag area and the momentum and pressure deficit for 3D bluff bodies was provided in Equation 2.5. Part of the momentum deficit is attributed to what is defined as the vortex drag (this is the final term in Equation 2.5) which is the contribution of the streamwise vortices to the total drag. However, Aider et al., 2010 adds to this that the counter-rotating vortex pairs generate a downwash and thus a low-pressure region. Hence, the streamwise vortices are also contributing to the pressure deficit. Moreover, it is concluded that a reduction in drag for a bluff body should be achieved by delaying separation and reducing the strength of the trailing vortices to minimize the momentum and pressure deficit. This is an important conclusion in the development of cyclist drag reduction methods.

Aider et al., 2010 end with a few important conclusions on the working mechanism of the experimental results. It is mentioned that the reduction in drag is related to the weakening of the longitudinal vortices. These, when integrated in a plane in the wake, show a reduction in the circulation compared to the baseline configuration strengthening the relation between the reduction in vorticity and the reduction in drag. Furthermore, it is argued that the drag reduction observed as a result of this reduction in longitudinal vorticity is larger compared to the drag increase created by the larger recirculation or wake.

2.4.2. Passive drag reduction methods through shape optimization

The research of Hwang et al., 2016 discuss the effect of side skirts on heavy vehicles resulting in a drag reduction of approximately 5%. Part of the drag reduction, based on LES results, is attributed to the absence of vortex structures when the side skirts have been applied. These results are in line with the previously discussed conclusions of Aider et al., 2010.

This analysis provides an opportunity to try to replicate this effect at the elbows and upper arms of a cyclist. As was discussed in subsection 2.2.2, counter-rotating vortex pairs originate from both elbows. It can be expected, considering the previous discussion, that these structures are largely responsible for the local pressure distribution and therefore the pressure drag on the upper arms and torso as well. Hence, this is the second area of interest in trying to manipulate flow structures to find drag reductions.

2.5. Generic Cyclist Model (GCM)

As was briefly mentioned before, the objective is to find drag-reduction methods that are translatable to other cyclists. This means that the underlying mechanisms can not be rider-specific but should only be related to the relative position of the rider instead. The first method that was proposed to increase the likelihood of finding a rider translatable drag reduction method, was the evaluation of flow structures found in multiple literature sources which use different cyclist models.

A second method is the introduction of a generic cyclist model (GCM). Using the scans of multiple professional riders in TT position, an average was taken resulting in a generic cyclist model. The flow structures in the wake of the generic cyclist model are therefore expected to be a more general representation of the flow field. The combination of both methods is likely to contribute to more robust drag reduction methods instead of finding a rider-specific result. As will be explained later, first a numerical investigation will be used to investigate the workings of different drag reduction methods. This is performed with a different model than the model used in the wind tunnel experiment. In case the measured difference in drag translates well between the numerical results and the wind tunnel results this will help with the argumentation that the drag reduction methods are mainly bike position-dependent instead of rider-dependent. The GCM in TT position can be found in Figure 2.12. A more detailed explanation of the development of the GCM is provided by Vloemans, 2022.

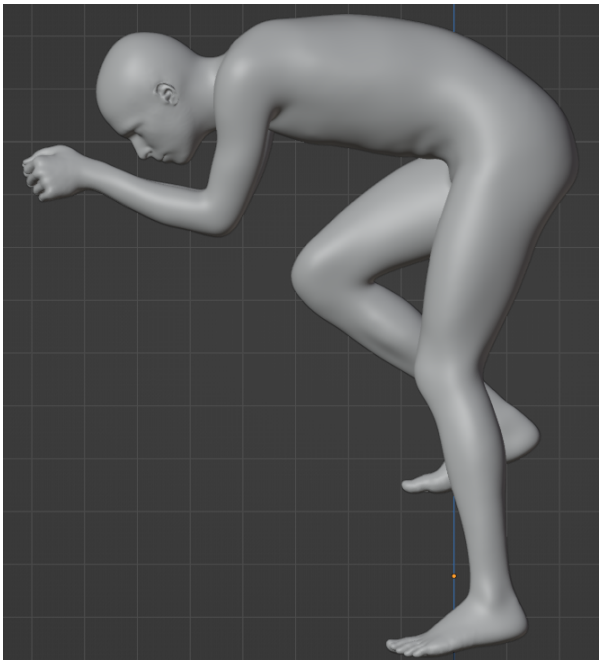

Figure 2.12: Digital model of the GCM in the high-drag time trial position

2.6. Research questions

From the discussion on the 3D flow topology, a series of research questions have emerged. The first question focuses on the possibility of finding a drag reduction through the manipulation of the flow topology.

Is it possible to achieve drag reductions for a cyclist in time trial position by manipulating the hip and upper arm vortices?

The next question focuses on the relation between the variation in vorticity and the measured drag area. As was discussed in section 2.3 the variation in drag area between the high- and low-drag positions can be attributed primarily to a variation in wake topology and a change in measured vortex drag. However, when flow structures are manipulated through geometrical modifications it should also be investigated whether a difference in drag can still be attributed to a change in vortex strength.

To what extent does a reduction in vortex strength contribute to a change in drag?

Finally, for the development of the drag reduction methods, a combination of both numerical and experimental simulations was used. For bluff body aerodynamics, however, a correct mapping of the physical representation of the wake topology is considered challenging. Furthermore, depending on numerical simulations only could result in a large uncertainty on the physicality of the solution. However, the numerical simulations can help with the early development of drag reduction methods. Then, the most promising designs can be tested in a wind tunnel experiment to help verify their effectiveness and underlying working mechanisms using balance measurements and flow visualization techniques. This sequential aerodynamic development process poses an interesting opportunity to evaluate the added benefits of exploring both types of methodologies in the development of drag reduction methods. This leads to the final research question.

To what extent can the combination of using numerical simulations with balance measurements and 3D-PTV complement each other in aerodynamic development?

3

Methodology

Through the evaluation of the previously discussed drag reduction methods from other research areas, different methods are proposed to achieve a reduction in drag for a cyclist in TT position. A description of the expected workings is provided. To start developing these drag reduction methods it is required to choose a measurement technique to evaluate both the observed drag force as well as the flow field to help decide what design direction to pursue. For this, a variety of options are available. Terra et al., 2016b for example, mention that cycling aerodynamics has been researched with wind tunnel measurements, field tests, and numerical simulations (e.g. CFD).

Each of these methods has advantages over the other and could all contribute to finding a broader understanding of the aerodynamics and complex flow field found in the wake of a cyclist. The following sections provide an evaluation of the most promising methods. First, the methodology behind the proposed cyclist drag reduction methods is discussed. Then, an explanation of a numerical campaign is given. These simulations are used to investigate the proposed drag reduction methods before testing these in the wind tunnel. Lastly, the methodology behind the measurement techniques used in the wind tunnel is discussed. The experimental simulations are used to obtain a deeper understanding of the flow mechanics of the most promising drag reduction methods found with the numerical simulations and to verify their working mechanisms.

3.1. Drag reduction methods through flow manipulation in cycling

A variety of drag reduction methods were engineered to manipulate the near-body flow structures of a cyclist in TT position. The following section discusses the design requirements for these methods. Furthermore, an explanation of the methodology behind each drag reduction mechanism is provided.

3.1.1. Design requirements

For each of the designs, several requirements were taken into consideration which are briefly discussed. Each method is developed to be compatible with modern cycling equipment. This means that a drag reduction method is designed to work with a cyclist in TT position on a modern TT bike. An example of such a configuration was shown previously in Figure 2.2b.

The next requirement is to keep each design symmetrical across the xz-plane (following the coordinate system introduced in Figure 2.1) to make it compatible with the full range of crank positions. The aim is to develop drag-reduction methods that provide a net gain for all crank positions instead of finding a local minimum enabled with an asymmetric design.

Finally, additional care on the position and size of the designs is given to minimize any losses of the power output of the cyclist. Manipulation of the flow structures close to the legs could result in an obstruction of the pedaling motion and result in a less efficient power transfer. Hence, the development of drag reduction methods is focused on parts of the body that remain relatively static during a pedaling motion. Following these design requirements, the focus now shifts towards the first drag reduction method.

3.1.2. Hip Vortex Control (HVC)

The first drag reduction method is based on the reduction of the hip vortices by promoting separation on the lower back of the cyclist. Based on the discussion in subsection 2.4.1 it was found that by promoting separation on the slanted back of an Ahmed body it is possible to reduce the c-pillar vortices in strength. As a result, an increase in surface pressure was measured resulting in a reduced drag force.

As was discussed in section 2.3, Crouch et al., 2014 provide insight into the relationship between the hip vortex position, leg position, and lower back pressure distribution. As the hip vortices show similarities in the local flow topology between the Ahmed body and a cyclist in TT position, it is expected that a reduction of the hip vortices could increase the local pressure distribution on the back of the cyclist leading to a reduction in drag.

Preferably, the vortex pair originating from the thighs would be reduced in addition to the hip vortices, to investigate if the drag reduction can be made more effective. However, since this system originates from the legs it makes it very difficult to manipulate the flow without affecting the pedaling efficiency of the rider. Hence, this is not considered for this thesis and the focus lies on the manipulation of the hip vortices alone.

To promote separation on the lower back of a cyclist, a device named the hip vortex control (HVC) is introduced. The geometry is kept relatively simple as it exists of three flat surfaces. One horizontal surface is positioned in the middle and two angled surfaces are positioned at the sides, all integrated on the lower back of the cyclist. The horizontal surface could be seen as a spoiler-like geometry. An impression of the HVC on the back of the GCM can be found in Figure 3.1.

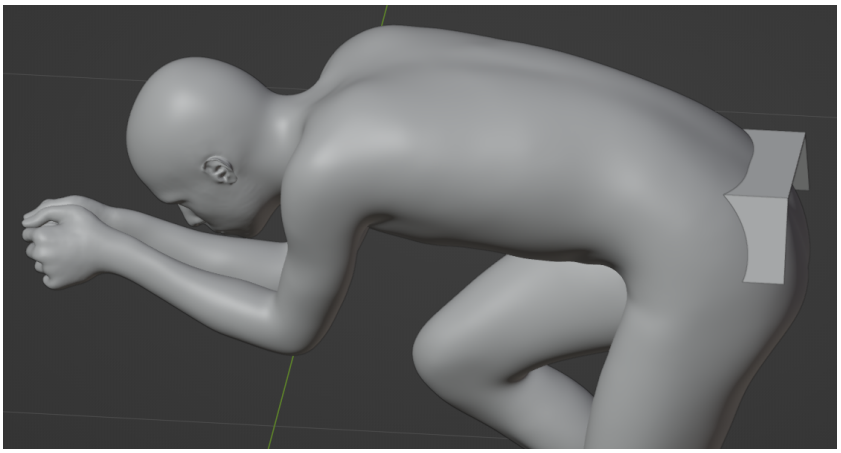

Figure 3.1: Example of the hip vortex control drag reduction method integrated on the lower back of the GCM

The aerodynamic mechanism to promote separation using this method is explained by the stagnation of the flow on the horizontal component resulting in a local pressure increase. Hence, it is expected that the larger adverse pressure gradient will contribute to the flow separating earlier on the back of the cyclist. Furthermore, since the hip vortices were found to continue across the sides of the upper legs, as was shown in Figure 2.6, the angled side plates have been added to control and reduce their formation. This mechanism is expected to decrease vortex strength close to the lower back of the cyclist and therefore increase the local pressure distribution and reduce the drag.

3.1.3. The Wingsuit

The next drag reduction method is focused on minimizing the elbow vortices and increasing the pressure distribution on the upper arms of the cyclist. Although the local flow field is exceedingly complex and has fewer similarities with the previously discussed drag reduction methods for bluff bodies, the principles are thought to be comparable to the methodology of the HVC.

To reduce the vorticity originating at the elbows a triangular-shaped geometry is introduced positioned between the upper arm and upper torso which is named the wingsuit. The design of the wingsuit drag reduction method integrated with the GCM can be found in Figure 3.2.

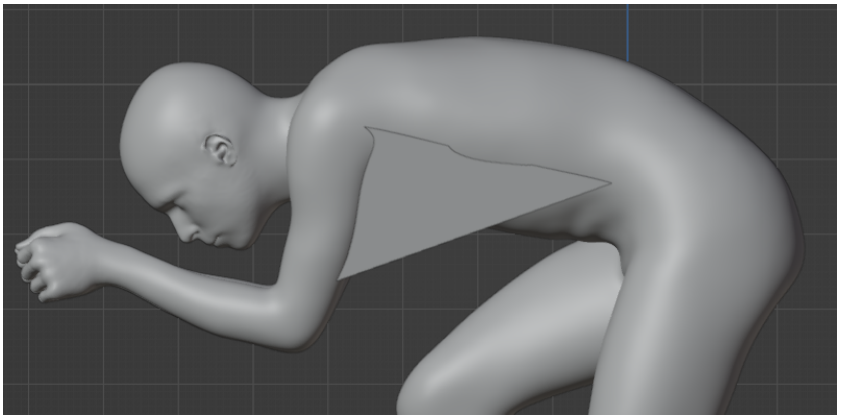

Figure 3.2: Example of the wingsuit drag reduction method on the GCM

By keeping the flow from moving laterally along the trailing edge of the upper arm, the wingsuit is meant to limit the formation of elbow vortices, shown in Figure 2.6. Furthermore, the wingsuit can help reduce the adverse pressure gradient on the outboard upper arm and therefore reduce separation on the outboard portion of the arm. The positioning of the wingsuit on the upper body and arms is expected to allow the cyclist to deliver the same amount of power as the wingsuit is only connected to static parts of the body when the cyclist is in a pedaling motion.

3.2. Aerodynamic development process

To structure the aerodynamic development of the discussed drag reduction methods a design process based on numerical and experimental simulations is presented. A flowchart of the proposed design process can be found in Figure 3.3.

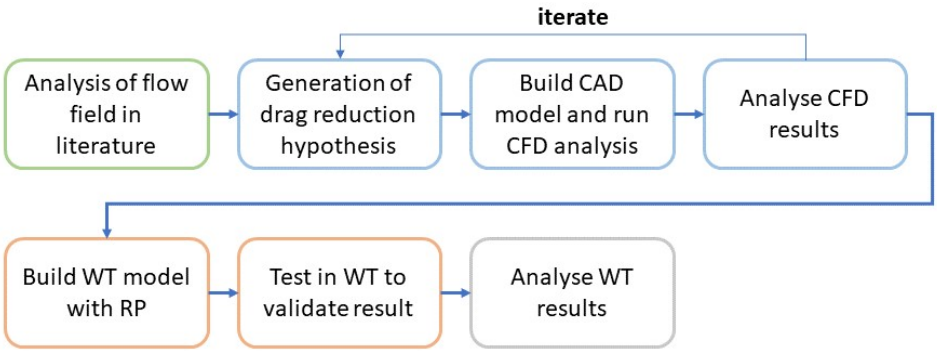

Figure 3.3: Flow chart of the proposed design process

Instead of depending on wind tunnel measurements exclusively, which can be very expensive, the early development of the designs is done numerically instead. Major benefits of the numerical evaluation of

the drag reduction methods are the fast iteration time and the possibility to immediately evaluate the results with the inclusion of detailed information on the flow field. These noticeable advantages will help in generating a broad understanding of the effectiveness of the proposed drag reduction methods and indicate clear design directions.

Besides increasing the development efficiency of the drag reduction methods, this investigation will also be a demonstration of how both numerical and experimental simulations can complement each other in aerodynamic development. Next, the details of the numerical and experimental methodology are discussed.

3.3. Numerical methodology

Although numerical simulations can be challenging in the context of unsteady flows, it does provide an extensive framework for aerodynamic development. For example, flow information in the full computational domain is captured. Additionally, numerical simulations can be run at a relatively low cost and are a time-efficient method to examine complex flow fields given that the results can be validated.

For this investigation, the use of open-source software was maximized, making it easier to replicate these processes. Besides the main objective of this numerical investigation, this could be considered as a demonstration of the capability of these openly available software packages to illustrate their strengths in the early stages of aerodynamic development.

3.3.1. Computer-aided Design (CAD) and cyclist model

For the development of the CAD models of the discussed drag reduction methods, it was decided to use *Blender*. This is an open-source software package, that allows the user to access a large online community with great support channels making it easier to solve problems quickly. Additionally, the manipulation of a previously developed or finished CAD model is relatively intuitive with Blender. Other CAD programs sometimes struggle with this and require the full build history to allow for a qualitative adaptation of the geometry. Finally, as it is an open-source program it permits anyone to replicate this design process in the future, without having the requirement of buying a software license.

The cyclist model used in this numerical experiment should preferably have volumetric validation material available. Because this investigation focuses on the manipulation of 3D flow structures it is important that their position and strength in the numerical solution is representable of what is expected to be measured in the wind tunnel. Hence, the validation data is preferably in the form of a wind tunnel experiment with sufficient data on the 3D flow topology.

It is because of this reason, that a digital model of Tom Dumoulin was used of which the 3D flow topology has been investigated by Jux et al., 2018 in a full-scale wind tunnel experiment using 3D Particle Tracking Velocimetry (PTV). The results provide an extensive solution set to compare against the results of the numerical simulations. An example of the quality of the captured flow structures in the experiment of Jux et al., 2018 can be found in Figure 3.4. To improve the correlation of the flow topology with the wind tunnel results of Jux et al., 2018, mesh settings and boundary conditions can be modified as will be discussed in chapter 4.

The numerical model of Tom Dumoulin is positioned in the high-drag position. This is similar to the position of the GCM which will be used in the experimental simulations as was discussed in section 2.5. This will limit the information on the effectiveness of the drag-reduction methods to the high-drag position. As Crouch et al., 2014 have shown, the position of flow structures changes throughout a full rotation of the crank. However, the presence of the upper arm and hip vortices remains independent of the crank angle, and the drag reduction methods are therefore expected to remain effective for the low-drag position. The development of the drag reduction methods for the high-drag position is thought to be more interesting because of the asymmetric position of the hip vortices. It is expected that the asymmetric position of the vortices is more challenging to manipulate with, as previously discussed, a

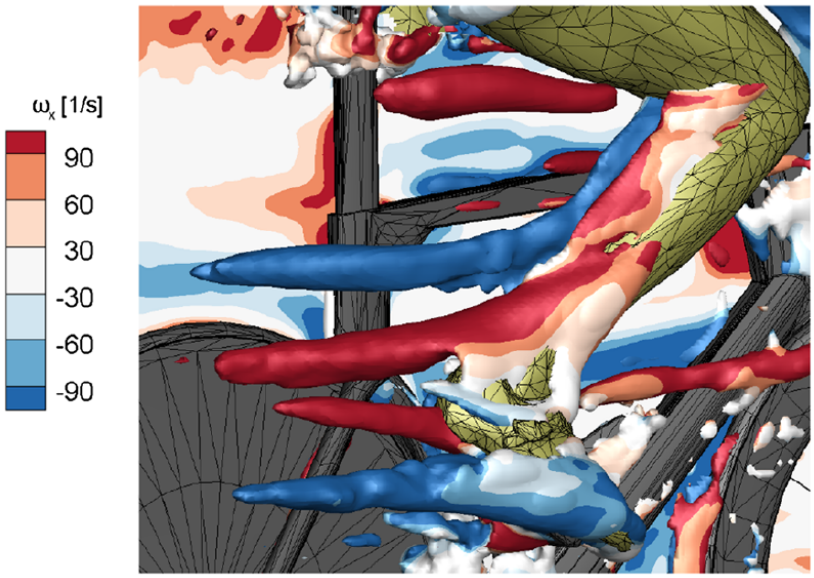

Figure 3.4: Q-criterion colored by ω_x showing the presence of flow structures adapted from Jux et al., 2018

symmetric geometry compared to the low-drag position.

3.3.2. Computational Fluid Dynamics (CFD)

The numerical investigation is performed with Reynolds Averaged Navier-Stokes (RANS) simulations. It was decided not to run a Detached Eddy Simulation (DES) or Large Eddy Simulation (LES) since these were found to be too computationally expensive to keep up the fast development cycle that a RANS solver could provide. Their benefits include the ability to resolve part of the turbulent scales instead of fully modeling these as is done in a RANS simulation. However, the added cost associated with the modeling improvements was considered too large and would restrict the investigation in drag reduction methods severely while it was assumed that the additional accuracy would not justify this.

For the following investigation, only the time-averaged solution will be sufficient in the discussion of the flow structures. The reason for this is twofold. First, the aim of this investigation is to find a drag reduction that is effective continuously. Moreover, the objective is to reduce the overall drag instead of finding an understanding of the way the flow is manipulated at an instantaneous level. Second, the measurement technique used in the research of Jux et al., 2018, being the validation data, only represents the time-average solution instead of the instantaneous solution. The measurement technique used has a low temporal resolution and is therefore limited in capturing instantaneous information. Hence, it makes more sense to compare the assumed steady-state solution of a RANS simulation with the time-average solution of the data set of Jux et al., 2018.

3.4. Experimental methodology

To verify the working mechanisms observed in the numerical simulations, a full-scale wind tunnel experiment was used. To capture information on the drag force and flow structures in an experimental simulation several methods exist. For example, balance measurements in the research of cycling aerodynamics have been used by Crouch et al., 2014, Terra et al., 2016b, Terra et al., 2019 among others. The benefit of this setup is the relative simplicity and time efficiency at which the measurements can be performed. However, the main limitation is that information on the wake itself is not captured. Hence, the reasoning behind measured variations in drag remains unknown.

To reduce this information gap, literature discusses the use of different flow visualization techniques and pressure measurements. These include oil flow visualisations (Crouch et al., 2014), surface pressure measurements (Crouch et al., 2014), wake rake measurements (Crouch et al., 2014) and Particle Image Velocimtery (Terra et al., 2016a, Jux et al., 2018, Terra et al., 2019 among others).

Since the objective of this thesis is to achieve drag reductions through flow manipulation, a connection between measurements done through a balance system and the visualization of the flow is made. Both methods will contribute to explaining the observed discrepancy in drag. The methodology of the balance measurements and flow visualization technique is discussed next, arguing why these methodologies contribute to the understanding of the working mechanisms of the drag reduction methods.

3.4.1. Balance measurements and crosswind simulations

Aerodynamic forces and moments can be measured with a six-component balance. The literature describes this as an accurate and reliable method to measure the drag force. Nonetheless, sources describe more measurement techniques capable of finding the drag force in the context of cycling aerodynamics. An example is the evaluation of the momentum deficit in the wake of a cyclist as is explained by Terra et al., 2019 using large-scale PTV. The measurement sensitivity compared to a force balance is, however, limited to 30 drag counts (Terra et al., 2019). A similar method was employed in an on-site environment discussed by Spoelstra et al., 2019.

Since the accuracy of the drag measurements for the research in this thesis is more important use will be made of a balance system. Furthermore, a balance system is less complex and provides flexibility to not only measure the drag component but also the other two force components and all three moments.

Combining a balance with a turntable allows us to measure the drag force in crosswind conditions. As is discussed by Barry, 2018, a cyclist in a competitive environment rarely experiences a perfect headwind. By rotating the cyclist model in the wind tunnel the forces can be measured for any crosswind angle. This is important as the drag reduction methods are based on the manipulation of the flow structures which are expected to be dependent on the crosswind angle. The effectiveness of the drag reduction methods for a range of crosswind angles is evaluated with a turntable resulting in a more realistic representation of the overall effectiveness.

To easily evaluate the combined effectiveness for a range of crosswind angles Barry, 2018 has introduced a weighted drag area using a weight parameter for each crosswind angle. Each weight is based on the probability of a crosswind angle to occur. The weighted drag area is computed with Equation 3.1.

$$C_D A = \frac{\sum_{j=1}^{n} w_j \cdot C_D A_j}{\sum_{j=1}^{n} w_j} \tag{3.1}$$

Barry, 2018 also provides the weights (w_j) for a cyclist riding at 11.18 m/s (40.23 km/h) assuming a wind speed of $U_w = 3.13$ m/s. For each crosswind angle, the road speed and wind speed remain constant resulting in a varying freestream velocity for each crosswind angle.

For this investigation, it was decided to use these weights (shown in Table 3.1) since the velocities at which the numerical and experimental simulations are tested are close to what was used by Barry, 2018 and are expected to be almost identical if computed separately. Additionally, the wind speed of $U_w = 3.13$ m/s was found to agree with typical wind speeds described in literature measured at vehicle height (Barry, 2018).

Table 3.1: Weights adapted from Barry, 2018 and freestream velocity for a wind speed of $U_w = 3.13$ m/s and bike velocity of 11.18 m/s. The function is symmetric about 0°

Crosswind angle [°]	0	2.5	5	7.5	10	12.5	15	17.5	20
Weighting factor (w) [-]	1.000	0.952	0.857	0.683	0.543	0.377	0.237	0.158	0.090

3.4.2. Particle Image Velocimetry (PIV)

As discussed before, the objective of this thesis is to understand the working mechanisms behind the drag reduction methods. Hence, any differences in the wake must be visualized in order to argue the reasons behind these variations in the drag. Particle Image Velocimetry (PIV) is often used to evaluate a flow field in a 2D setup measuring, for example, two (planar PIV) or three (stereoscopic PIV) velocity components. Volumetric measurements are referred to as tomographic PIV and require a complex setup. However, this method is limited in the measurable volume and requires the setup to be displaced and re-calibrated to expand the measurement domain. Other techniques, such as hotwire and Laser Doppler Anemometry (LDA), only provide flow field information at the probe location, limiting their capability to provide flow field data on a global scale.

A measurement technique such as a wake rake is capable of measuring at higher frequencies and can deliver volumetric information when considering the time-average solution as was demonstrated by Crouch et al., 2014. However, it is intrusive and depending on the rake used, lacks spatial resolution. Therefore, it was decided to focus on PIV instead, because of its ability to provide volumetric flow field information without disturbing the flow. Next, the working principles of PIV will be discussed.

Working principles

A detailed explanation of the workings of PIV is given by Raffel et al., 2018. The working principle of PIV starts with the injection of particles in the flow. The particles are illuminated by a pulsing laser sheet of which the time interval is known. With a camera, images are captured of the illuminated region at a known time interval to capture the illuminated flow field. The cameras have to be calibrated to be able to relate the particle image displacement with the tracer particle movement. By capturing the motion of the particles a velocity field can be reconstructed. A schematic of a 2D PIV setup can be found in Figure 3.5.

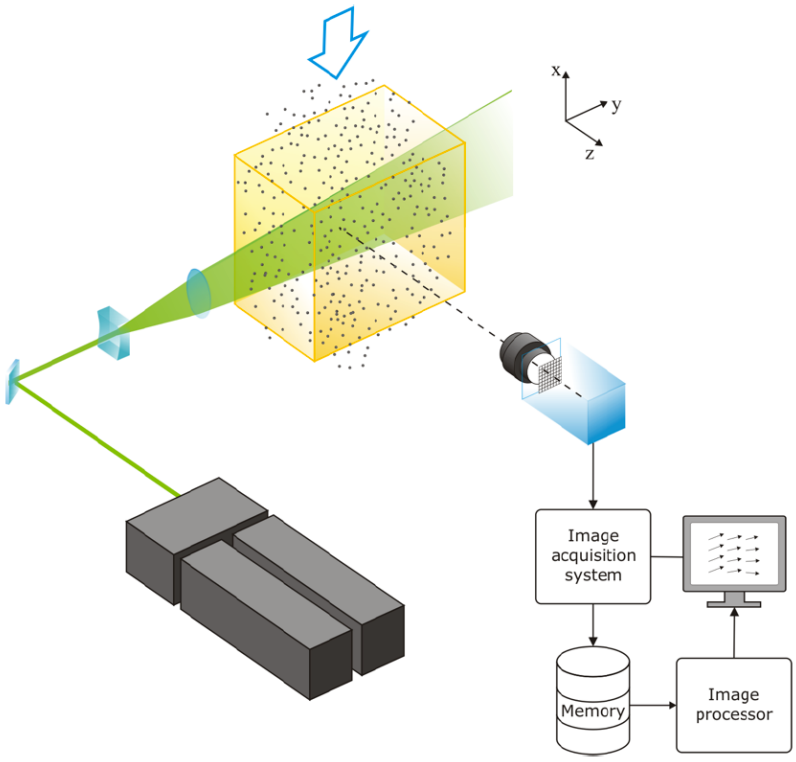

Figure 3.5: Schematic of PIV setup adapted from Scarano, 2013b

To obtain the velocity field from the raw images, a series of processes are required. First, the mea-

surement domain is divided into smaller volumes called interrogation windows after the data has been recorded. Furthermore, Jux, 2017 describes two different methods to extract velocity information from the raw images. These are particle-based approaches and correlation-based methods. Moreover, particle-based approaches build tracks based on the motion of individual particles. Hence, the seeding density per interrogation window is limited as the individual particles become more difficult to track with an increasing number of particles. Whenever this method is used for the visualization of a fluid it is often referred to as Particle Tracking Velocimetry (PTV).

For correlation-based methods, the movement of the particles is cross-correlated between two time steps resulting in a 2D vector field. This principle can be expanded towards a 3D vector field with tomographic PIV. This requires the illumination of a volume instead of a plane. A tomographic reconstruction (Elsinga et al., 2006) of the individual measurements is required before the cross-correlation analysis is performed.

A limitation of PIV is the relatively small measurement domain. The setup can be displaced but this is time inefficient and error sensitive. The use of Helium-Filled Soap Bubbles (HFSB) as tracer particles was introduced by Bosbach et al., 2009 and enabled the visualization of the flow field in large-scale experiments. Caridi et al., 2016 mention that the light scattered from HFSB is $10^4 - 10^5$ times more intense for bubble diameters in the submillimeter range making them effective as flow tracers in larger volumes. However, as tomographic reconstruction is computationally expensive, a more efficient method to reconstruct the flow field named Shake-The-Box (STB, Schanz et al., 2013) was introduced. Terra et al., 2019 have used HFSB in a PTV experiment to estimate the drag of a cyclist using wake flow field information. The setup of this experiment can be found in Figure 3.6.

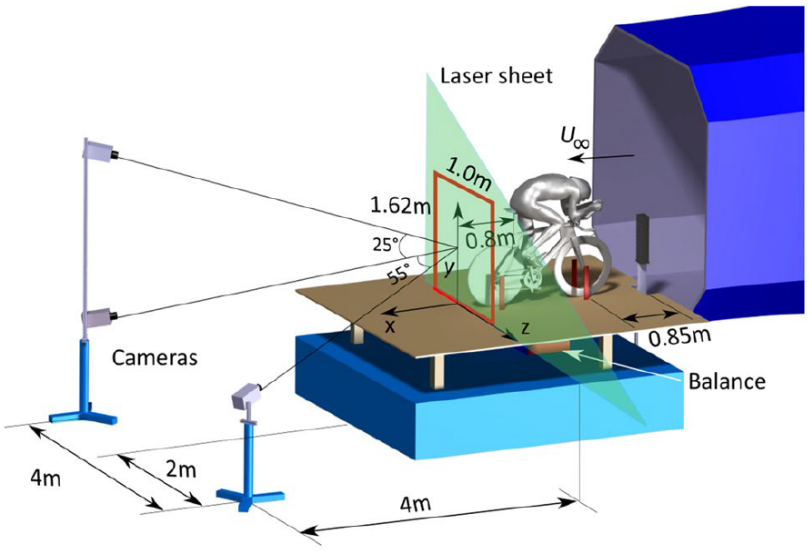

Figure 3.6: Experimental large-scale PTV setup adapted from Terra et al., 2019

A tomographic setup using HFSB would unfortunately result in a too-small measurement volume to capture enough information to visualize the variations in the flow topology for the drag reduction methods. A more effective approach would be the use of Coaxial Volumetric Velocimetry (CVV) as introduced by Schneiders et al., 2018 which is explained next.

Coaxial Volumetric Velocimetry

To increase the measurement domain and the ability to capture the flow field in complex regions, a system named coaxial volumetric velocimetry is introduced (Schneiders et al., 2018). The benefits of this system compared to tomographic PIV include the possibility to evaluate the 3D flow topology of complex geometries in large volumes. Furthermore, flow information close to the model can be captured providing information on the formation of the flow structures and location of flow separation.

The CVV system uses 4 cameras that are positioned closely together. The measurement volume is illuminated by a light source positioned between the 4 cameras. The volume measured by the 4 cameras is larger compared to what tomographic PIV can capture. A schematic overview of the CVV system can be found in Figure 3.7 showing the illuminated measurement volume indicated with a red dashed line.

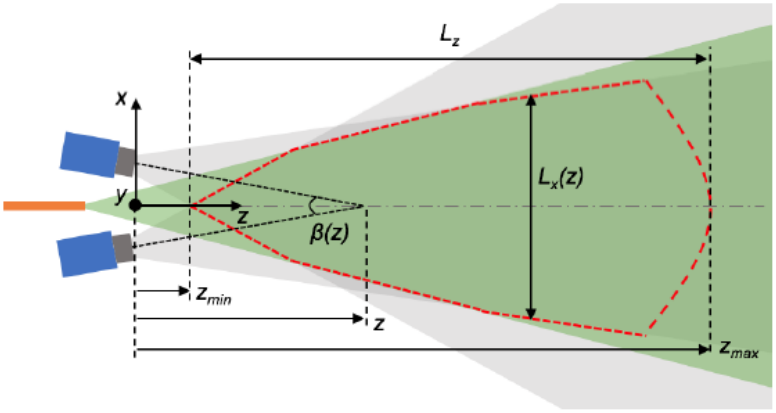

Figure 3.7: Schematic of the CVV system with top two cameras in blue showing the respective field of view in grey. The illuminated region is shown in green with a dashed outline showing the measurement volume. Adapted from Schneiders et al., 2018

A major difference compared to the tomographic setup shown in Figure 3.6 is the smaller tomographic aperture (β). The cameras can therefore be bundled together in a smaller body. This allows it to be attached to a robotic arm for easy positioning (Schneiders et al., 2018). An example of the CVV probe can be found in Figure 3.8 together with the UR5 robotic arm attachment location.

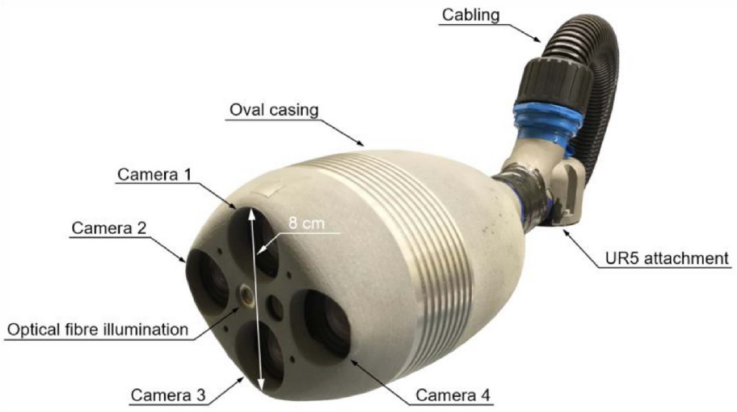

Figure 3.8: CVV probe with four cameras bundled in a single housing adapted from Jux et al., 2020

Similar to a tomographic PTV experiment, tracer particles are injected into the flow which are illuminated with a laser. The laser light is transported from the laser head to the CVV probe using an optical fiber. Schneiders et al., 2018 mention that particle image intensity (I_p) scales with the fourth order to the distance of the tracer as $I_p \propto z^{-4}$. As a result, the maximum depth (z_{max}) is limited by the particle image intensity.

Terra et al., 2020 mention that the measurement volume is a conical shape with cross-sections of 10 cm and 40 cm at 20 cm and 60 cm measured from the probe respectively. The exact size, however, can vary depending on the crop factor applied to the sensor as will be explained in chapter 5.

The low tomographic aperture results in a larger in-depth uncertainty compared to a tomographic setup

as is discussed by Scarano, 2013a. Both Jux, 2017 and Schneiders et al., 2018 mention an uncertainty of $\epsilon_x = \epsilon_y \leq 0.1$ mm and $\epsilon_z \leq 1$ mm. Hence, it can be expected that the uncertainty in the depth direction is about 10 times larger than in the other two directions.

By combining individual measurements a large time-average visualization of the flow field is constructed. Scarano et al., 2021 also mention that CVV is not well-suited for the evaluation of the instantaneous flow field because of the relatively low temporal resolution. However, for this research, only the time-average solution is measured as was discussed before. Additionally, Scarano et al., 2021 discuss that the spatial resolution is limited to approximately 1 vector per cm^3 compared to the expected 1 or more vectors per mm^3 for tomographic PIV. Nonetheless, the scales of the previously discussed hip and elbow vortices for a cyclist are expected to be large enough and easily detectable with CVV.

The discussed principles make CVV very suitable for the evaluation of the 3D flow topology of a cyclist. The system is not in requirement of having to be re-calibrated every time the probe is re-positioned because of the use of a robotic arm making the operation more time-efficient. An example of a complete setup using large-scale robotic PTV to measure the 3D flow topology in the wake of a cyclist can be found in Figure 3.9.

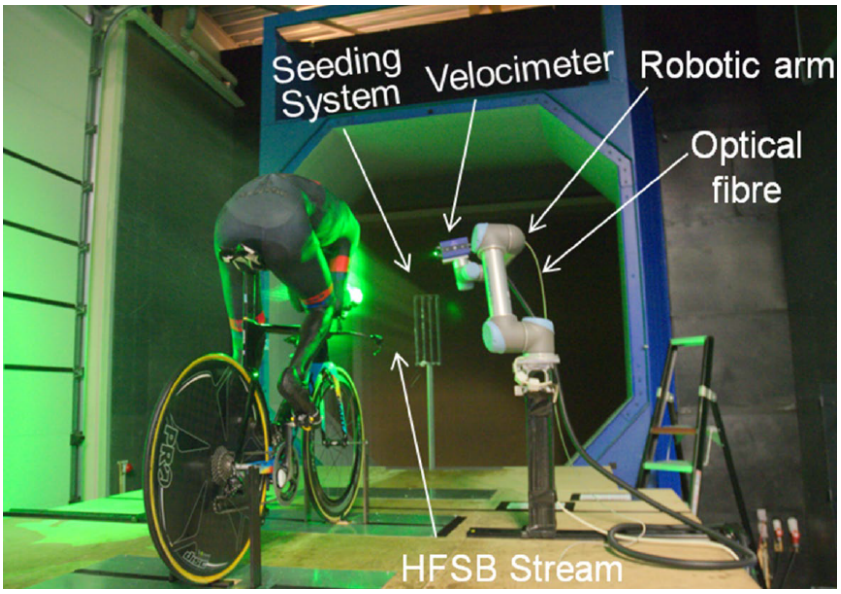

Figure 3.9: Example of a large-scale robotic PTV experiment. Note that the probe used in this experiment uses a different housing as this is an older version than the version shown previously. Adapted from Jux et al., 2018

4

Numerical Setup

To examine the potential of the proposed drag reduction methods, each was evaluated numerically and compared with the baseline configuration. Based on the results of this investigation the most promising designs were then further developed and tested in a wind tunnel experiment. This chapter will focus on explaining the details of the numerical setup that was used to evaluate both drag reduction methods introduced in the previous chapter.

First, the CFD setup is discussed. Then, an explanation of the numerical cyclist model and the experimental data used to verify the physicality of the numerical results is given. Next, the results of a mesh study are discussed as well as the impact of this on the correlation of the flow structures to the wind tunnel results. This is followed by a discussion on the convergence and solution averaging. Finally, the processing of the data is discussed.

4.1. CFD setup

The following section will discuss the numerical setup. First, a discussion on turbulence modeling is provided. Next, a discussion on the initialization and averaging of the solution is given. The section concludes with a discussion of the setup used to run crosswind simulations.

4.1.1. Numerical schemes and turbulence modeling

For this investigation, the open source CFD package *OpenFOAM* was utilized. Using the SIMPLE algorithm to couple the pressure with the velocity, a finite volume method was employed to compute the solution. For the interpolation, second-order schemes were used together with relaxation schemes to ensure stability. The divergence and gradients were all discretized using second-order schemes.

The solutions were generated using an incompressible Reynolds Averaged Navier-Stokes (RANS) solver. The turbulence was modeled using the $k-\omega\ SST$ model (Menter et al., 2003) similar to what Griffith et al., 2014 used in their numerical research on the effect of leg position on cyclist aerodynamic drag. Furthermore, Defraeye et al., 2010 recommend using this turbulence model in the evaluation of the flow field in cycling. It is mentioned that this model provides the best overall performance compared to other turbulence models for RANS simulations.

4.1.2. Initialisation and boundary conditions

The simulations were initialized from a potential solution which is computed using OpenFOAM's built-in potential solver. Simulations were performed at a freestream velocity (U_∞) of 15 m/s. The remaining parameters were simulated to represent the wind tunnel setup of the experimental data as well as possible. This meant that the wheels and legs were simulated in the static, high-drag, position. Although this does not completely replicate a moving cyclist, it does reduce discrepancies with the available wind tunnel results. Moreover, the areas of interest are focused around the cyclist's torso, which is assumed to be sufficiently far from the ground as well as the legs, such that it is expected that this will have a small impact on the physicality of the position of the flow structures when compared to a moving cyclist which was discussed in section 2.2.

4.1.3. Crosswind simulations

To run an analysis on the performance of the drag reduction methods for crosswind conditions the setup of the CFD simulation had to be slightly changed. For this investigation, it was decided to rotate the domain and the inlet to simulate the cyclist experiencing crosswind conditions. Conditions between -20° and 20° with steps of 5° were simulated for both drag reduction methods to investigate the response. Using the weight function discussed in subsection 3.4.1 the weighted drag area was computed allowing us to compare the performance of the drag reduction methods against the baseline. An overview of the weight factors and changing bike velocity as a result of the rotating domain with constant freestream velocity is shown in Table 4.1.

Table 4.1: Overview of the weight factors applied at the various crosswind conditions and the changing bike velocity for a constant freestream velocity of $U_\infty = 15$ m/s. Only positive crosswind angles have been included as the results are symmetric for the negative angles

Crosswind angle [°]	0	5	10	15	20
Weighting factor (w)	1.000	0.857	0.543	0.237	0.090
Bike velocity [m/s]	15.0	14.9	14.8	14.5	14.1

4.1.4. Convergence and solution averaging

The simulations were left running for 2000 iterations. Inspection of the convergence of the drag area indicated that the solution would become stable after around 1000 iterations. It was decided to average the flow field and aerodynamic forces for the final 500 iterations.

4.2. Cyclist model and geometrical domain

Using *Blender*, an open-source CAD program, digital models of the drag reduction methods were developed. These were integrated with a cyclist model for which a digital model of Tom Dumoulin in TT position was used. This digital model was constructed with scanning data. Terra et al., 2019 provide the frontal area of 0.32 m^2. Furthermore, Jux et al., 2018 have used this model in a full-scale wind tunnel experiment where the 3D flow topology was carefully mapped using robotic PTV. Their results were found to agree with other literature sources such as Crouch et al., 2014. An example of the digital model of Tom Dumoulin can be found in Figure 4.1.

The numerical results of three configurations, a baseline, HVC, and wingsuit configuration will be discussed in chapter 6. Examples of the CAD models of the HVC and wingsuit can be found in Figure 3.1 and Figure 3.2 respectively.

The cyclist model was placed in a computational domain measuring $L \times W \times H = 56 \times 31 \times 15$ [m]. This domain is larger than the computational domains used by Defraeye et al., 2010 and Blocken et al., 2019. This was useful to capture the flow field under crosswind conditions when rotating the domain.

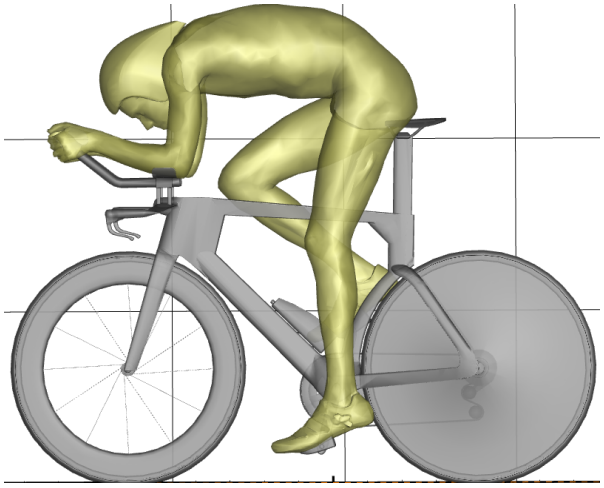

Figure 4.1: Model of Tom Dumoulin in TT position used in the numerical simulations

The availability of wind tunnel correlation data was extremely important to find that the CFD setup was providing a flow field of sufficient accuracy representing the experimental flow field. Terra et al., 2016a for example, mention the complexity of running sporting models in CFD and also place emphasis on the prerequisite of having validation data. An aspect that complicates the modeling of sports aerodynamics is the sophistication of the geometry. As a result of the bluff geometry of the model, the wake is anticipated to be highly turbulent and therefore unsteady. Hence, it can be challenging to find a physical solution for a steady-state solver like a RANS solver.

Therefore, the data set of Jux et al., 2018 was utilized to compare with the CFD results. Special attention was given to the position, size, and strength of the flow structures around the elbows and hips. Modeling choices such as the mesh settings can heavily influence the location of flow separation and the physicality of the wake development. By closely evaluating the results of Jux et al., 2018 these settings could be adjusted such that the baseline numerical solution would correlate well with the experimental results. Improving the correlation with the wind tunnel provided more certainty in the physicality of the solution. More importantly, it improves the certainty of finding drag-reduction methods that produce similar results in the wind tunnel and on the road.

As was discussed before, the cyclist model that is used during experimental testing of the drag reduction methods is not identical to the model used by Jux et al., 2018 and therefore the model that was used in the numerical tests. This may influence the effectiveness of the drag reduction methods when these are transferred to the wind tunnel model. Nonetheless, since the bike position between both models is very similar it is expected that the flow field and therefore the effectiveness of the drag reduction methods are comparable. Next, we will further discuss the correlation between the baseline results and the experimental simulations from Jux et al., 2018.

4.3. Mesh study and wind tunnel correlation

An investigation was performed on the agreement between the position of the flow structures found in the numerical simulations and the wind tunnel. The majority of the modeling improvements in CFD were done through the manipulation of the mesh settings. The mesh was generated using OpenFOAM's built-in meshing tool named *SnappyHexMesh*. Systematic changes were made to the generation of cells, adding refinement in regions with large velocity gradients which was followed by an analysis of the variation in the wake structures.

A baseline numerical setup, building on prior experience, was tested and functioned as a starting point. Focus was put on the total number of cells and therefore total computation time. As the number of cells heavily influences the latter this should be kept to a minimum to keep iteration cycles manageable.

From the initial results, it became clear that the presence of the hip and elbow structures with the wind tunnel was well captured in CFD. However, their strength and position were slightly off. A comparison of the flow topology between the wind tunnel result and the initial CFD result can be found in Figure 4.2. The flow topology has been visualized with iso-surfaces of the non-dimensional streamwise vorticity. The results were made non-dimensional with the freestream velocity (U_∞) and the torso chord which Terra et al., 2020 have reported as $c = 0.7$ m for this model.

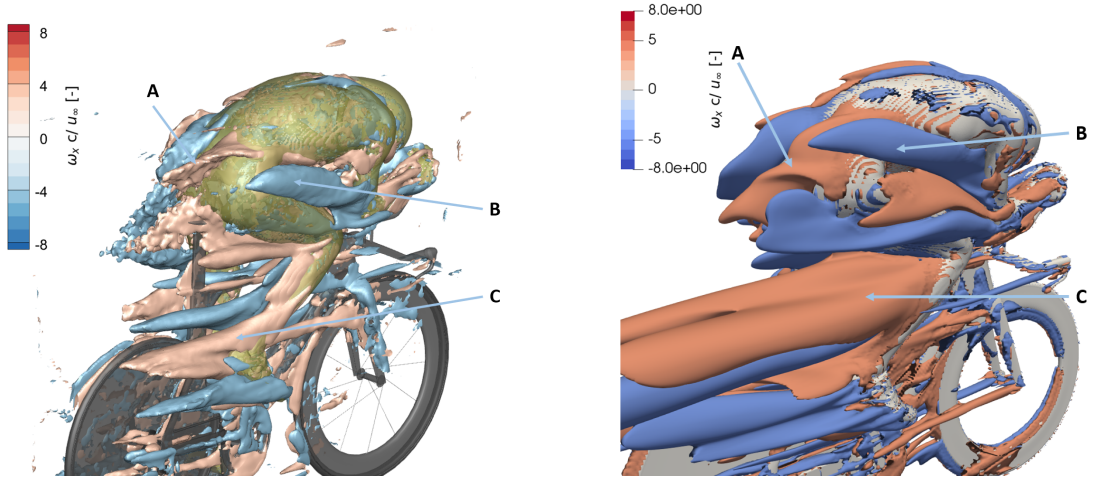

(a) RHS view showing iso-surfaces of non-dimensional vorticity. Data is adapted and re-processed from the wind tunnel experiment of Jux, 2017

(b) RHS view of coarse-mesh CFD result showing iso-surfaces of vorticity

Figure 4.2: Comparison of position and strength of the vortex structures between the wind tunnel and CFD. Both figures show iso-surfaces of non-dimensional streamwise vorticity at $\omega_x c/U_\infty = \pm 4$ [-]

Three miscorrelations on the RHS stand out where the LHS was found to correlate better. First of all, the right-hand side hip vortex (A) is over-estimated. Second of all, the lower elbow vortex (B) is too powerful and persists much further downstream than the wind tunnel suggests. Finally, the positive (red) knee vortex (C) is over-estimated in CFD. To improve the correlation with the wind tunnel a number of changes to the mesh recipe were made. First, the surface mesh settings of the cyclist were changed to improve the correlation of these structures with the wind tunnel and will be discussed next.

4.3.1. Surface mesh refinements

The first method used to improve the mesh quality and physicality of the simulation was to change the surface mesh refinement. Using rectangular-shaped cells on the surface, the size of the edges was scaled down to half its original size to increase the refinement of the surface cells.

The refinement of the surface mesh of the cyclist resulted in cells with edge lengths of 2 mm. By refining the surface mesh on the cyclist the previously discussed miscorrelations were found to improve. The results can be found in Figure 4.3.

From Figure 4.3b small improvements are found in the size of the RHS hip vortex (A). However, its position can still be improved. Furthermore, the lower RHS elbow vortex (B) did not show any large difference from the initial result. Finally, the positive knee vortex (C) has reduced, and the flow topology correlates much better with the wind tunnel.

Table 4.2: Overview of the number of cells and solver time for each mesh update

Mesh option	Number of cells [-]	Solver time per iteration [s]	Average y^+ [-]	$C_D A$ [m^2]
Baseline	24.0e6 cells	21 s	17.86	0.1735
Surface refinement	26.3e6 cells	23 s	11.23	0.1792
Prism layer refinement	27.9e6 cells	25 s	9.89	0.1861

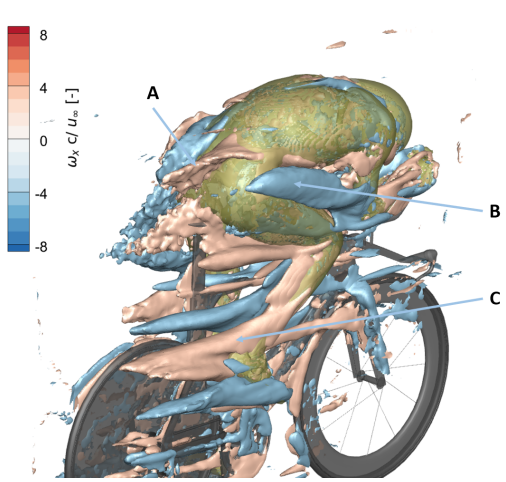

(a) RHS view showing iso-surfaces of non-dimensional vorticity. Data is adapted and re-processed from the wind tunnel experiment of Jux, 2017

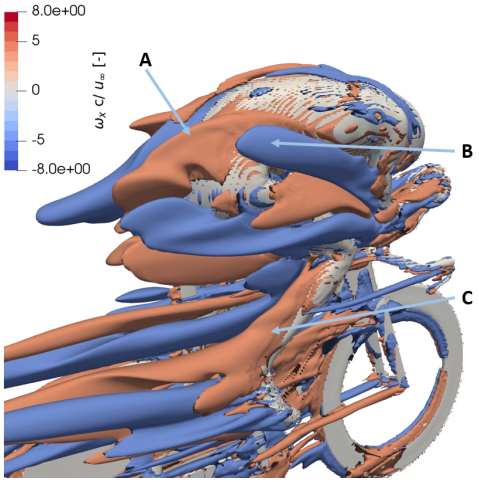

(b) RHS view of CFD result with refined surface mesh showing iso-surfaces of vorticity

Figure 4.3: Comparison of position and strength of the vortex structures between the wind tunnel and CFD. Both figures show iso-surfaces of non-dimensional streamwise vorticity at $\omega_x c/U_\infty = \pm 4$ [-]

Finally, Table 4.2 shows that the surface refinement added 2.3e6 additional cells. The effect on the solver time per iteration was found to be an additional 2 seconds as a result of the additional cells. Furthermore, the average y^+ was reduced from 17.9 to 11.2.

4.3.2. Prism layer refinements

After the mesh settings of the surface refinement had been adjusted, the flow field sensitivity to the prism layers was investigated. The baseline case used 3 prism layers on the surface of the cyclist. An additional layer was added to the refined surface mesh. The effect of the additional layer on the flow field can be found in Figure 4.4b. The first layer height was determined based relative to the edge length of the corresponding surface mesh cells. Hence, the y^+ was independent of the prism layer sensitivity study as the surface mesh was not changed.

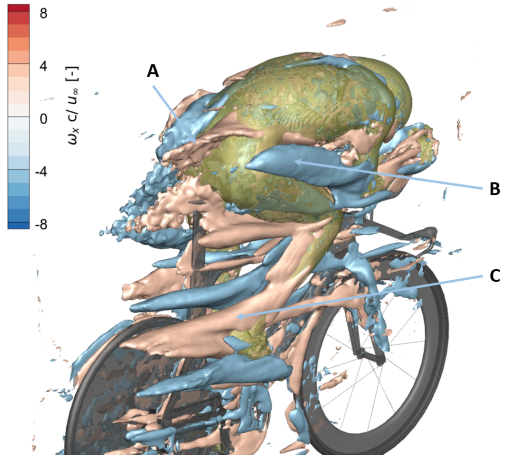

(a) RHS view showing iso-surfaces of non-dimensional vorticity. Data is adapted and re-processed from the wind tunnel experiment of Jux, 2017

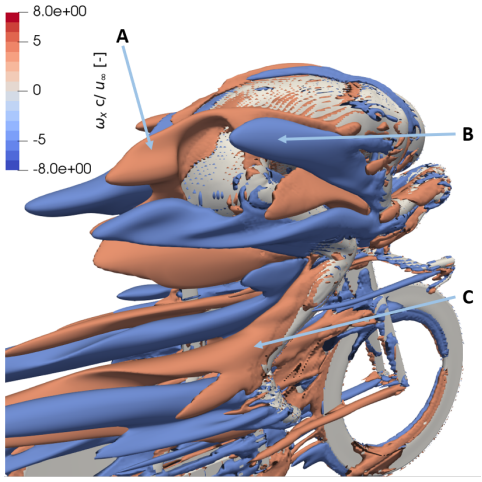

(b) RHS view of CFD result with additional prism layer showing iso-surfaces of vorticity

Figure 4.4: Comparison of position and strength of the vortex structures between the wind tunnel and CFD. Both figures show iso-surfaces of non-dimensional streamwise vorticity at $\omega_x c/U_\infty = \pm 4$ [-]

The result shows that the RHS hip vortex (A) correlates better with the WT result. The lower RHS

elbow vortex (B) has slightly reduced in size. The position of the knee vortex (C) remains unchanged compared to the result in Figure 4.3b. This change required 1.6e6 additional cells resulting in 2 seconds per iteration additional solver time as is shown in Table 4.2. Nonetheless, because of the improved hip vortex correlation with the wind tunnel, it was decided to keep these mesh settings in the development of the drag reduction methods.

Additional prism layer refinements were tested. However, the flow field correlation with the WT results was not found to improve similar to the previous two mesh changes. Moreover, it was found that the drag area was converging as the number of prism layers on the cyclist increased. The result of the number of prism layers on the drag area can be found in Figure 4.5. Terra et al., 2019 had measured a drag area of 0.237 of the same model in a wind tunnel experiment. Although CFD underestimates the drag area this was found to be consistent with the literature when comparing CFD with wind tunnel results as discussed by Griffith et al., 2014. Similar to this numerical simulation it is expected that part of the discrepancy between the measured drag area in the wind tunnel and CFD is due to simplifications in the numerical model. Furthermore, as was shown before the flow topology still shows some miscorrelation with the wind tunnel which is expected to contribute to the difference in drag area.

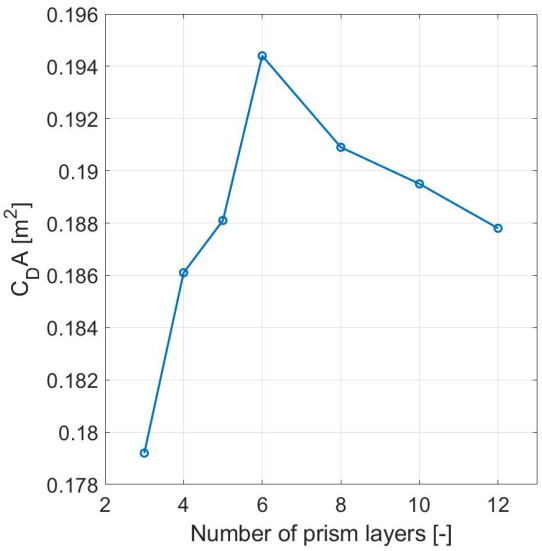

Figure 4.5: Effect of number of prism layers on the cyclist model on the measured drag area

Since the focus of this investigation is not on finding the correct absolute drag value it was decided to not further increase the number of prism layers to keep the solver times to a minimum. Furthermore, the measured variations in drag between a drag reduction method and the baseline and the physicality of the corresponding flow field changes are considered more important in this research than the absolute correlation with the wind tunnel results. Finally, an example of the final mesh configuration can be found in Figure 4.6

4.3.3. Flow field correlation of numerical simulations with robotic 3D PTV

The previous discussion on the correlation of the flow structures of the numerical results has only been realized because of the availability of the 3D flow field data from Jux et al., 2018. This demonstrates the great advantage of running 3D PTV compared to regular PIV experiments when afterwards, the data is used to compare with numerical results.

The availability of the 3D data provides more certainty in the position and strength of the flow structures when compared with CFD results. Planar or tomographic PIV, as was discussed in chapter 3, will only provide limited flow field information in a plane or a small volume. However, when numerical simulations are used for low-speed aerodynamic development such as for cycling, it is very important that the flow

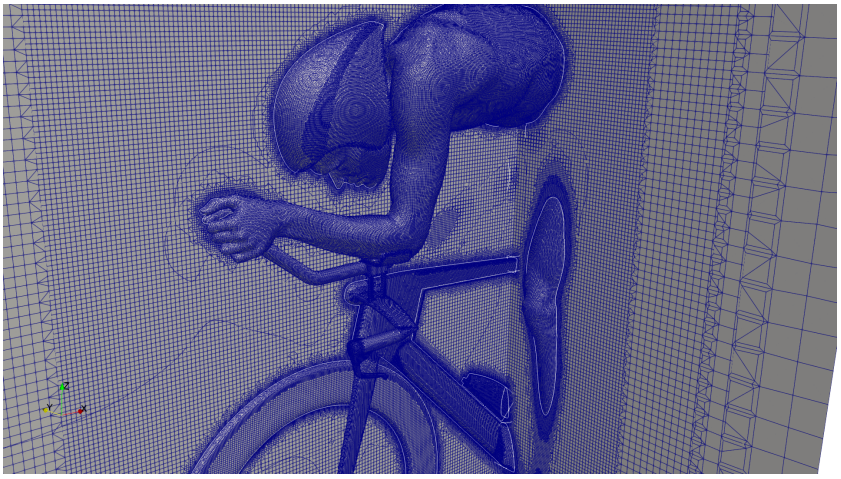

Figure 4.6: Example of the final mesh recipe

topology can be verified. Especially for RANS simulations which can struggle to find physical solutions for a highly unsteady flow field, benefit from having experimental data on the 3D flow topology.

This example of finding an improved correlation with the wind tunnel shows that the added information on the 3D flow topology measured using 3D PTV can provide greater certainty in the validity of the CFD simulations. Moreover, the flow topology in a numerical simulation may gradually improve as mesh and boundary settings are adapted meaning that different flow structures may appear or change position for different mesh recipes. Hence, the validation of just one flow structure does not mean the remaining structures correlate with the wind tunnel. Therefore, the added flow field information of 3D PTV can extend the accuracy of numerical simulations as these provide an opportunity to validate the flow topology throughout a much larger domain. This is a unique opportunity in the validation of numerical simulations and could therefore be a valuable addition to aerodynamic development with numerical simulations.

4.4. Data processing and analysis

The processing of the data was done in *ParaView*, an open-source data visualization application. The visualization of the flow was done using the average solution. Furthermore, flow structures were visualized using the Q-criterion colored by vorticity as discussed in section 2.1 and with iso-surfaces of vorticity as was shown before. Finally, the surface pressure was visualized using the pressure coefficient which is defined in Equation 4.1.

$$C_p = \frac{p - p_\infty}{\frac{1}{2}\rho U_\infty^2} \tag{4.1}$$

Iso surfaces of the Q-criterion were computed in a subset of the flow field to minimize computation times. Furthermore, the grid was subsampled to further improve post-processing times. The grid was kept fine enough to ensure the visualization of smaller flow structures.

5

Experimental Setup

The most promising designs of the HVC and wingsuit were tested in a wind tunnel experiment. The following chapter explains the experimental setup. First, a description of the wind tunnel facility is given. Next, the experimental apparatus is discussed. Then, the data acquisition procedures are explained. A discussion on the data processing techniques follows this. Finally, the experimental uncertainty is discussed.

5.1. Open Jet Facility (OJF)

The wind tunnel experiment was performed in the Open Jet Facility in the High Speed Laboratory at the Delft University of Technology. A 500 kW electrically powered fan drives the tunnel capable of reaching a velocity up to 35 m/s. The exit of the tunnel nozzle is an octagonal shape that spans 2.85 m both in width and height. At the back of the test section, cooling fins are positioned to keep the flow at a constant temperature. For this experiment, the temperature was set to 20° Celsius. The turbulence intensity has been measured to be around 0.5% (Lignarolo et al., 2014). However, for this experiment, this is expected to have been slightly larger because of the installation of a seeding rake in the settling chamber which will be explained in subsection 5.2.3.

The floor carrying the bike and cyclist model was positioned 20 cm above the nozzle exit to ensure it would be sufficiently far from the tunnel wall's boundary layer and jet's shear layers which Lignarolo et al., 2014 mention spread with a 4.7° angle. The CVV measurements were conducted at a freestream velocity of 14 m/s, similar to the experiment of Jux et al., 2018 and what is found to be a professional TT training velocity as reported by Lukes et al., 2005. The balance measurements were performed for a range of velocities to capture the Reynolds number effects.

5.2. Experimental apparatus

The experimental apparatus will be discussed next. All components that make up the experimental setup will be explained in detail.

5.2.1. Overview of the experimental setup

A schematic overview of the wind tunnel setup can be found in Figure 5.1. In this figure, the CVV probe and robotic arm are positioned on the RHS of the model.

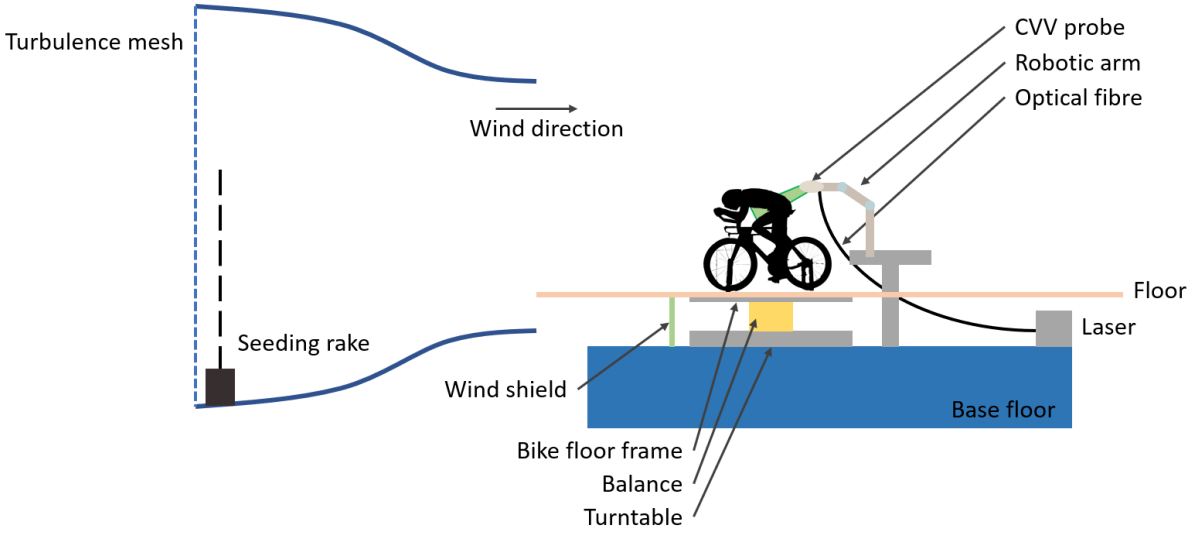

Figure 5.1: Side view of a schematic of the wind tunnel setup

From the figure, it can be seen that the cyclist model is positioned on the raised floor above the nozzle exit. Upstream of the balance, a windshield was installed to keep the balance from measuring the flow interacting with the bike floor frame which is attached directly to the balance. The robotic arm is connected to x95 beams which were secured directly to the base floor to keep vibrations to a minimum. The laser was positioned downstream and secured to the base floor. An optical fiber transported the laser light to the CVV probe.

An overview of the test section can be found in Figure 5.2. Here, the CVV probe is positioned on the LHS of the cyclist model. In addition, the seeding rake can be seen in front of the turbulence mesh in the settling chamber of the wind tunnel. The bike is connected to a frame on top of the balance using steel struts which are connected to the front and rear axles. The cyclist model is positioned on a circular floor which can be positioned independently of the remaining static floor parts, to simulate crosswind conditions. The distance between the circular and static floor was 5 mm.

5.2.2. Balance, turntable, and floor

A balance system combined with a turntable was used to measure the drag force in the straight-ahead condition and crosswind conditions. This system could rotate the model with an accuracy of 0.1 degrees in both directions.

The turntable was mounted onto the base floor. The balance was mounted on the turntable such that it would rotate with the model. The balance is a 6-component system, capable of measuring three force components along the three axes and moments around these three axes simultaneously. The balance was manufactured and calibrated by the Dutch Aerospace Laboratory and is capable of measuring a load up to 250 N in the streamwise direction with a maximum uncertainty of 0.06% (Alons, 2008). Finally, a frame that would carry the circular floor and the bike, was secured to the balance. An overview of this setup with the bike floor frame, balance, and turntable installed on the base floor can be found in Figure 5.3.

For the remaining part of the setup, a steel frame was installed around the balance that was connected to the base floor, carrying the static floor components. Both the balance and turntable were controlled with a PC in the control room.

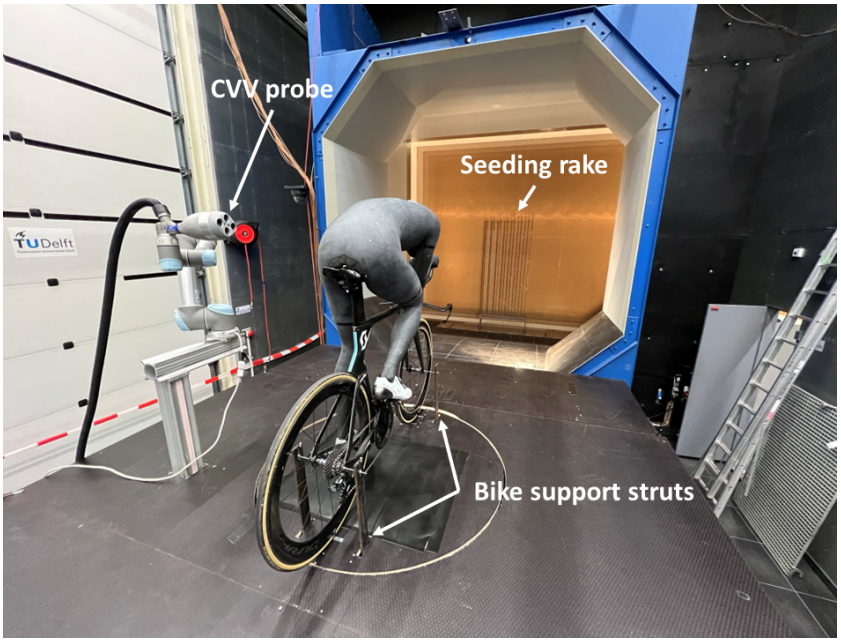

Figure 5.2: Overview of the experimental setup

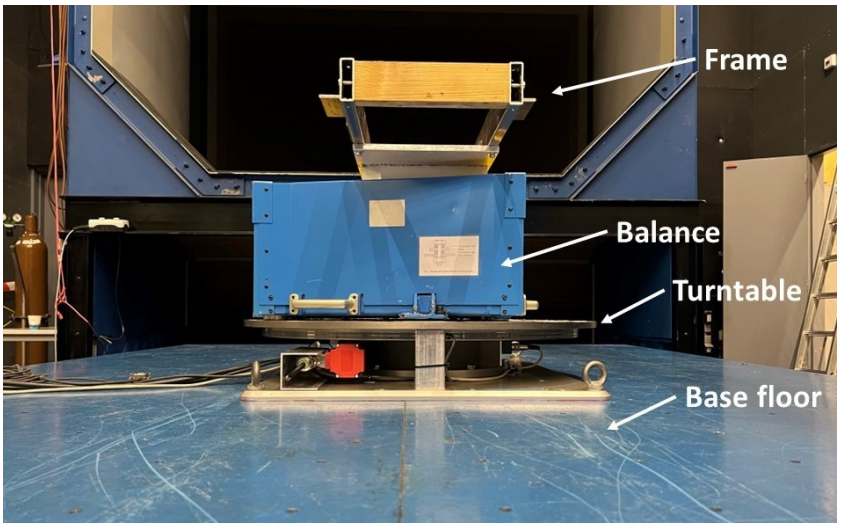

Figure 5.3: Overview of the turntable and balance setup

5.2.3. Robotic 3D-PTV

The CVV system is comprised of multiple components. The CVV probe was positioned in the measurement domain with a robotic arm of which the details are discussed next. Additionally, the seeding rake used during the experiment was operated for the first time during an experiment. Hence, details on the operational part are provided such that the experiment can be replicated. Finally, details on the camera settings of the CVV system and laser are explained.

Robotic Control Unit

The base of the CVV probe was connected to a robot head. The *Universal Robots - UR5* robotic arm was used to position the camera probe. The arm is capable of reaching 850 mm in each direction shaped like a spherical dome from the robot base. The base was connected to an x95 beam positioned 0.6 m downstream, -0.9 m laterally measured from the frontal axis of the bike to measure the on the

LHS of the model. The height of the robot base measured 0.65 m from the floor. To measure on the RHS of the model the robot base was moved to the other side changing to 0.9 m laterally. An overview of the distances to the seeding rake and the robot base from the GCM can be found in Figure 5.4.

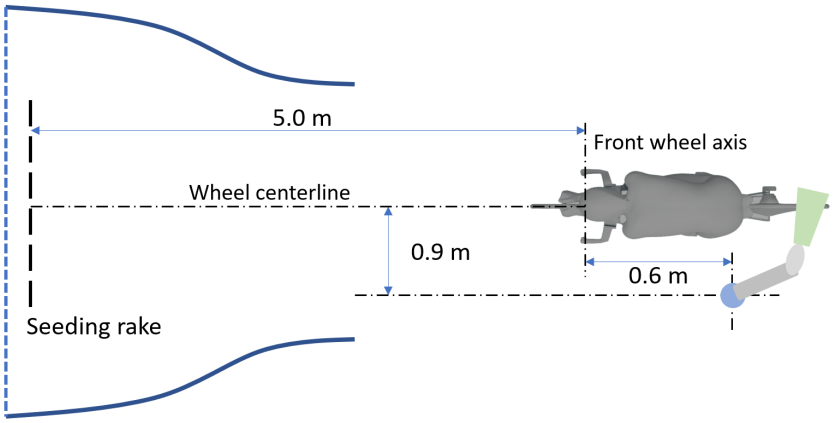

Figure 5.4: Overview of the dimensions between the robot base, seeding rake, and the GCM

The position of the robot head with respect to the base can be positioned by translating the head or rotating each of the joints individually. Each joint has a $\pm 360^{\circ}$ range. The manufacturer mentions an accuracy of the position of the robot head of ± 0.1 mm.

Robot positions were determined before the data acquisition and their locations were stored on a PC with a program named *RoboDK*. Each position was determined manually using the tablet placing the camera in the correct position after which the location was saved in *RoboDK* as a joint target. This operation would fix the joint positions for the location of the robot head. If for example, a sequence of robot positions is determined only by the location of the robot head, an arbitrary combination of joint positions may cause the robot to run into itself.

Finally, the measurement volume was estimated to be 0.45 m^3. An overview of the measured volume in the wake of the cyclist can be found in Figure 5.5.

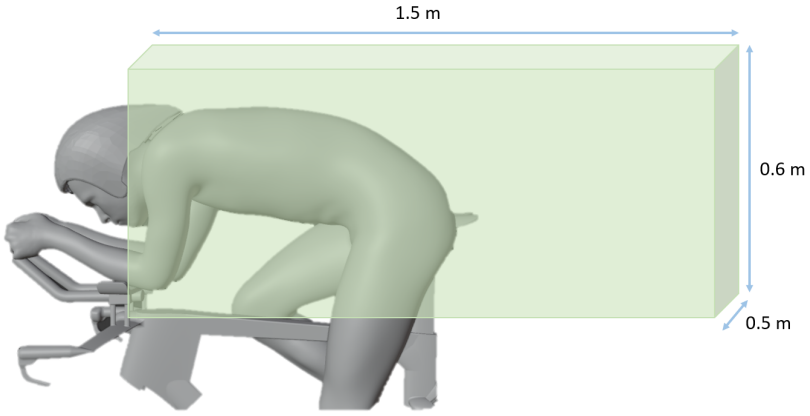

Figure 5.5: Measurement volume

Seeding rake

The seeding rake, used to generate the HFSB, was developed at the Faculty of Aerospace Engineering at the Delft University of Technology. Each nozzle is capable of generating 30,000 bubbles per second. The rake includes a total of 398 nozzles. However, for this experiment, only the rear half of the nozzles were operated to minimize the soap usage resulting in 216 active nozzles.

Only taking into consideration the active nozzles, the size of the seeding rake is 182 cm in height and 98 cm in width. With 27 nozzles in height and 8 nozzles wide the distance between each nozzle in height is 7 cm and in width is 14 cm. A close-up of the nozzles is shown in Figure 5.6.

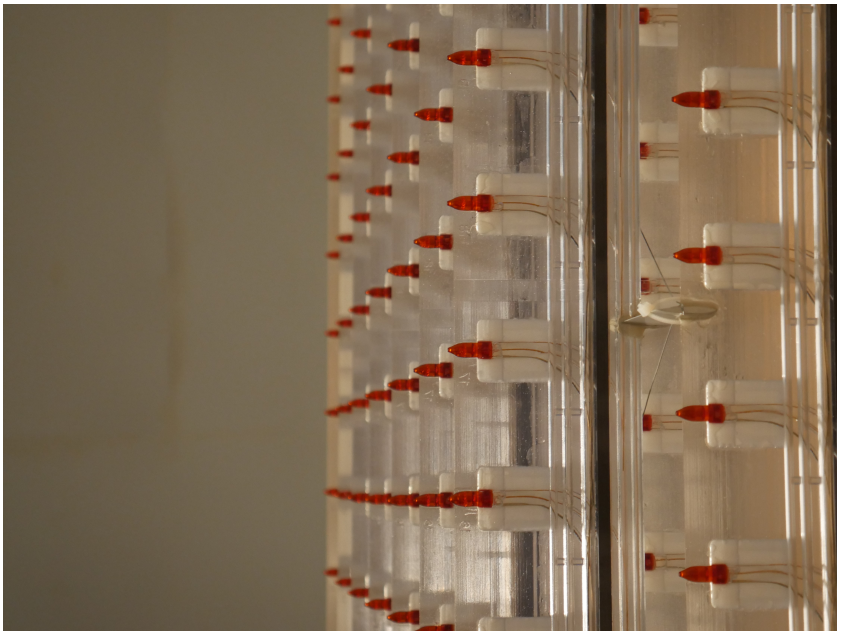

Figure 5.6: Side view of the seeding rake with nozzles used to generate the HFSB

The seeding density in the freestream was computed using the area between four nozzles (A_n) as shown in Equation 5.1a. Next, the volume flow rate ($\dot{V}$) was computed using Equation 5.1b. Here, u_n is the velocity in the settling chamber which is a third of the freestream velocity. Finally, the bubble density (C_{HFSB}) could be computed using Equation 5.1c.

$$A_n = d_{z_n} \times d_{y_n} = 7 \text{ cm} \times 14 \text{ cm} = 98 \text{ cm}^2 \tag{5.1a}$$

$$\dot{V} = A_n \times u_n = 98 \text{ cm}^2 \times 467 \text{ cm/s} = 45766 \text{ cm}^3/\text{s} \tag{5.1b}$$

$$C_{\text{HFSB}} = \frac{\dot{N}}{\dot{V}} = \frac{30,000}{45766} \frac{\text{bubbles/s}}{\text{cm}^3/\text{s}} = 0.65 \text{ bubbles/cm}^3 \tag{5.1c}$$

As discussed before, the seeding rake was positioned in the settling chamber of the OJF. This will affect the turbulence intensity in the freestream as discussed by Sciacchitano and Giaquinta, 2019. However, during their experiment, a slightly smaller seeder was used. Nonetheless, the seeding rake was positioned at the same location in the settling chamber as the seeder used during this experiment. Moreover, Sciacchitano and Giaquinta, 2019 measured a turbulence intensity of 0.8%. This was almost double the measured value without a seeding rake installed (Lignarolo et al., 2014). Nonetheless, this is still much smaller than the measured turbulence intensity of 1.9% discussed by Jux et al., 2018 where the seeder was placed at the nozzle's exit. For this experiment it is expected that the turbulence intensity is in a similar range as discussed by Sciacchitano and Giaquinta, 2019.

Operating procedure and seeding generation

Controlling the seeding rake is done with a Fluid Supply Unit (FSU) which is operated in the control room of the OJF. A helium and air mixture is combined with soap in a pressurized system. Individual pressure levels could be controlled with the FSU being the soap pressure, internal gas pressure, and external gas pressure. The values used during the experiment are shown in Table 5.1. An overview of the control panel of the FSU can be found in Figure 5.7.

Table 5.1: Pressure settings used during the experiment

Pressure setting	Pressure [bar]
Soap pressure	1.9
Internal gas pressure	2.0
External air pressure	2.0

Figure 5.7: Control panel of the FSU

Since both the FSU and seeding rake were used for the first time in an experiment, a brief overview of the operating procedure is given next. This procedure was found to give the best results and minimize soap usage.

1. Fill the soap reservoir with approximately 1.5 liters of soap. This should allow you to run the seeder for over an hour with only half the nozzles being active.
2. Pressurise the system and the soap reservoir.
3. Have the wind tunnel running at approximately 10 m/s.
4. Open the He valve, V11, to allow helium to enter the system.
5. Open the air and helium valves, V1 and V3 respectively, and wait for the actual soap pressure gauge to settle to around 1.85-1.95 bar.
6. Open the soap valve, V2, and give the system a couple of seconds to reach a homogeneous distribution of soap bubbles before starting the measurements.

After the experiment, the soap return valve should be opened for a couple of seconds to allow any remaining soap in the system to return to a reservoir at the FSU to reduce the soap losses. Finally, an example of the seeded volume can be found in Figure 5.8.

Imaging system and illumination

The imaging system used to capture the flow field is similar to the system described by Jux et al., 2020. This system is named the LaVision *MiniShaker Aero* coaxial volumetric velocimeter. The technical specifications of the camera system have been summarised in Table 5.2.

The acquisition frequency was kept at 821 Hz, similar to what was used in the experiment of Jux et al., 2020. Increasing the acquisition frequency resulted in a cropped sensor size and reduced the

Figure 5.8: Example of the seeded flow with HFSB

Table 5.2: Technical specifications of the LaVision *MiniShaker Aero*

Optics			Minishaker Aero
	Focal length	f_i	4 mm
	Camera aperture	$f_\#$	11
Imaging			
	Tomographic aperture	β	8° horizontal 4° vertical
	Active sensor size	S_x x S_y	640 x 476 pixels
	Pixel pitch	Δ_{px}	4.8 μm
	Magnification (at z_0 = 40 cm)	M	0.01
	Digitial image resolution (at z_0 = 40 cm)	r	2.1 pixels/mm
	Bit depth	b	10
	Acquisition frequency	F	821 Hz

camera field of view. Changing the frequency also changes the particle displacement between frames. Furthermore, the particle displacement also varies with object distance where particles closer to the camera tend to move faster compared to particles further away. For this experiment, it was decided to capture a set of 10,000 images at each measurement position resulting in an acquisition time of 12.2 s.

For the given freestream velocity and acquisition frequency we find that a particle moves 17 mm between two frames. Using the magnification factor at a nominal distance of $z_0 = 40$ cm and pixel pitch we find that the particle image displacement is 35 pixels.

Finally, the illumination system used was the Quantronix *Darwin-Duo* Nd-YLF laser with a 2 x 25 mJ pulse energy at 1 kHz and a wavelength of $\lambda = 527$ nm.

5.2.4. Generic Cyclist Model (GCM) and bike

The development of the generic cyclist model is explained by Vloemans, 2022. The model is the average representation of a group of professional riders. The GCM was produced with Fused Deposition Modeling (FDM) 3D printing made from black PLA. Parts of the model were left hollow to save weight. The model's surface was painted using matt black PUTOP fill primer to fill in any gaps between the printed layers. Any excess primer was sanded down to grit 800 to ensure a smooth surface quality. The mat black PUTOP was chosen to minimize any reflections created by the laser light which could decrease the data quality.

The bike used during the experiment was a Scott Plasma 5 (rim brakes) time trial bike. The groupset and wheels were from Shimano from the DURA-ACE line with electronic Di2 shifters. The shoes were Shimano's s-phyre RC902 EU size 44 using yellow cleats from Shimano. Finally, the helmet was the Kask Mistral size medium combined with a detachable visor. An overview of the GCM in TT position in its baseline configuration is shown in Figure 5.9 in which reference distances have been included. The corresponding distances and crank angle can be found in Table 5.3.

Figure 5.9: Baseline configuration of GCM in TT position

The frontal area of the GCM in the wind tunnel setup is estimated to be 0.35 m^2, which is based on the CAD model of the GCM. The CAD models of the helmet and bike were not available and alternatives from the CAD models of the CFD simulation were used instead. During the experiment, a part of the physical cyclist model and bike were scanned resulting in a 3D digital model. Compared to the digital models of the helmet and bike used for the numerical simulations any differences were found to be small and should therefore not affect the estimation of the frontal area.

Table 5.3: Reference distances and angle of the GCM in the wind tunnel setup

Name	Symbol	Dimension	Unit
Crank angle	θ	75	[°]
Hands to ground	A	99	[cm]
Height elbow supports	B	11	[cm]
Lower pedal to ground	C	15	[cm]
Saddle height	D	16	[cm]

The drag reduction methods have been tested with and without the visor to evaluate the effect of having the visor installed. This visor is installed using magnets on the Kask helmet. An overview of both

configurations can be found in Figure 5.10.

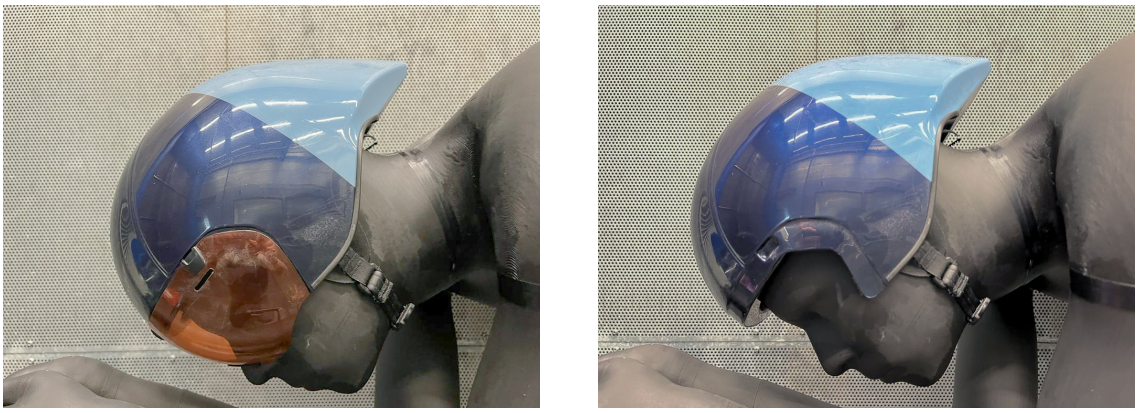

(a) Helmet with the visor installed

(b) Helmet without the visor installed

Figure 5.10: Overview of the Kask Mistral helmet with and without the visor installed

On the cyclist model, a number of markers were added which were used to map the particle tracks onto a global reference frame. In total, seven markers were used as reference points to map the particle tracks onto the global reference frame. The mapping process is explained in more detail in subsection 5.4.4. Markers were added on the hands and back of the GCM trying to cover as much of the measurement volume as possible. The marker positions that were accessible from both sides with the CVV system can be found in Figure 5.11. The diameter of these markers is in the range of 0.5-2 mm.

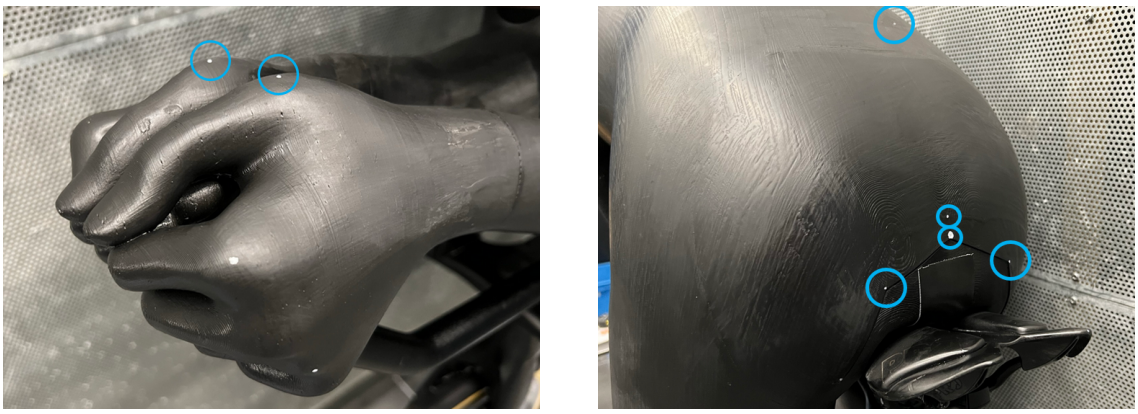

(a) Marker positions on hands

(b) Marker positions on the lower back of the cyclist

Figure 5.11: Markers accessible from both robot positions indicated with circles

5.2.5. Hip Vortex Control (HVC)

The HVC is manufactured using Rapid Prototyping (RP). Given the complex geometry of the GCM it was required to align the HVC with the surface of the GCM to keep flow from moving between the HVC and the GCM. In CAD the contact points of the HVC were modeled as a negative of the surface of the GCM such that it would directly follow the surface of the GCM.

Using a FDM 3D printer the HVC was printed with a 20% infill density to save weight without comprising rigidity. Moreover, the layer thickness was set to 0.4 mm to reduce print times. PLA was chosen as a material because of its low density.

Three versions of the HVC were produced. Each is positioned at a slightly different streamwise location on the model. This would allow for an investigation of the sensitivity of the position of the HVC. Fur-

thermore, the horizontal component of the HVC was kept similar in length in the streamwise direction between the three different positions along the spine of the cyclist. An overview of the three positions of the HVC on the GCM is provided in Figure 5.12. The dimensions of the HVC and its streamwise location with respect to the hands of the GCM can be found in Appendix B.

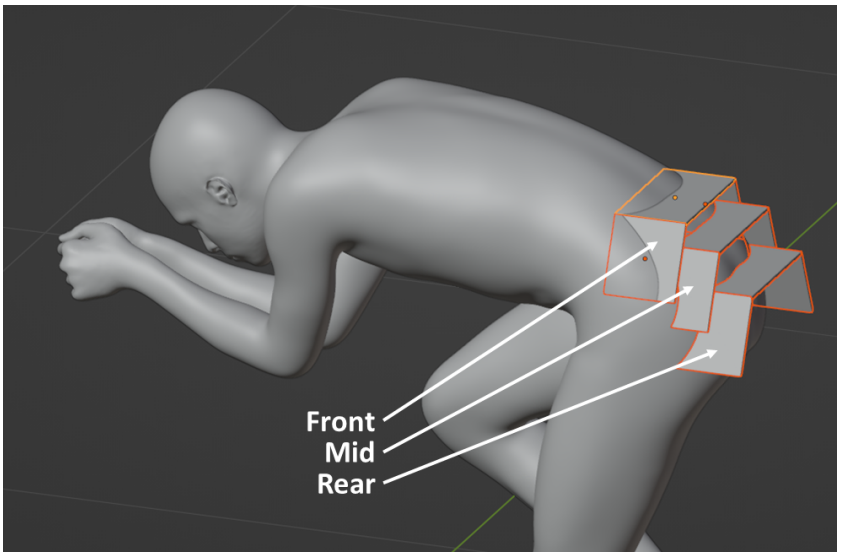

Figure 5.12: Overview of HVC positions tested in the wind tunnel. Although the three HVC positions are shown together in this figure to visualize their relative positions, each was run separately in the wind tunnel experiment

The surface quality of the HVC was considered smooth when taken from the printer directly. Therefore, it did not require any additional post-processing. However, the surface was primed and painted matt black to minimize any laser reflections. Finally, the HVC was fitted to the HVC using black tape sealing any gaps between the GCM and the HVC. An example of the mid-positioned HVC can be found Figure 5.13.

Figure 5.13: Example of the HVC-mid positioned on the GCM

5.2.6. Wingsuit

The production of the wingsuit was done similarly to the production of the HVC. The parts connected directly to the GCM were printed from PLA using a FDM printer. Furthermore, as the print volume was limited in size, it was decided to split the wingsuit into three parts, print these individually, and glue them together. Part of the wingsuit not in direct contact with the GCM was constructed from a 4 mm thick MDF wooden sheet to minimize the amount of printing that was required. The combination of parts of the 3D printed pieces with the wooden construction can be found in Figure 5.14.

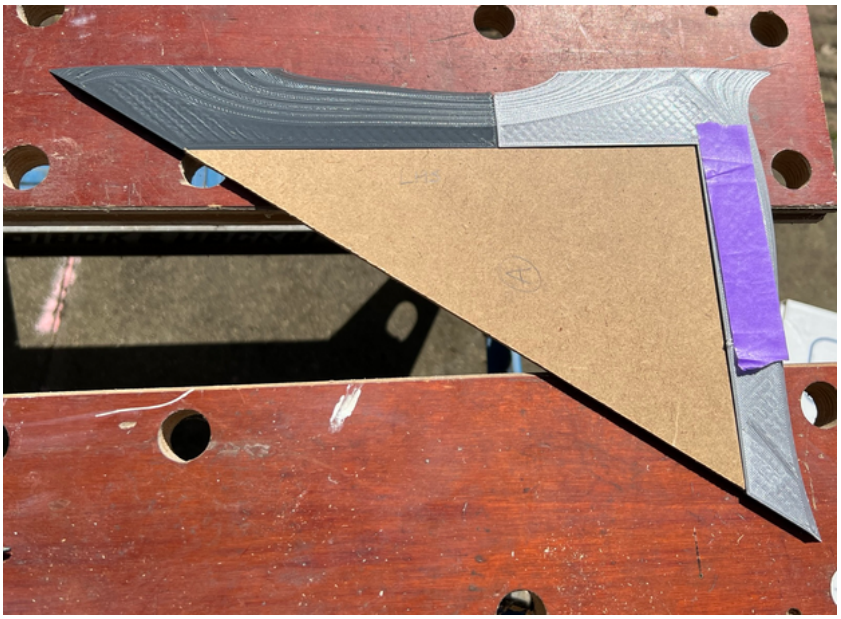

Figure 5.14: Combining 3D printed parts of the wingsuit with 4 mm MDF wooden sheet

Three sizes of the wingsuit were produced to capture the sensitivity in drag. An overview of the three sizes that were tested can be found in Figure 5.15. Both the small and mid wingsuit sizes were scaled-down versions of the large wingsuit. The scaling was done at a corner of the wingsuit positioned in the shoulder of the GCM, making sure that equal scaling was applied to both perpendicular edges of the wingsuit. The scaling parameters were 0.85 and 0.7 for the mid and small wingsuits respectively. The dimensions of each wingsuit size have been added to Appendix B.

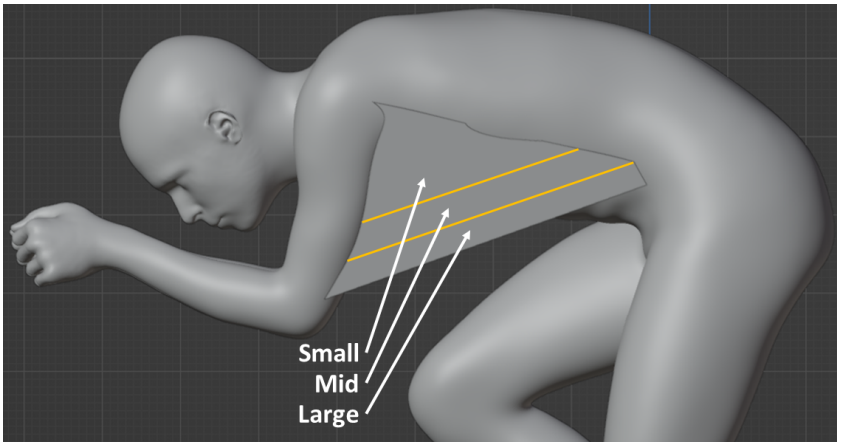

Figure 5.15: Overview of the different wingsuit sizes that were tested in the windtunnel

The wingsuit was primed and painted matt black to reduce any reflections from the laser. The wingsuit was fitted with black tape to the model to minimize any flow escaping between the wingsuit and the GCM. An example of the final wingsuit model fitted to the GCM can be found in Figure 5.16a.

Finally, a mid-sized wingsuit was fabricated from lycra and tested in the wind tunnel. Lycra is a very elastic fabric and is therefore used in the production of cycling clothes. The lycra wingsuit was tested to investigate the aerodynamic effectiveness of a more realistic integration of the wingsuit. A similar-sized lycra cloth was put under tension between the upper arms and upper torso attached using double-sided tape and the edges were covered with black tape to ensure a smooth transition between the model and the wingsuit. An example of the lycra wingsuit installed on the GCM model can be found in Figure 5.16b.

(a) Wingsuit mid installed on the GCM

(b) Wingsuit mid made from lycra to replicate the solid wingsuit in fabric

Figure 5.16: Overview of the wingsuits made from PLA and lycra installed on the GCM

5.3. Data acquisition and procedures

Several procedures were followed to capture information on the flow field. Next, we will discuss each of these procedures used to capture the data with the balance and CVV system.

5.3.1. Balance data acquisition and processing

For the balance measurements, data was measured at a 2 kHz rate for a duration of 30 seconds. For each measurement, a time-average result was computed from which a wind-off condition (zero measurement) was subtracted. Furthermore, measurements without the model and bike installed were taken which were subtracted from the time-average results to account for the drag of struts.

Measurements were repeated for a range of set-point velocities being $0-11-14-15-17-20$ m/s. The set-point velocities showed a small discrepancy with the measured freestream velocity. However, the results were normalized using the measured wind tunnel velocity and air density instead of using the set-point velocity. The measured freestream velocity ranges between 10.3 m/s and 18.3 m/s resulting in a Re ranging between 4.1e5 and 7.3e5 based on the torso length of 0.6 m.

5.3.2. CVV data acquisition and processing

Operation of the CVV camera and image acquisition was done in *DaVis 10.0*, which is a commercial software package distributed by *LaVision*. Furthermore, all the processing of the images was done in *DaVis 10.2*. An overview of the acquisition process of the CVV system is as follows:

1. System installation
   (a) Geometric calibration
   (b) Self-calibration
   (c) Pre-programming of probe positions
2. Data acquisition

(a) Seeding generation
(b) Data acquisition

3. Data processing

(a) Pre-processing
(b) Particle tracking
(c) Data mapping and stitching
(d) Binning
(e) Flow field analysis

A schematic representation of these steps can be found in Figure 5.17.

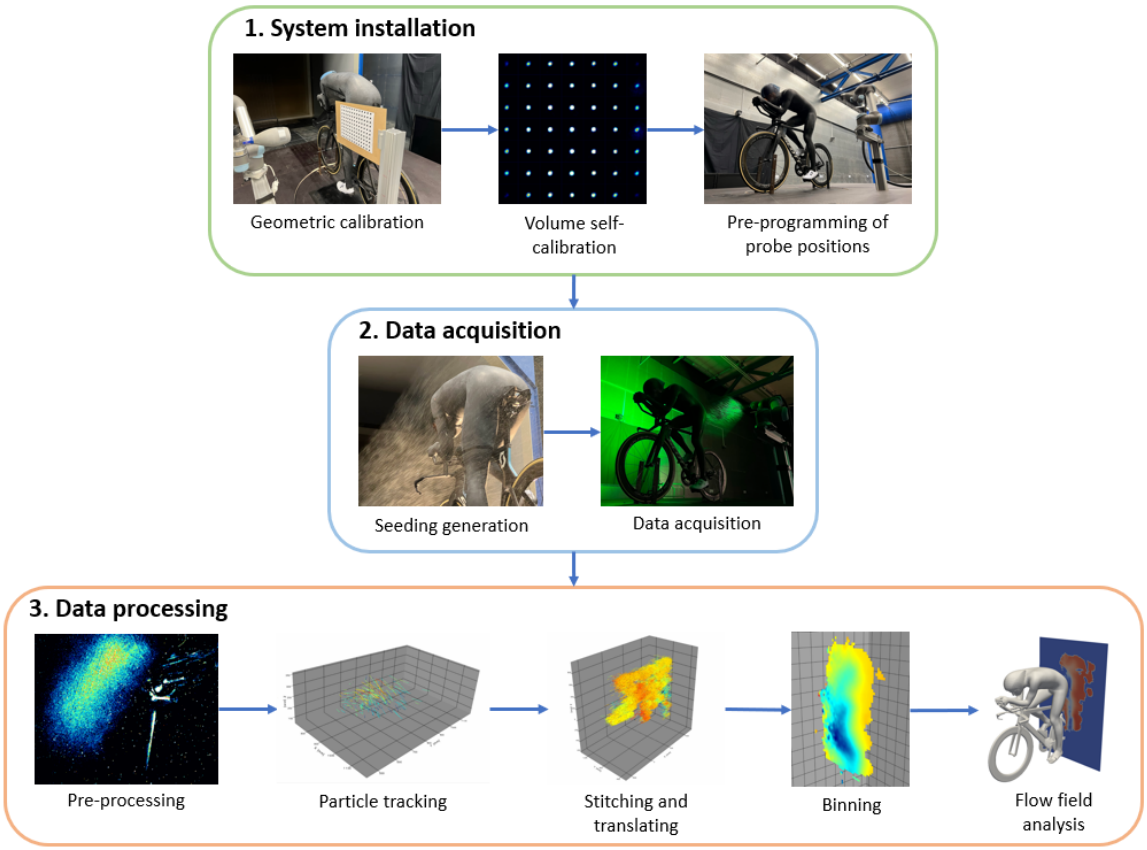

Figure 5.17: Schematic of the CVV processes

Next, each of these steps will be discussed in more detail.

5.3.3. System calibration

Before the data can be processed, two calibration procedures were performed, which are a geometric calibration and volume self-calibration. After the system was calibrated it was not required to re-calibrate after the robot head was re-positioned. This made the system very versatile and quick to use. However, when the system was shut off completely or the position of the robot base was changed, a re-calibration was required. Next, we will discuss both calibration procedures.

Geometric calibration

The first calibration step is called the geometric calibration. The system was calibrated using a calibration plate made in *DaVis*. The calibration plate was printed on A3 paper and placed on a wooden frame

that could be fitted to an x95 beam allowing it to be placed easily in the measurement domain.

A series of images of the calibration plate were captured at 5 different probe locations. These images were captured under ambient light conditions. The camera positions were chosen such that the cameras would capture the calibration plate from different angles while trying to keep the calibration plate filling the field of view. In *DaVis*, a pin-hole calibration (Soloff et al., 1997) was performed on the set of images.

Volume self-calibration

The next step was to perform a volume self-calibration (Wieneke, 2008). To run the volume self-calibration a measurement of the seeded flow was required. Moreover, the seeding density should not be too large for the calibration process to run successfully. Hence, a data set captured in the wake of the cyclist was used to perform the self-calibration.

Through self-calibration, the maximum error in the disparity map of the geometric calibration was reduced. The maximum disparity after the volume self-calibration was 0.19 pixels.

Finally, an Optical Transfer Function (Schanz et al., 2013) was computed. As is explained by Jux, 2017 this is used to re-project the particles from 3D space to 2D image coordinates.

5.3.4. Acquisition

Before the data was acquired, each of the probe positions was pre-programmed in *RoboDK* as was discussed before. The sequence of the probe measurements was programmed such that the robot movements and therefore acquisition times were kept to a minimum. Before a probe location was stored, the robot was positioned such that the probe was pointed approximately with a 45° angle facing upstream and $40 - 50$ cm away from the model to reduce interference with the flow field caused by the camera head.

5.4. Data analysis and reduction techniques

The data analysis and reduction techniques are discussed next. First, the repeatability of the balance measurements is explained. Furthermore, to visualize the flow topology with the data of the 3D-PTV measurements, this must be processed to obtain the 3D velocity field from the particle images. These processes are discussed next.

5.4.1. Repeatability of balance measurements

Part of the balance measurements were repeated throughout the experiment to examine the repeatability of the results and to quantify the variation of the balance measurements over time. An example of repeated measurements of the baseline configuration without the visor installed is shown in Figure 5.18.

From these results, we find that the drag area shifts resulting in slightly larger values as the experiment progressed. Furthermore, the maximum difference between the two measurements was found to be about a 1.2% difference in drag area.

To reduce the uncertainty introduced by this shift in the results it was decided to take two actions into consideration. First, it was decided to only compare the results taken during a single measurement session. Hence, the results shown in the same graph in the next chapter have all been measured where the model was not removed or changed in between measurements. This could be one of the reasons for the shift in the drag area between different measurement days.

Second, it was found that when comparing the deltas in drag area between similar configurations for

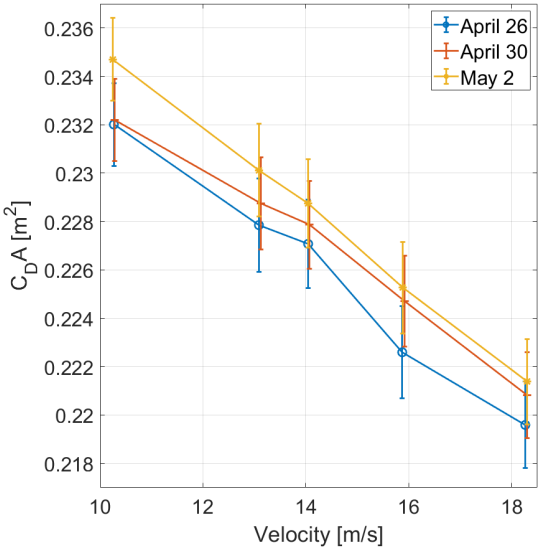

Figure 5.18: Comparison of the measured drag area of the baseline configuration for different sessions

different days the discrepancy between these was small enough that it would not affect any of the conclusions. Hence, trends between different configurations were found to be close when comparing the drag deltas of different measurement days. Therefore, the discussed variation in the measured drag area is not expected to influence the discussion on the results.

5.4.2. Pre-processing of 3D-PTV results

The raw images acquired with the CVV system may contain unwanted reflections in case particles close to the model had been captured. Reflections were minimized by positioning the camera such that it would not be positioned perpendicular to the surface of the model. Nonetheless, some acquisitions still showed reflections in the raw images and needed therefore to be processed before the tracks could be computed.

Each measurement has been categorized into either a nominal reading, where the noise levels are low, or a noise-affected reading. For each category, a different pre-processing technique has been applied. In total 213 cones were processed of which 67 measurements are considered as nominal readings and 146 measurements were processed as noise-affected readings. For this experiment, more noise-affected recordings have been captured because many of the measurements were taken close to the surface of the model to capture the development of the flow structures.

Nominal measurements

The nominal images were pre-processed with a sliding time filter where the minimums were subtracted from the solution. The filter length was set to 7 images. It was found that background noise could be reduced by subtracting the minimum from the raw images.

Noise affected measurements

The images that were affected by static noise were processed slightly differently. Instead of subtracting the minimum, the average solution was subtracted. Using a sliding filter with a filter length of 7 images, the average solution was subtracted from each image reducing the background noise.

This approach assumes, however, that the model, and therefore the noise-affected area, was not mov-

ing during the experiment. Any movement would result in a small variation of the by-reflection affected area and would cause the filter to become less effective. Although some movement of the model was visible during the experiment it was found that these were small enough and that with the filter applied reflections were minimised.

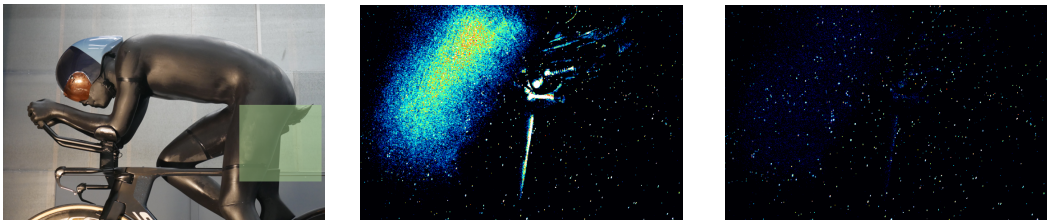

(a) Field of view (in green) **(b)** Raw image **(c)** Pre-processed image

Figure 5.19: Comparison between raw and processed images, with image intensity in the range 0-72 in blue and red respectively, where the average sliding time filter has been subtracted to minimize the noise in the image

An example of a noise-affected image can be found in Figure 5.19b. This image was taken close to the upper part of the extended leg. The result after the sliding filter has been applied is shown in Figure 5.19c. The result shows that the reflections in the image have been reduced considerably and that the particles are still visible.

5.4.3. Shake-The-Box

The next step is to run the Shake-The-Box algorithm in *DaVis* to compute the tracks from the pre-processed images. The working principles are explained by Schanz et al., 2016. Settings were tuned to limit the number of unphysical tracks. Between the two sets of pre-processed images, only the particle detection threshold was varied. For the nominal and noise-affected images, the threshold was set to 15 and 20 counts respectively. The pre-processed images which were affected by noise were found to produce slightly more background noise. Hence, the threshold was raised to keep the number of unphysical tracks to a minimum.

For the remaining settings, it was decided to keep these to the baseline settings as recommended by *DaVis*. However, the minimum track length was increased to 5 particles to improve the quality of the tracks. Furthermore, the maximum absolute change in particle shift had been increased to 3 voxels to account for the larger velocity gradients in the wake of the cyclist. These settings have been based on the analysis of Jux, 2017.

5.4.4. Mapping of particle tracks onto the global frame of reference and repositioning of the CAD model in the data set

Since measurements were taken on both sides of the GCM to capture the asymmetry of the wake, the robot base had to be re-positioned to the other side of the GCM. Hence, the particle tracks found on both sides were combined into a single coordinate system through a homogeneous transformation matrix, which defines a rotation and translation. A rotation component was added to the transformation to account for any small discrepancies in the orientation of the robot base between both sides.

To compute the homogenous transformation matrix (HTM), use was made of a set of seven markers positioned on the surface of the GCM which were accessible from both sides by the CVV camera. The position of these markers was discussed in subsection 5.2.4. Images of these markers were captured, allowing their position to be reconstructed in *DaVis*.

The position of the markers was reconstructed by running an Iterative Particle Reconstruction (IPR) algorithm (Wieneke, 2013) resulting in their position in each of the coordinate systems. With the positions of all 7 markers, an optimization problem was defined to compute the HTM. The definition of the optimization problem can be found in Equation 5.2.

$$\arg \min_{\phi\theta\psi xyz} f := \sum_{i=1}^{N} ||\mathbf{R}(\phi,\theta,\psi)\mathbf{p}_i + \mathbf{T}(x,y,z) - \mathbf{r}_i||^2 \tag{5.2}$$

Here, **R** is the rotation matrix which is defined as $\mathbf{R} = \mathbf{R}_z(\psi)\mathbf{R}_y(\theta)\mathbf{R}_x(\phi)$ (Equation 5.3a) in radians. Moreover, **T** (Equation 5.3b) is the translation vector given in mm. Furthermore, $\mathbf{p}_i$ are the input coordinates and $\mathbf{r}_i$ are the target coordinates.

$$\mathbf{R} = \begin{bmatrix} \cos\psi & -\sin\psi & 0 \\ \sin\psi & \cos\psi & 0 \\ 0 & 0 & 1 \end{bmatrix} \begin{bmatrix} \cos\theta & 0 & \sin\theta \\ 0 & 1 & 0 \\ -\sin\theta & 0 & \cos\theta \end{bmatrix} \begin{bmatrix} 1 & 0 & 0 \\ 0 & \cos\phi & -\sin\phi \\ 0 & \sin\phi & \cos\phi \end{bmatrix} \tag{5.3a}$$

$$\mathbf{T} = \begin{bmatrix} x \\ y \\ z \end{bmatrix} \tag{5.3b}$$

The optimization problem was solved with Horn's quaternion-based algorithm (Horn, 1987). The resulting rotation matrix [rad] and translation vector [mm] can be found in Equation 5.4a and Equation 5.4b respectively.

$$\mathbf{R} = \begin{bmatrix} 0.9958 & 0.0583 & -0.0706 \\ -0.0547 & 0.9971 & 0.0520 \\ 0.0734 & -0.0480 & 0.9961 \end{bmatrix} \tag{5.4a}$$

$$\mathbf{T} = \begin{bmatrix} 112 \\ 1784 \\ -25 \end{bmatrix} \tag{5.4b}$$

The resulting HTM, for which the error between the input and target was minimized, was applied to the input markers which were then translated to the LHS coordinate system. The maximum, mean, and root-mean-square (RMS) error of the magnitude of each of the vectors can be found in Table 5.4.

Table 5.4: Errors between the result and target marker positions

Error	Result [mm]
Maximum	19.8
Mean	6.8
RMS	9.4

An example of the shifted markers can be found in Figure 5.20. The result from this analysis was used to rotate and translate the set of tracks positioned on the RHS onto the LHS coordinate system. These operations were applied after the tracks had been found with the Shake-The-Box algorithm.

Finally, the positions of the markers have also been used to re-position the CAD model of the GCM in the processed solution. This makes it easier to identify the relative position of the flow structures with the model.

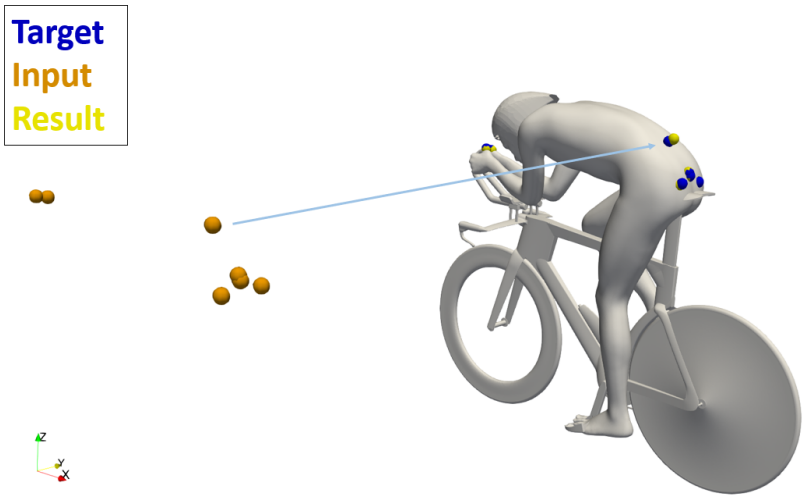

Figure 5.20: Shift of coordinate system after optimization of HTM

5.4.5. Statistical convergence, binning and outlier detection

The bin size was determined based on a convergence study. For each bin, the velocity statistics are ensemble-averaged (Agüera et al., 2016) and were computed in *DaVis*. For two bin sizes, 20 mm and 30 mm, the convergence was investigated. For both bin sizes, the overlap was set to 75% resulting in a 5.0 mm and 7.5 mm vector spacing respectively. Furthermore, it was decided to not investigate any bin size smaller than 20 mm because of the maximum observed error of 19 mm in the mapping of the markers as discussed in subsection 5.4.4.

For this analysis, it was decided to determine the convergence at two locations. One in the wake of the extended leg and one just outside of the wake of the extended leg. These two positions and the time-average solution of the freestream velocity can be found in Figure 5.21.

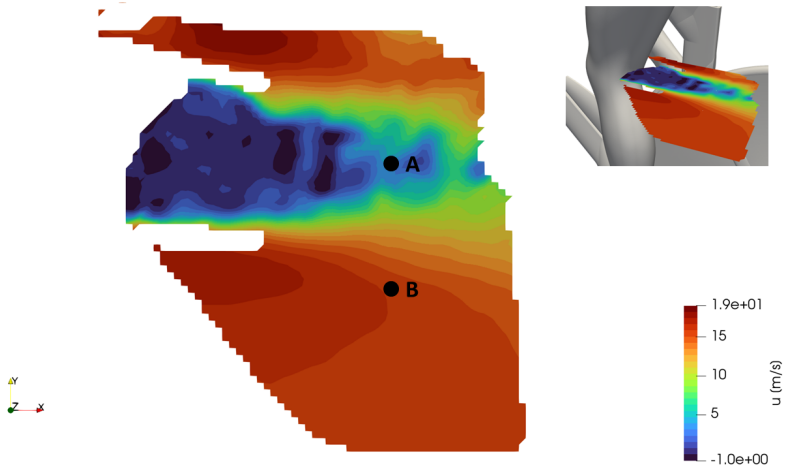

Figure 5.21: Probe locations A (Wake) and B (outside of the wake) where convergence was determined. The figure shows the time-average solution of streamwise velocity based on 10,000 images

In steps of 1000 images, the number of accumulated samples within each bin was computed and plotted. This result can be found in Figure 5.22.

This result shows that the smaller bin size of 20 mm has fewer samples in the bin compared to the larger bin size of 30 mm. However, the result indicates that even in the wake of the extended leg at probe location A, 100 samples are found for the 20 mm bin size. This is considered a minimum to perform a statistical analysis. An example of the total number of particles in the discussed plane can be found in

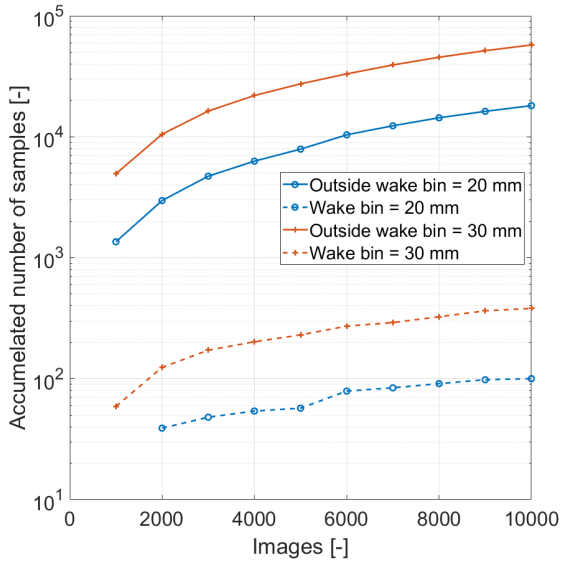

Figure 5.22: Accumelated number of samples contributing to the average velocity

Figure 5.23. This figure indicates that probe location A is positioned in a region with a low number of particles and is therefore representable for one of the more challenging measurement locations.

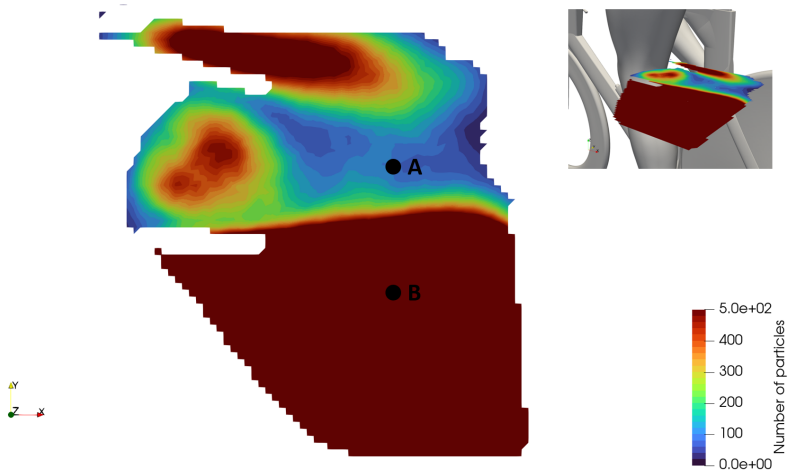

Figure 5.23: Accumulated number of particles per bin for 10,000 images

However, this result does not guarantee that a similar number of particles are found elsewhere in the wake. Nonetheless, this analysis is based on the result of one CVV measurement and it is expected that the number of samples will increase for regions in the wake where two measurements overlap. Furthermore, the position of this plane in the wake of the extended leg is expected to have a relatively small number of particles because of the larger wake size and relatively low velocity. Hence, it is expected to represent a more challenging region to measure convergence.

Additionally, the statistical convergence for all three velocity components was determined at both probe locations. The result for u, v and w can be found in Figure 5.24a, Figure 5.24b and Figure 5.24c respectively.

The result shows that the convergence of the velocity is slightly faster for the larger bin size. Nonetheless, with 10,000 images for each measurement, the smaller bin size also shows that the velocity components still manage to converge. However, for w it can be seen that the velocity in the wake is not completely converged. The unsteadiness of the flow in the wake of the extended leg is expected

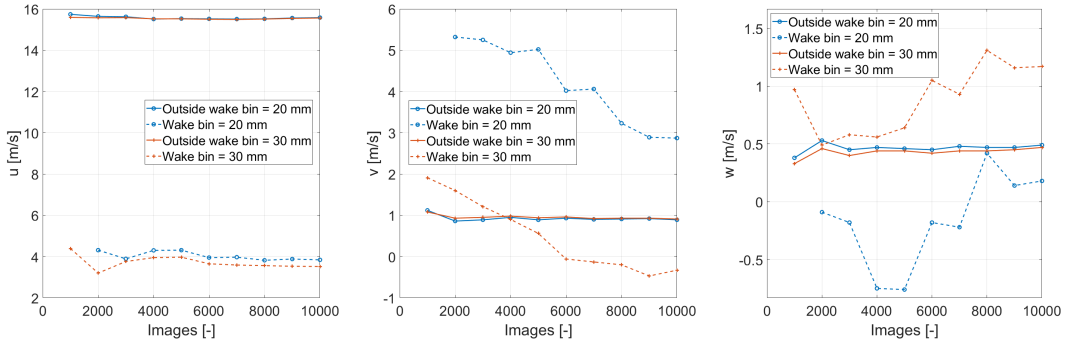

(a) Convergence of u **(b)** Convergence of v **(c)** Convergence of w

Figure 5.24: Convergence of the velocity components in the wake (B) and laminar region (A)

to reduce the convergence rate. However, compared to the magnitude of u it is expected that this variation in w is not affecting the result too much. Finally, because of the velocity gradients in the wake, the results indicate that for different bin sizes, the results converge to slightly different values.

Based on these results it was decided to use a bin size of 20 mm with a 75% overlap. An outlier detection was applied to the solution to reduce the influence of any unexpected velocity measurements. A method named Iterative Reweighted Least Squares (Burrus et al., 1994), was used to determine the outliers, and this function was implemented directly in *DaVis*.

5.5. Experimental errors and uncertainty

To provide an indication of the reliability of the measurements, an analysis of the uncertainty is made. Both the uncertainty for the balance measurements and the PTV results were evaluated and are discussed next.

5.5.1. Model blockage and freestream corrections

The model blockage was found to be 4.3% based on the estimated frontal area of the model and the nozzle exit area of the OJF. Furthermore, the frontal area itself and therefore the model blockage would not change for the HVC and wingsuit configurations compared to the baseline. The model blockage is assumed negligible as for this research the relative difference in drag area measured between configurations is of more importance. Because of this reason, no model blockage correction was applied to the results.

Terra et al., 2019 mention a small velocity correction for the Open Jet Facility of $1.01U_\infty$ for a similar experiment on a full-scale cyclist model. That correction factor was computed following Mercker and Wiedemann, 1996. For this experiment, however, it was decided to not apply this correction factor to the freestream as for the same reason no correction factor for the model blockage was applied. Any conclusions based on the balance measurements were found not to be affected by this decision.

5.5.2. Uncertainty of the balance measurements

The 6-component balance has a documented maximum uncertainty (ϵ_F) of the drag force (F_X) of $\epsilon_F = 0.06\%$. The maximum allowed drag force for this balance ($F_{X_{max}}$) was 250 N (Alons, 2008).

The standard measurement uncertainty of the mean force was computed for the force measurements taken at 2 kHz for 30 seconds assuming that the observed drag values are normally distributed. The uncertainty was computed using Equation 5.5.

$$\epsilon_F = \frac{k\sigma}{\sqrt{N}} \tag{5.5}$$

Here, k is the coverage factor (in this case k=1 as the standard measurement uncertainty is computed), and N is the number of uncorrelated samples. The standard deviation (σ) of the raw data for the drag force was computed for the baseline configuration and the result can be found in Table 5.5.

Table 5.5: Force statistics of drag force measurements for the baseline configuration

Freestream velocity [m/s]	Mean drag force [N]	Standard deviation [N]	Uncertainty [N]	Percentage of mean [%]
0	0.0	0.049	-	-
10.3	16.3	1.734	0.11	0.7
13.1	26.1	3.181	0.20	0.8
14.0	29.8	3.435	0.22	0.8
15.9	37.8	4.656	0.29	0.8
18.3	49.3	5.685	0.36	0.7

In finding the number of uncorrelated samples an autocorrelation function of the force signal of F_X was computed at $U_\infty = 14$ m/s. The result can be found in Figure 5.25. Assuming an uncorrelated signal at the second positive peak at t$= 0.12$ s resulted in 30 s / 0.12 s = 250 uncorrelated samples per measurement.

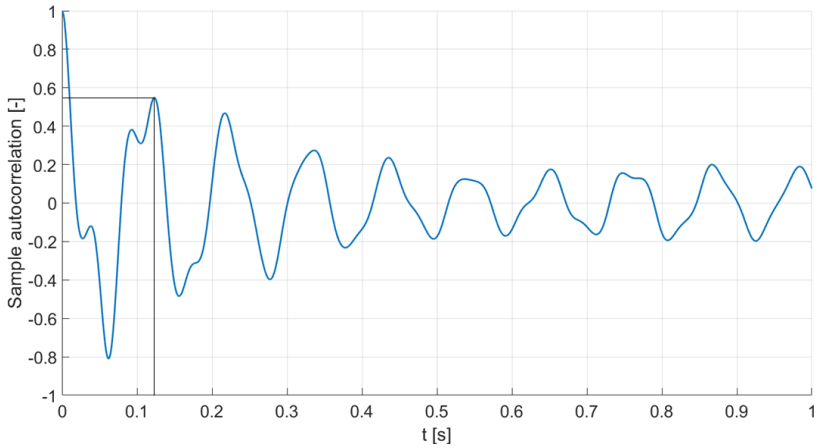

Figure 5.25: Autocorrelation function for F_x at $U_\infty = 14$ m/s with lines indicating the time at which the signal is considered uncorrelated

The resulting autocorrelation functions of the force responses for the other freestream velocities were found to result in a similar number of uncorrelated samples. Hence, it was decided to use the 250 uncorrelated samples per measurement in the computation of the uncertainty for all freestream velocities.

As can be seen from Table 5.5, the uncertainty as a percentage of the mean is similar for each freestream velocity. Compared to the documented uncertainty of the balance this is found to be larger and is therefore considered as the uncertainty for the balance measurements.

The standard deviation of the raw signal was computed for various measurements taken during the experiment and was found to be consistent throughout. However, for the computation of the measurement uncertainty the largest observed standard deviations were used and are shown in Table 5.5. Furthermore, each of these uncertainties has been added to the balance results in the next chapter with uncertainty bars.

5.5.3. Interference CVV system

Although PIV is accepted as a non-intrusive measurement technique the use of a CVV robotic system will affect the flow since the camera is always near the measurement region. However, both Jux, 2017 and Giaquinta, 2018 mention that it is expected that the presence of the CVV system is negligible on the measured flow field.

Giaquinta, 2018 discusses the analysis of a freestream measurement. According to Giaquinta, 2018 a minimum distance of 32 cm is recommended to keep the maximum measured velocity error below 1%. However, this analysis is based on a previous version of the camera head. For this research, a more streamlined-shaped housing was used as was shown in Figure 3.8. For the measurements taken in this experiment, the recommended minimal distance was taken into consideration but the actual error was expected to be smaller because of the updated geometry of the housing of the camera system.

5.5.4. Uncertainty of the CVV measurements

The uncertainty of the velocity field of the 3D-PTV measurements is investigated at both probe locations as is shown in Figure 5.21. Equation 5.5 was used to compute the standard measurement uncertainty of the velocity components. The standard deviation (σ) of each velocity component was computed based on the contribution of all tracks in the bins at the probe locations shown in Figure 5.21.

Jux, 2017 discusses the uncertainty at a similar position in the wake of the extended leg of a cyclist. Jux, 2017 mentions that a characteristic frequency of 50 Hz in the wake of the extended leg is expected. This frequency is used to compute the number of uncorrelated samples. With the image sampling rate of 821 Hz a total of 609 uncorrelated samples for each measurement of 10,000 images were computed. Hence, following Equation 5.5, the uncertainty scales with $1/\sqrt{609} = 0.04$.

To estimate the expected uncertainty, the results from the wake measurements shown in Figure 5.21 have been used. However, as was discussed, for probe location A only 100 samples were measured. However, for the 100 samples found in this bin in the wake, it is expected that these are randomly distributed during the acquisition and hence are uncorrelated.

Hence, it was decided to compute the uncertainty for each velocity component at probe location A assuming that the 100 samples are uncorrelated. The result can be found in Table 5.6. This result is considered to represent the worst case of uncertainty as the sample size is relatively low and the flow is highly unsteady. Additionally, to compute the uncertainty in the region outside the wake (B) it was decided to use the computed number of uncorrelated images of 609. Those results can also be found in Table 5.6.

Table 5.6: Uncertainty for the velocity components measured in the wake and laminar region for the time average solution with 10,000 images

Velocity component (probe location A)	Velocity [m/s]	σ_u [m/s]	Uncertainty [m/s]
u	3.84	2.92	0.29
v	2.87	6.24	0.62
w	0.18	3.38	0.34

Velocity component (probe location B)	Velocity [m/s]	σ_u [m/s]	Uncertainty [m/s]
u	15.58	1.60	0.065
v	0.89	1.66	0.067
w	0.49	1.31	0.053

This uncertainty does, however, not take into account some additional sources of uncertainty such as the repositioning of the CVV probe. Furthermore, as more time passes between measurements, after relocating the probe, the level of uncertainty is expected to increase. Small variations in ambient conditions may contribute to this. To provide a more complete evaluation of the uncertainty for the CVV measurements another approach is considered.

Individual CVV measurements taken next to each other were programmed such that part of the volume would overlap. Within these overlapping regions on a predefined grid, the mean velocity for each of the individually processed measurements was computed. By taking the root-mean-square (RMS) of the difference between the velocity components on the same grid, another indication of the uncertainty is presented as the measured velocity at those locations should be identical. The velocity on this grid was determined using a linear interpolation between the measured velocity vectors. For two regions, shown in Figure 5.26, the uncertainty was evaluated.

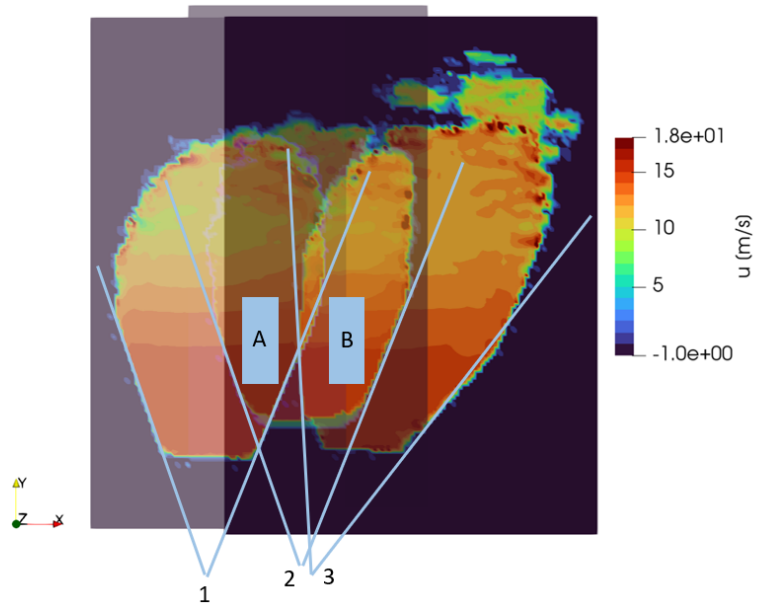

Figure 5.26: Overview of overlap regions between separate CVV measurements. The uncertainty was determined for regions A (for probe positions 1 and 2) and B (for probe positions 2 and 3)

Since the orientation of the CVV probe for position 3 was slightly angled around the z-axis it was decided to compare this against the observed uncertainty for positions 1 and 2 between which the probe was only translated. As was discussed before, the in-depth uncertainty of the CVV system is about 10 times larger than the uncertainty in the other two directions. Hence, this is expected to affect the uncertainty when rotating the CVV probe. The results are shown in Table 5.7.

Table 5.7: Computed RMS of the difference between two measurements in regions A and B

Velocity component	Uncertainty A [m/s]	Uncertainty B [m/s]
u	0.17	0.18
v	0.11	0.16
w	0.17	0.13

The results show that the uncertainty in region B for the u and v components is indeed slightly larger than the uncertainty measured in region A. As was discussed, the rotation of the CVV probe between positions 2 and 3 could contribute to this. Compared to the uncertainties shown in Table 5.6 it can be seen that for the results outside of the wake, these uncertainties are larger. The uncertainty of 0.18 m/s is expected to better represent the uncertainty than the previously discussed uncertainties for the outside wake as it also takes into consideration the repositioning of the CVV probe.

Ultimately, these presented uncertainties for the CVV measurements are not expected to be of concern in the evaluation of the results. In the comparison of the flow fields between different configurations, the focus is on the identification of large variations in the flow field. Hence, smaller variations that fall within the uncertainty range are not regarded and are therefore expected not to influence the conclusions.

6

Results and Discussion

The following chapter discusses the results of both the CFD investigation and the wind tunnel tests. The CFD simulations were used in the early stages of the project to gain insights into the workings of the proposed drag reduction methods. Based on these results, physical models were designed and tested in the wind tunnel. First, a discussion of the numerical results is provided, focusing on the working mechanisms resulting in the drag reductions. Then, the experimental results are discussed to verify the drag reductions and flow mechanisms examined in the numerical results.

6.1. Numerical results

The numerical results for each of the three configurations, the baseline, the HVC, and the wingsuit, as explained in chapter 4, are discussed next. The development of the HVC and the wingsuit was done numerically. The changing flow topology for each configuration is discussed highlighting the working mechanism.

6.1.1. Baseline results

The presence of large vortex structures in the wake of a cyclist and its relation to drag is discussed in section 2.4. To expand on this discussion it is therefore critical to understand the baseline 3D flow topology. An overview of the flow field is provided first, before comparing this to the results of the other configurations.

The flow topology of the baseline configuration shows a variety of flow structures. Part of these are counter-rotating vortex pairs emanating at the upper arms and hips. The presence of these structures is in line with the results of Crouch et al., 2014 and Jux et al., 2018. Moreover, the correlation of the flow topology with the experiment of Jux et al., 2018 has been discussed in chapter 4. Figure 6.1 shows an overview of the flow topology of the baseline configuration in which labels have been included highlighting the elbow and hip vortices. The flow topology has been visualized with the Q-criterion and is colored by vorticity.

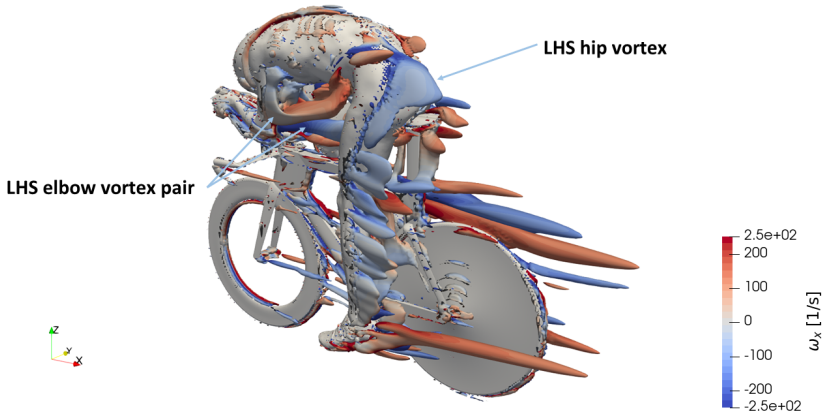

(a) LHS view

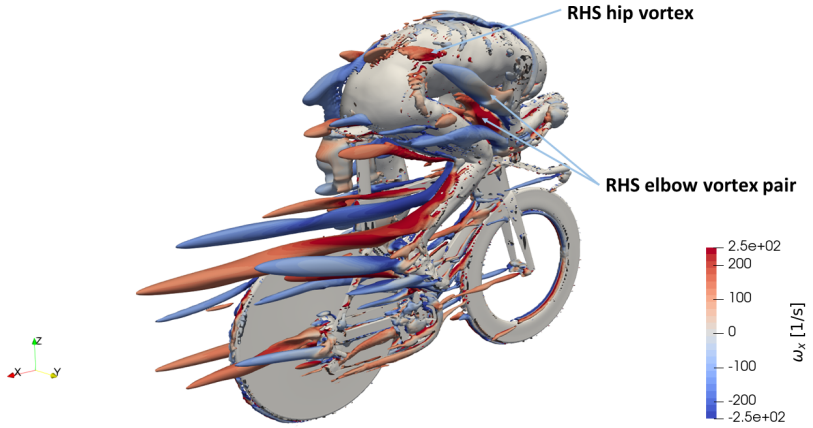

(b) RHS view

Figure 6.1: Baseline CFD result showing Q-criterion ($Q = 4000\ [1/s^2]$) coloured by ω_x [1/s] (red counterclockwise and blue clockwise vorticity)

These results show a large asymmetry in the size and position of the hip vortices as is expected for the high-drag position. Additionally, the outboard vortex from each vortex pair, located at the upper arms, was found to progress downstream along the side of the lower back. A difference between the LHS and RHS is that the RHS outboard elbow vortex is positioned slightly higher which is attributed to the presence of the raised upper leg.

6.1.2. HVC results and manipulation of the hip vortices

The flow topology for the HVC configuration is discussed next. The objective of the HVC is to reduce the streamwise vortices by promoting separation on the lower back. The flow topology is visualized by Q-criterion and colored by vorticity. The result is shown in Figure 6.2. Furthermore, these figures showing the flow topology have been placed side-by-side with the baseline result in Appendix C for easy comparison.

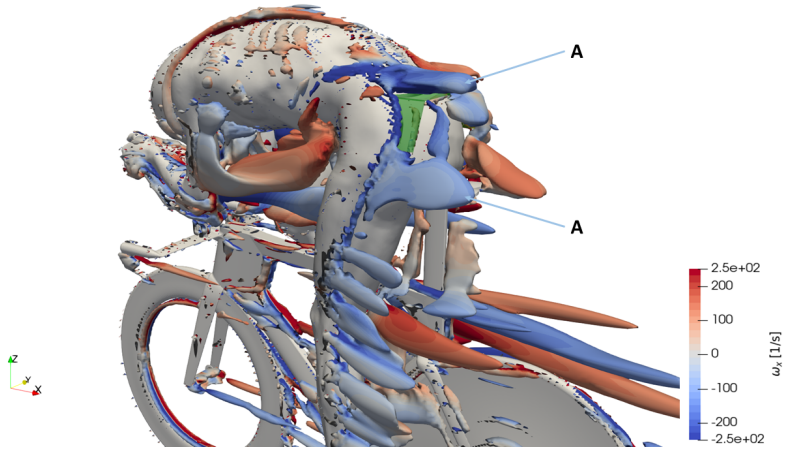

(a) LHS view

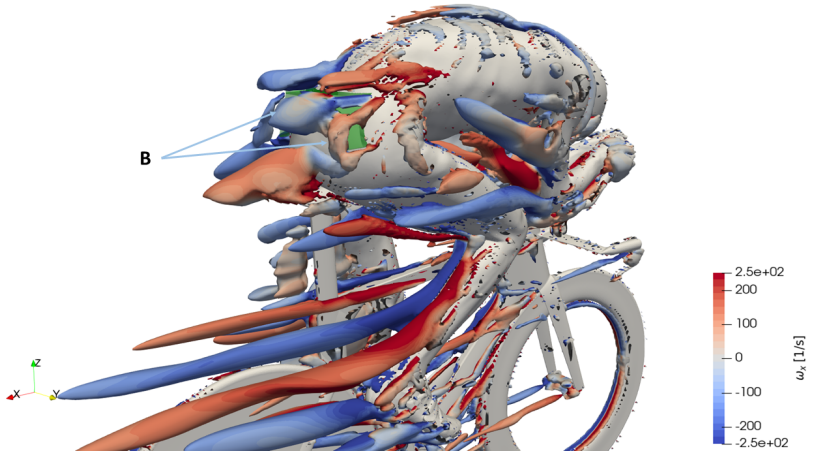

(b) RHS view

Figure 6.2: HVC (in transparent green) CFD result showing Q-criterion ($Q = 4000\ [1/s^2]$) coloured by ω_x [1/s] (red counterclockwise and blue clockwise vorticity)

A few key differences compared with the baseline configuration stand out. First of all, Figure 6.2a indicates that the LHS hip vortex (A) has reduced in size when compared to the baseline result shown in Figure 6.1a. Second of all, around the trailing edges of the HVC, smaller structures have developed (B). Interestingly, with the HVC installed, the symmetry of the hip vortices has become more comparable to the flow topology of the symmetric leg position as discussed by Crouch et al., 2014. As was discussed previously, Crouch et al., 2014 have indicated that the symmetric position of the hip vortices can be related to a drag reduction compared to the asymmetric position of these structures. This suggests that a drag reduction is expected as a result of the change in flow topology. To further develop the analysis, the flow field is examined at planes throughout the computational domain. An overview of the positions of these planes can be found in Figure 6.3.

The flow field at the rear axis in the wake of the cyclist is visualized by the streamwise velocity and streamwise vorticity and is compared against the baseline configuration. This is shown in Figure 6.4. First, by comparing the streamwise velocity, the more symmetric position of hip vortices is also reflected in the wake development as is shown in Figure 6.4b. Another discrepancy is the expansion of the wake behind the extended leg for the HVC configuration. This is expected to increase the drag and therefore limits the effectiveness of the HVC. The comparison of the streamwise vorticity in Figure 6.4 shows that the RHS hip vortex dissipates slightly faster compared to the baseline configuration as its peak strength is reduced highlighted by the absence of the line contour representing $\omega_x = 100$ 1/s.

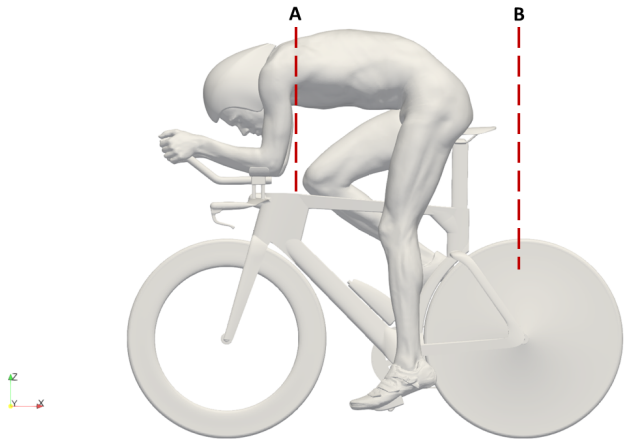

Figure 6.3: Overview of the plane positions used to analyze the numerical results

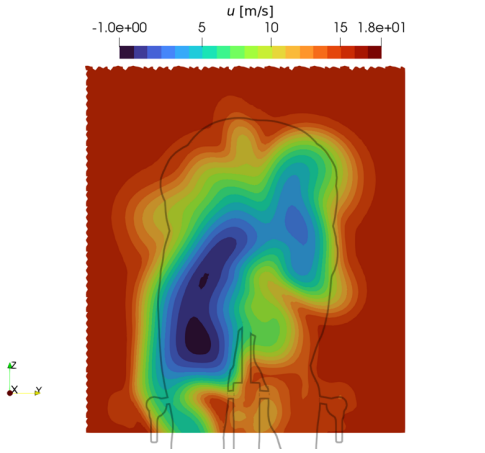

(a) Streamwise velocity of the baseline configuration

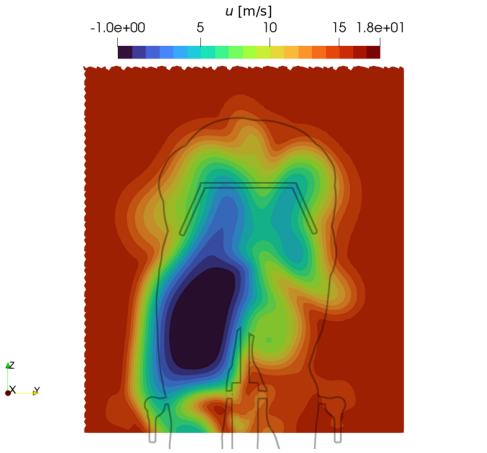

(b) Streamwise velocity of the HVC configuration

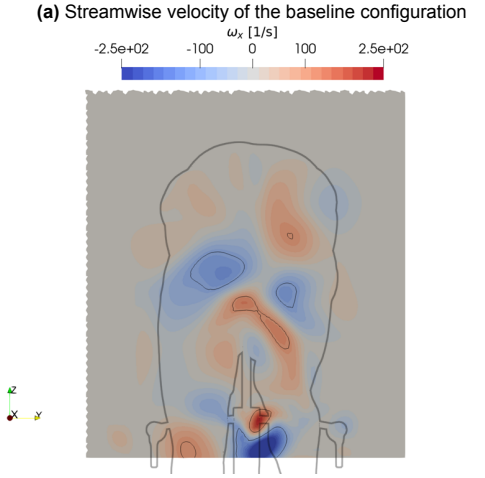

(c) Streamwise vorticity of the baseline configuration and a line contour of $\omega_x = \pm 100$ [1/s]

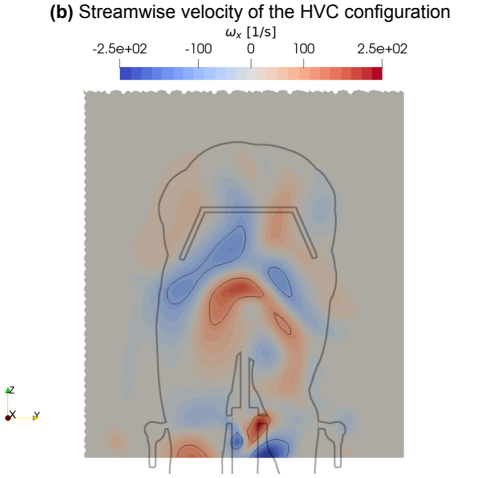

(d) Streamwise vorticity of the HVC configuration and a line contour of $\omega_x = \pm 100$ [1/s]

Figure 6.4: Comparison of the streamwise velocity and vorticity between the baseline (left) and HVC (right) configurations at the location of the rear axis (position B)

The variation in wake topology is also clearly visualized in a plane centered on the location of the wheels as shown in Figure 6.5. With the HVC installed, Figure 6.5b shows that a region of flow reversal has developed on the lower back of the cyclist. This was not observed in the baseline result shown in

Figure 6.5a. When comparing the streamwise vorticity in the same plane, it was found that the hip vorticity dissipates slightly faster compared to the baseline configuration as is made visible with a line contour in Figure 6.5c and Figure 6.5d.

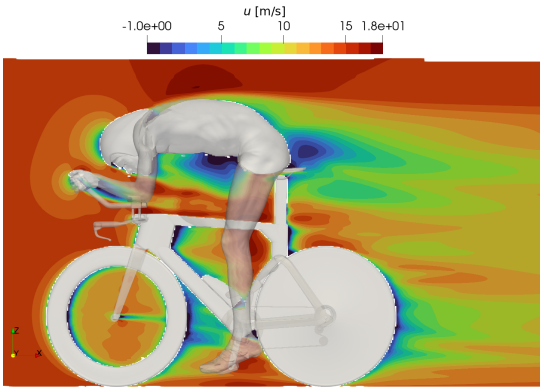

(a) LHS view of the baseline configuration showing streamwise velocity

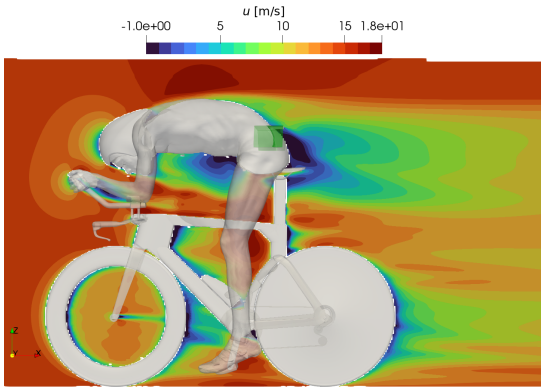

(b) LHS view of the HVC configuration showing streamwise velocity

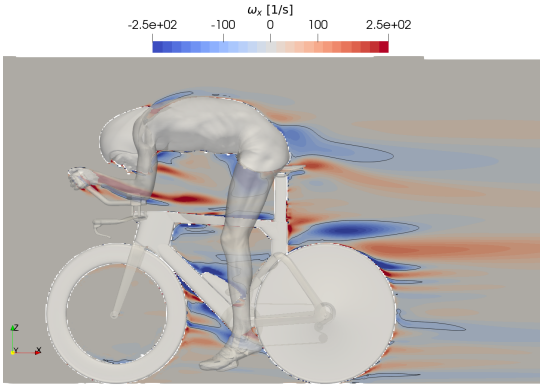

(c) LHS view of the baseline configuration showing streamwise vorticity and a line contour of $\omega_x = -50$ [1/s]

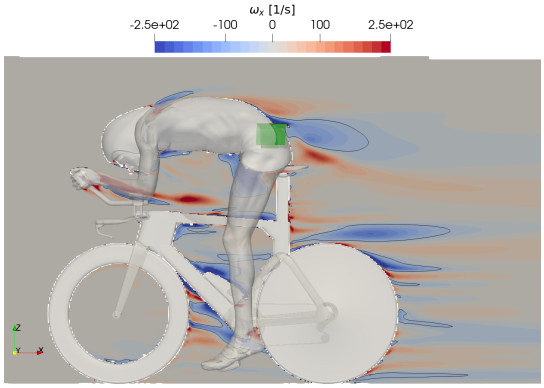

(d) LHS view of the HVC configuration showing streamwise vorticity and a line contour of $\omega_x = -50$ [1/s]

Figure 6.5: Comparison of the streamwise velocity and vorticity between the baseline (left) and HVC (right in transparent green) configuration at a center plane

To understand the effect of these changes in the flow field on the drag, the pressure on the back of the cyclist is visualized. This is shown in Figure 6.6. The result indicates that especially on the LHS, where the hip vorticity has reduced the most, the pressure contours show an increase in surface pressure contributing to a reduction in drag.

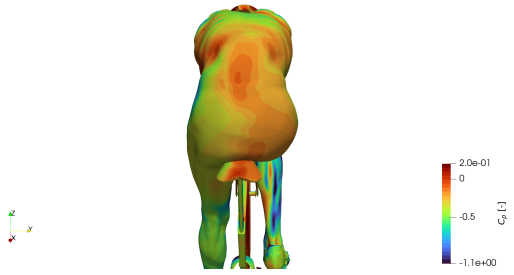

(a) Rear view of the cyclist's back for the baseline configuration

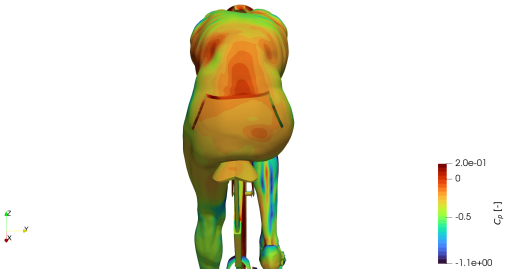

(b) Rear view of the cyclist's back for the HVC configuration

Figure 6.6: Comparison between the baseline configuration (left) and wingsuit configuration (right) showing pressure coefficient on the back of the cyclist

Fundamentally, the HVC increases the wake on the lower back and locally reduces the hip vortex structures in strength. This relation between the counter-rotating vortex pairs in the wake of a bluff body and the surface pressure was discussed in section 2.4. It was concluded that reducing such vortices by promoting separation, can lead to an increase in surface pressure. The numerical results suggest a similar working mechanism as the wake is increased, the streamwise vortices have been reduced and, the surface pressure has increased.

As was discussed in section 2.4, Beaudoin and Aider, 2008 and Aider et al., 2010 demonstrate that the reduction of streamwise vortices by promoting separation on the back of an Ahmed body leads to a reduction in drag. More specifically, Aider et al., 2010 conclude that the longitudinal vortices must be reduced to lower the drag, based on a wake integral analysis. The author continues that the expansion of the wake should also be kept to a minimum to reduce the drag effectively. Figure 6.2 highlights that with the HVC installed, streamwise vortex structures still appear around the hips and thighs, suggesting there is more potential to further reduce the drag. This is expected, however, to require a more complex design of the HVC.

6.1.3. Wingsuit results and manipulation of the elbow vortices

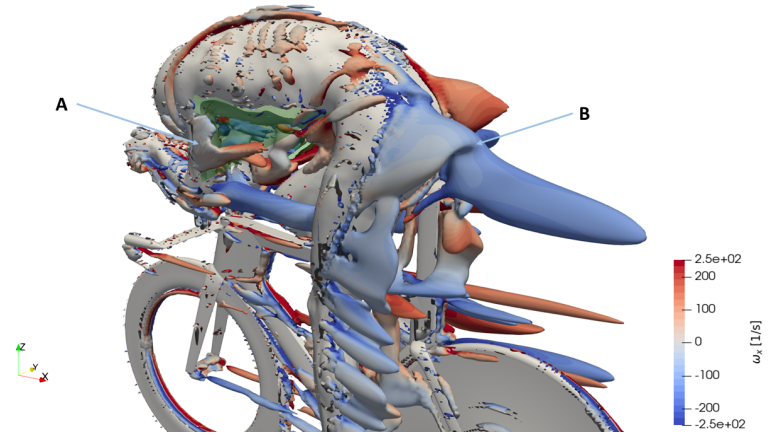

(a) LHS view

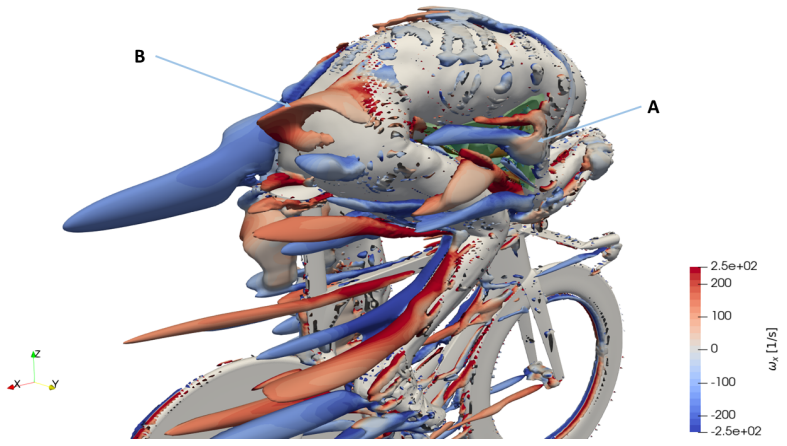

(b) RHS view

Figure 6.7: Wingsuit (in transparent green) CFD result showing Q-criterion ($Q = 4000\ [1/s^2]$) coloured by ω_x [1/s] (red counterclockwise and blue clockwise vorticity)

An overview of the flow field for the wingsuit configuration can be found in Figure 6.7. The wingsuit geometry has been included in transparent green to allow for visual access between the upper arms.

When comparing the result to the baseline flow topology in Figure 6.1 a few differences stand out. The outboard elbow vortex (A), on both the LHS and RHS, is reduced in size. Especially on the LHS, the presence of the elbow vortex is decreased whereas in the baseline result, this vortex extends further downstream towards the side of the lower torso. These figures compared to the baseline configuration, have also been added side-by-side to Appendix C for easier comparison. A second observation is that the size of the hip vortices (B) for both the LHS and RHS is increased. Both vortices extend further into the wake as a result of the introduction of the wingsuit.

Further inspection of the flow field in a plane behind the upper arms shows that the wake on the RHS is slightly increased. This result, visualized by the streamwise velocity for the baseline and wingsuit configurations, is shown Figure 6.8a and Figure 6.8b respectively. Additionally, the vortices emanating from the upper arms have reduced in strength to various degrees. This is visualized for the baseline and wingsuit configurations in Figure 6.8c and Figure 6.8d respectively.

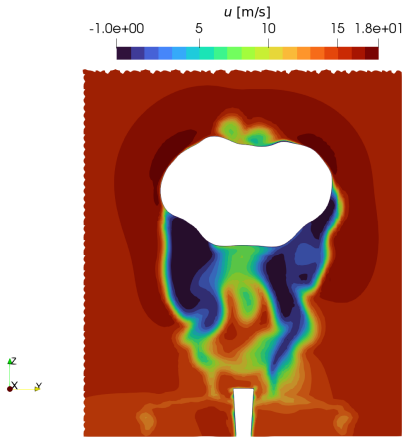

(a) Streamwise velocity of the baseline configuration

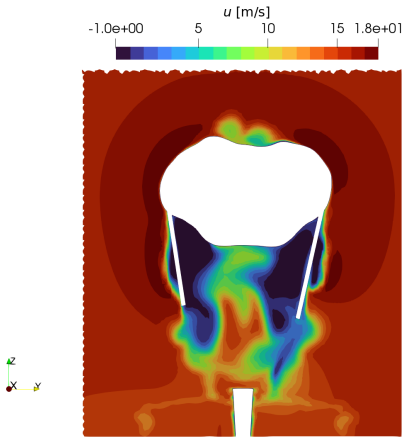

(b) Streamwise velocity of the wingsuit configuration

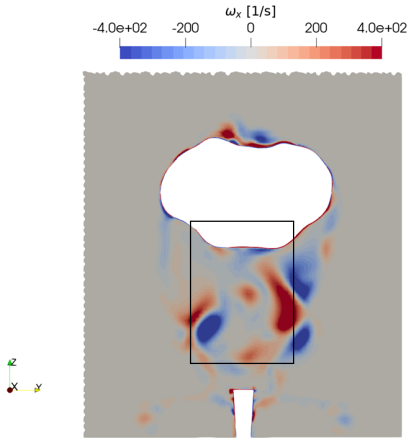

(c) Streamwise vorticity of the baseline configuration showing a rectangle for which the circulation (Γ) was computed

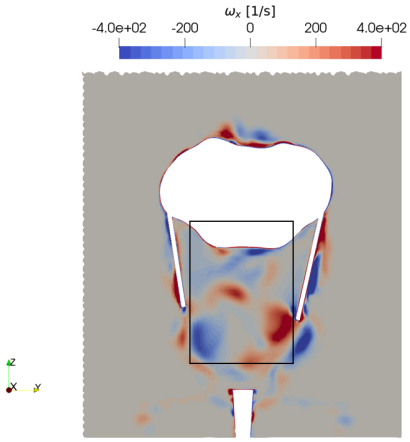

(d) Streamwise vorticity of the wingsuit configuration showing a rectangle for which the circulation (Γ) was computed

Figure 6.8: Rear view of a slice behind the upper arms (position A) comparing the streamwise velocity and vorticity between the baseline (left) and wingsuit (right) configurations

Two vortices positioned towards the inboard side of the elbows are present in both results, however, their strength has reduced. A comparison between the vortex strength is made based on the circulation (Γ) inside the rectangle shown in Figure 6.8c and Figure 6.8d. The circulation was computed using Equation 2.3. The results are shown in Table 6.1.

The table indicates that the total circulation behind the upper arms has reduced for the wingsuit configuration compared to the baseline configuration. This suggests that the vortex strength inside the area

Table 6.1: Circulation behind the upper arms by integrating the absolute streamwise vorticity ($|\omega_x|$) on the surface in the rectangle shown in Figure 6.8c and Figure 6.8d

Configuration	Γ [m^2/s]
Baseline	7.16
Wingsuit	6.20

shown in Figure 6.8d for the wingsuit configuration has decreased. To inspect the effect of this reduction in vorticity on the pressure distribution in the wake, a comparison between both configurations can be found in Figure 6.9. Here, the pressure coefficient is shown in a plane behind the upper arms to which a line contour is added visualizing the streamwise vorticity at $\omega_x = \pm 250$ [1/s].

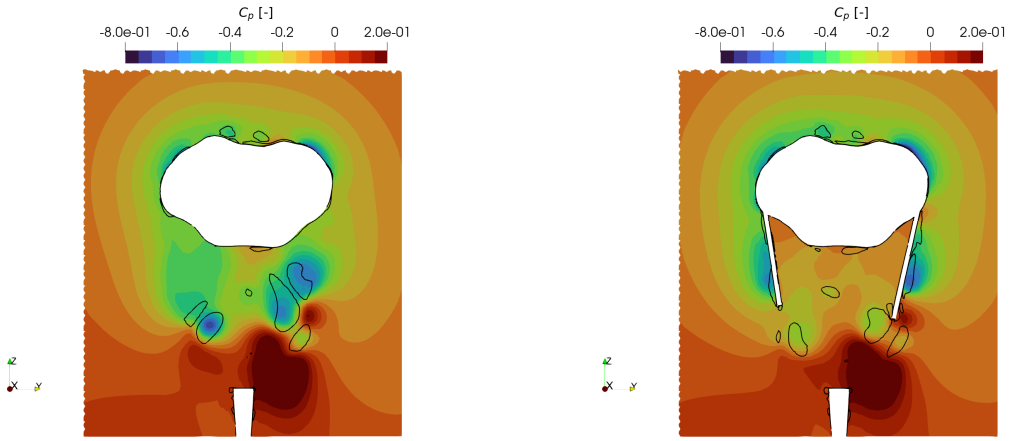

(a) Baseline configuration

(b) Wingsuit configuration

Figure 6.9: Rear view of a slice behind the upper arms (position A) showing C_p [-] and a line contour showing $\omega_x = \pm 250$ [1/s]

Interestingly, the line contours of $\omega_x = \pm 250$ [1/s] and therefore the position of the elbow vorticity immediately highlight the relation between regions of low pressure and the core of the vortices. By reducing the number of vortices emanating from the upper arms the result shows that locally the pressure has increased. Although the pressure in the wake is still indirectly related to the total drag of the cyclist, it does indicate a strong relation between the presence of the streamwise vortices and the local pressure distribution.

Using a wake integral analysis it is, however, possible to estimate the deficit in pressure, streamwise velocity, and, in-plane velocity providing more detail on the cause of the drag reduction. Each term of the wake deficit analysis used by Crouch et al., 2014 shown in Equation 2.5 was evaluated in the rectangle in the plane shown in Figure 6.8c. The results are shown Table 6.2.

Table 6.2: Drag area estimation using the relation of the pressure and momentum deficit shown in Equation 2.5 of the area highlighted in Figure 6.8c

Drag area	Baseline	Wingsuit	Difference
Pressure term [m^2]	-0.0056	-0.0085	-0.0029
Streamwise velocity term [m^2]	0.0398	0.0421	0.0023
In-plane velocity term [m^2]	0.0041	0.0032	-0.0009
Total [m^2]	0.0383	0.0368	-0.0015

The variation in the wake topology between the two configurations and its effect is clearly represented in these results. The absence of the elbow vortices contributes to a reduction of the in-plane velocity responsible for part of the recovery of the wake deficit. However, the majority of the recovery of the wake deficit is a result of the reduction of the pressure deficit. The increase in the wake is also visible from this analysis as the streamwise velocity term has slightly increased for the wingsuit configuration. This example clearly demonstrates the importance of the balance between the streamwise vorticity and wake

size in the development of drag reduction methods as was also discussed in subsection 2.4.1. There, it was mentioned that it is preferred to reduce the streamwise vorticity while keeping the increased wake size to a minimum to effectively reduce the drag.

To better relate the effect of these variations in the flow field with the drag area of the cyclist, the pressure on the surface of the upper arms was examined. This pressure distribution on the upper arms can then be directly related to the pressure drag which is, as discussed before, the main contributor to the total drag. The comparison of the pressure distribution on the upper arms between the baseline and wingsuit configuration can be found in Figure 6.10. The figure shows that with the wingsuit the pressure has increased considerably on the upper arms contributing to the reduction in pressure drag.

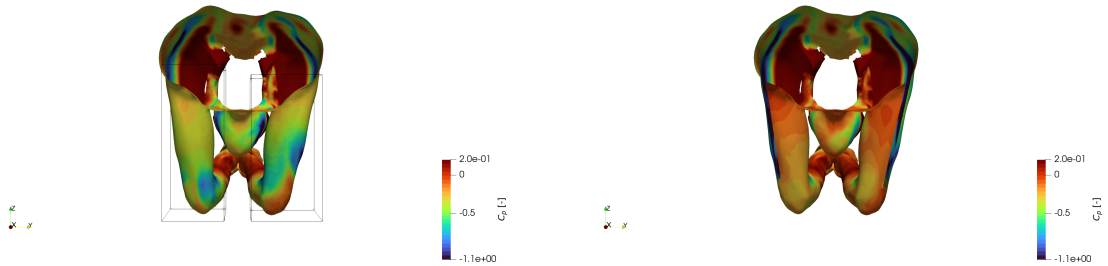

(a) Rear view of the upper arms for the baseline configuration showing an outline of the regions where the drag was computed

(b) Rear view of the upper arms for the wingsuit configuration

Figure 6.10: Comparison between the baseline configuration (left) and wingsuit configuration (right) showing pressure coefficient on the upper arms

After the evaluation of the forces acting on the upper arms positioned in the outlined volume indicated in Figure 6.10a, a reduction of -1.25 N in pressure drag between the baseline and wingsuit configurations was measured. This result is obtained after subtracting the pressure drag acting on the upper arms of the baseline configuration from the wingsuit configuration as shown in Table 6.3. The results in the table indicate that this local change in drag is also responsible for the total change in pressure drag and that the viscous drag has not changed between the two configurations. Despite the difference in pressure drag acting on the upper arms being almost completely responsible for the change in total drag, further downstream other variations in the flow topology are observed. These will be discussed next.

Table 6.3: Drag force computed on the upper arms in the volume shown in Figure 6.10a

Configuration	Pressure drag LHS upper arm [N]	Pressure drag RHS upper arm [N]	Total pressure drag upper arms [N]	Total viscous drag [N]	Total pressure drag [N]	Total drag [N]
Baseline	1.31	1.06	2.37	1.82	19.12	20.94
Wingsuit	0.64	0.48	1.12	1.82	17.86	19.68
Difference (Wingsuit-Baseline)	-0.67	-0.58	-1.25	0	-1.26	-1.26

Downstream effects

Since the wingsuit is positioned so far upstream also a downstream effect can be expected. As was already discussed, the hip vortices have increased in size for the wingsuit configuration compared to the baseline. The variations in the streamwise velocity and streamwise vorticity in a plane at the rear axis for the baseline and wingsuit configurations can be found in Figure 6.11.

These figures show that the upper side of the wake is positioned slightly lower compared to the baseline. The streamwise vorticity shows an increase in the hip vortices' size as previously discussed. These discrepancies will affect the local pressure distribution. The comparison of the pressure distribution on the lower back of the cyclist between the wingsuit configuration and the baseline result can be found in Figure 6.12.

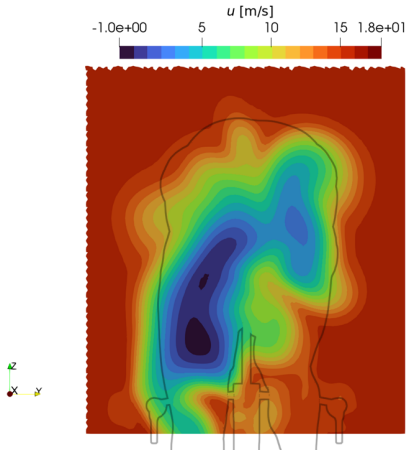

(a) Rear view of the baseline configuration showing streamwise velocity

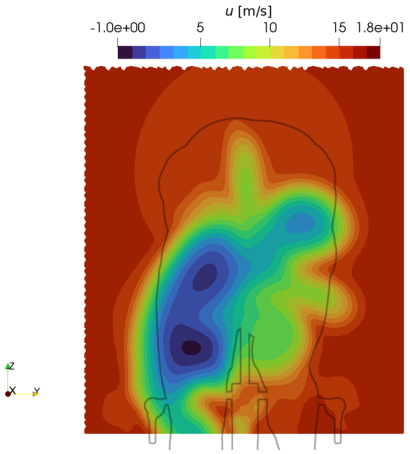

(b) Rear view of the wingsuit configuration showing streamwise velocity

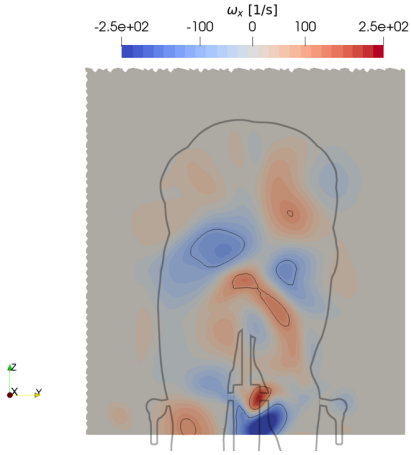

(c) Rear view of the baseline configuration showing streamwise vorticity and a line contour of $\omega_x = \pm 100$ [1/s]

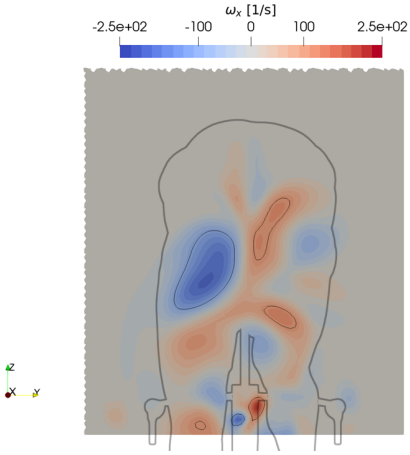

(d) Rear view of the wingsuit configuration showing streamwise vorticity and a line contour of $\omega_x = \pm 100$ [1/s]

Figure 6.11: Comparison of the streamwise velocity and vorticity on a plane at the rear axis (position B) between the baseline (left) and wingsuit (right) configurations

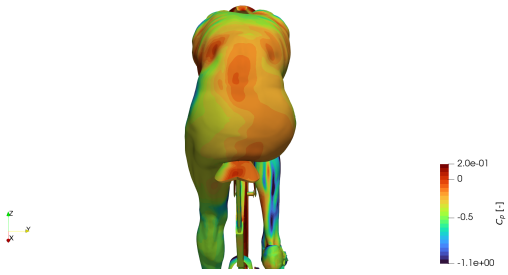

(a) Rear view of the cyclist's back for the baseline configuration

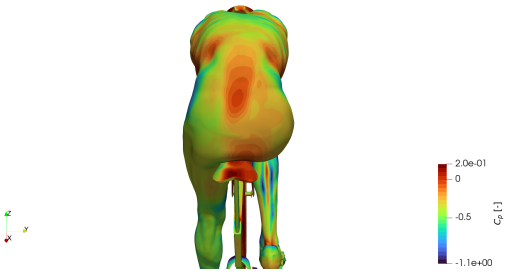

(b) Rear view of the cyclist's back for the wingsuit configuration

Figure 6.12: Comparison between the baseline configuration (left) and wingsuit configuration (right) showing pressure coefficient on the back of the cyclist

Two differences stand out. First of all, the surface pressure along the spine of the cyclist has increased. This is attributed to the stronger hip vortices which increase the local downwash on the upper back of the cyclist. Second of all, the areas on the lower back close to the origin of the hip vortices show a reduction in surface pressure. This will contribute to an increase in drag especially on the lower back where the majority of the wall's normal is pointed in the drag direction. However, it is expected that the drag can be further reduced by manipulating the hip vortices for the wingsuit configuration. This has been measured in the wind tunnel and will be discussed in section 6.2.

6.1.4. Overview of the drag reductions

As a result of the variations in flow topology for the HVC and the wingsuit configurations compared to the baseline, a drag reduction for both was observed. Below, in Table 6.4, an overview is given of the drag areas computed with CFD. The results indicate that the wingsuit is more effective in reducing the drag compared to the HVC resulting in a -5.91% and -2.15% drag area reduction respectively.

Table 6.4: Overview of drag reductions estimated with CFD

Configuration	$C_D A$ [m^2]	$\Delta C_D A$ [%]	Weighted $C_X A$ [m^2]	Weighted $\Delta C_X A$ [%]
Baseline	0.186	0	0.183	0
HVC	0.182	-2.15	0.180	-1.64
Wingsuit	0.175	-5.91	0.173	-5.46

These results clearly indicate that it is feasible to achieve a drag reduction through the manipulation of the flow topology in cycling. This is, therefore, contributing to the objective of this thesis. Nonetheless, to solidify these findings the experimental results will be discussed investigating if these agree with the numerical solutions.

The weighted drag area has also been included in Table 6.4. The definition of the weighted drag area has been discussed in subsection 3.4.1 and is a weighted average of the drag area of the crosswind analysis. As can be seen from Table 6.4, both the HVC and wingsuit were found to become slightly less effective when considering the weighted drag area. More details on the crosswind results will be discussed next.

6.1.5. Crosswind analysis

In CFD, the sensitivity of each configuration with the crosswind angle was evaluated. Table 6.4 shows the weighted drag area for each configuration and Figure 6.13 provides more detailed information on the force coefficient at each crosswind angle. The result for the lateral aerodynamic force has been added to Appendix C and was found to only slightly increase for both the HVC and wingsuit configurations and is therefore not expected to cause any stability problems on the bike.

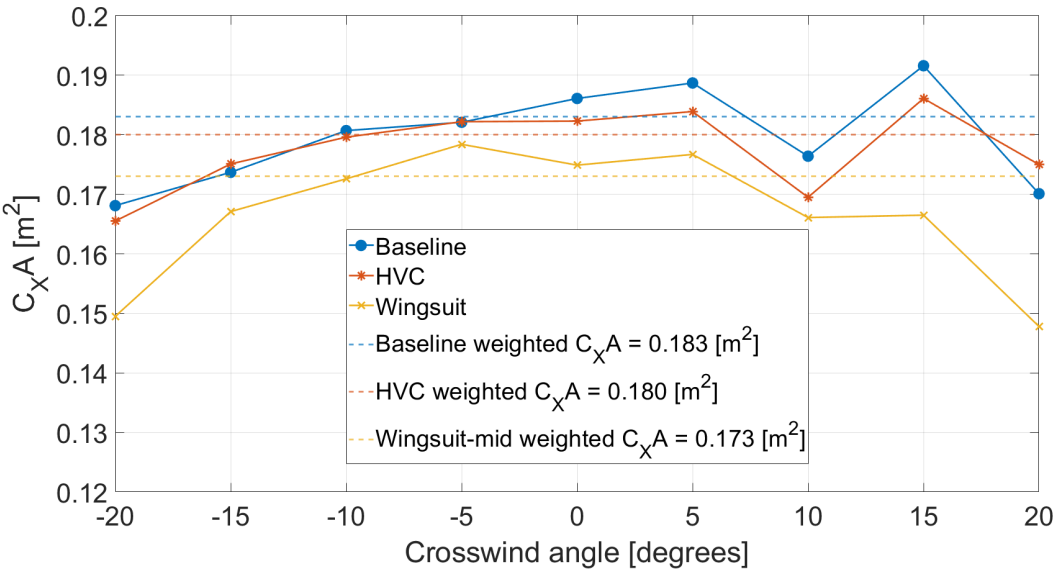

Figure 6.13: Crosswind drag analysis in CFD of the HVC and wingsuit compared with the baseline

The result displayed in Figure 6.13, shows that for the full range of crosswind angles, the drag area for the wingsuit configuration is smaller compared to the baseline configuration. Additionally, the HVC is

more effective for positive crosswind angles compared to the result for negative crosswind angles. The asymmetric response is attributed to the asymmetric leg position.

Although these results are promising regarding the effectiveness of the drag reduction methods, more information is required before any accurate conclusions can be made. As the flow field is expected to be very complex, especially towards the more extreme crosswind angles as the projected frontal area increases, it is expected that the RANS simulations can become less reliable. For these crosswind angles, no experimental results of the 3D flow field were available to verify the physicality of the flow field of the numerical simulations. Hence, to confirm the effectiveness of the drag reduction methods for this range of crosswind angles, the drag force is also measured in the wind tunnel experiment.

Nonetheless, the 3D flow topology at -15° has been added to Appendix C. This should provide an indication of the major discrepancies between the three configurations in such conditions. These results should, however, be verified in the future to be more confident in the physicality of the presented flow structures. Consequently, these results are not discussed in detail.

6.2. Experimental results

The results of the wind tunnel experiment are discussed next. First, an overview of the flow field for each of the three configurations is provided. Differences in the flow topology compared against the baseline are discussed which will lead to the results of the balance measurements. Finally, the results of the crosswind experiments are provided.

6.2.1. The 3D flow topology of the GCM in time trial position

The flow field for the three configurations, the baseline, HVC-mid, and wingsuit-mid, was measured using 3D-PTV. The objective for these measurements is to further develop an understanding of the reasons for the measured drag reductions and verify the observed flow mechanism from the numerical simulations. The setup of the CVV system has been discussed in chapter 5. A few planes are defined to help visualize the flow field of which the positions are shown in Figure 6.14.

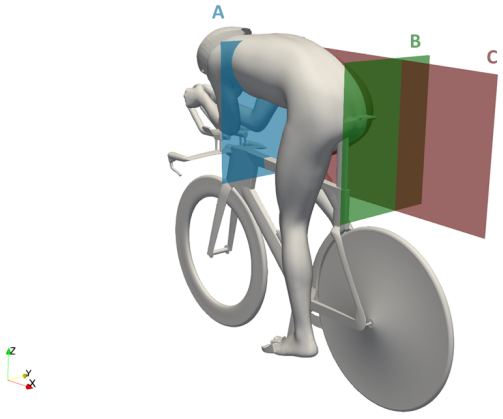

Figure 6.14: Definitions of the planes used to visualize the flow field of the experimental results

An overview of the flow topology for the baseline configuration is shown in Figure 6.15. Here, the flow topology is visualized with the Q-criterion which is colored by the streamwise vorticity.

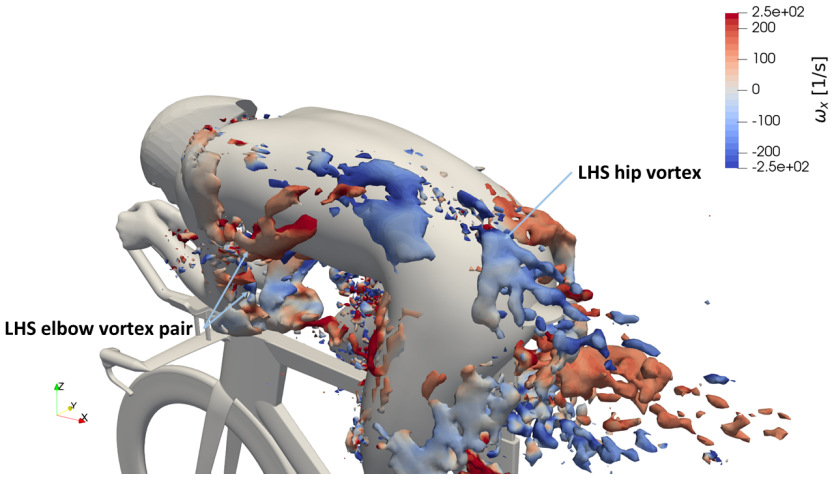

(a) LHS view

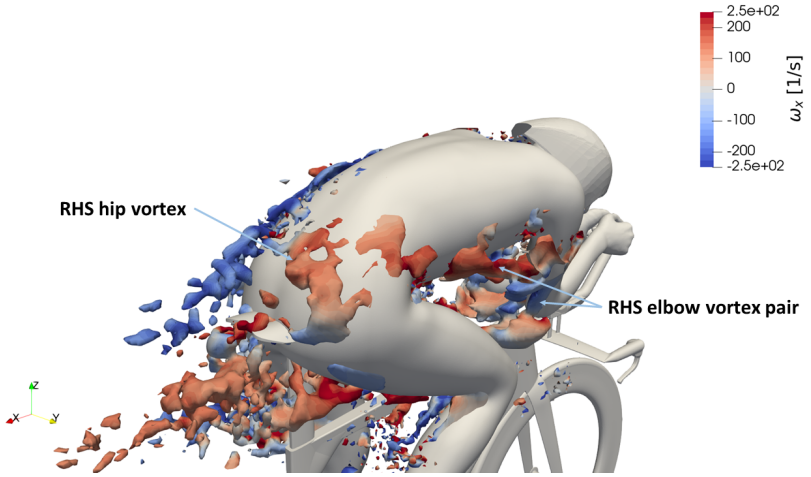

(b) RHS view

Figure 6.15: Baseline experimental result showing Q-criterion ($Q = 4000\ [1/s^2]$) coloured by ω_x [1/s] (red counterclockwise and blue clockwise vorticity)

The results indicate vortices emanating from the upper arms and hips. The most noteworthy flow structures are highlighted. First, the LHS hip vortex is found to continue slightly further downstream compared to the RHS which is similar to the numerical results. Furthermore, the vortices originating from the upper arms are found to follow similar paths downstream as the numerical results suggested. On both sides, these vortices follow the sides of the lower torso towards the lower back of the cyclist.

The displayed flow structures, compared to the numerical results, appear to be less coherent. This is expected to be a result of the bin size. In subsection 5.4.5 an explanation of the decision of the bin size is provided. For the following analysis, the fact that the flow structures appear less coherent is not expected to affect any of the conclusions.

A visualization of the streamwise velocity at the position of the rear axis is examined, which can be found in Figure 6.16. Compared to the results of Jux et al., 2018, it is found that the streamwise velocity in the wake of the cyclist compares well. Small differences include the downwash along the lower back being slightly more tilted and the velocity in the wake of the cyclist reaching lower values compared to what is discussed by Jux et al., 2018. Such discrepancies are assumed to be an effect of the differences between the two models.

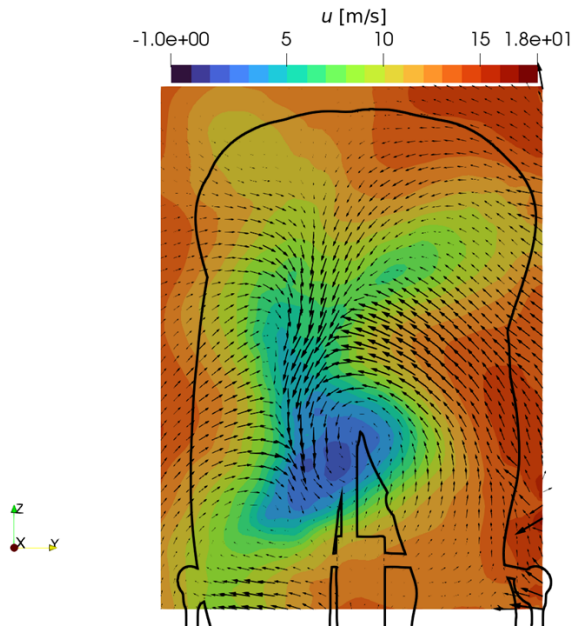

Figure 6.16: Streamwise velocity at the location of the rear axis (position B). The arrows, which are scaled by velocity magnitude, indicate the in-plane velocity

6.2.2. The flow topology of the HVC

The flow field in the wake of the HVC configuration is compared with the baseline results. The flow topology is visualized with the Q-criterion and is colored by the streamwise vorticity. However, only part of the flow field is visualized because data was only captured in a smaller part of the wake because of time and resource limitations. The measurement domain is outlined in Figure 6.17 which also shows the measured flow topology. Similar to the numerical results, the strength of the hip vortex is reduced. However, flow structures still form around the trailing edges of the HVC.

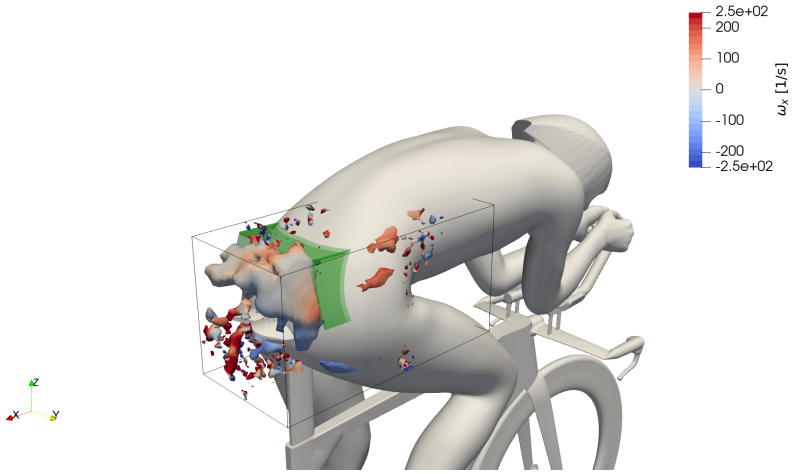

Figure 6.17: HVC experimental result showing Q-criterion ($Q = 4000\ [1/s^2]$) coloured by ω_x [1/s] (red counterclockwise and blue clockwise vorticity)

Next, the streamwise velocity and streamwise vorticity are visualized in a plane at the rear axis. This result can be found in Figure 6.18 where the baseline configuration is compared against the HVC.

The results show a more expanded wake similar to what was predicted by the numerical results. Furthermore, the RHS hip vortex is reduced in size comparable to what was suggested by the numerical

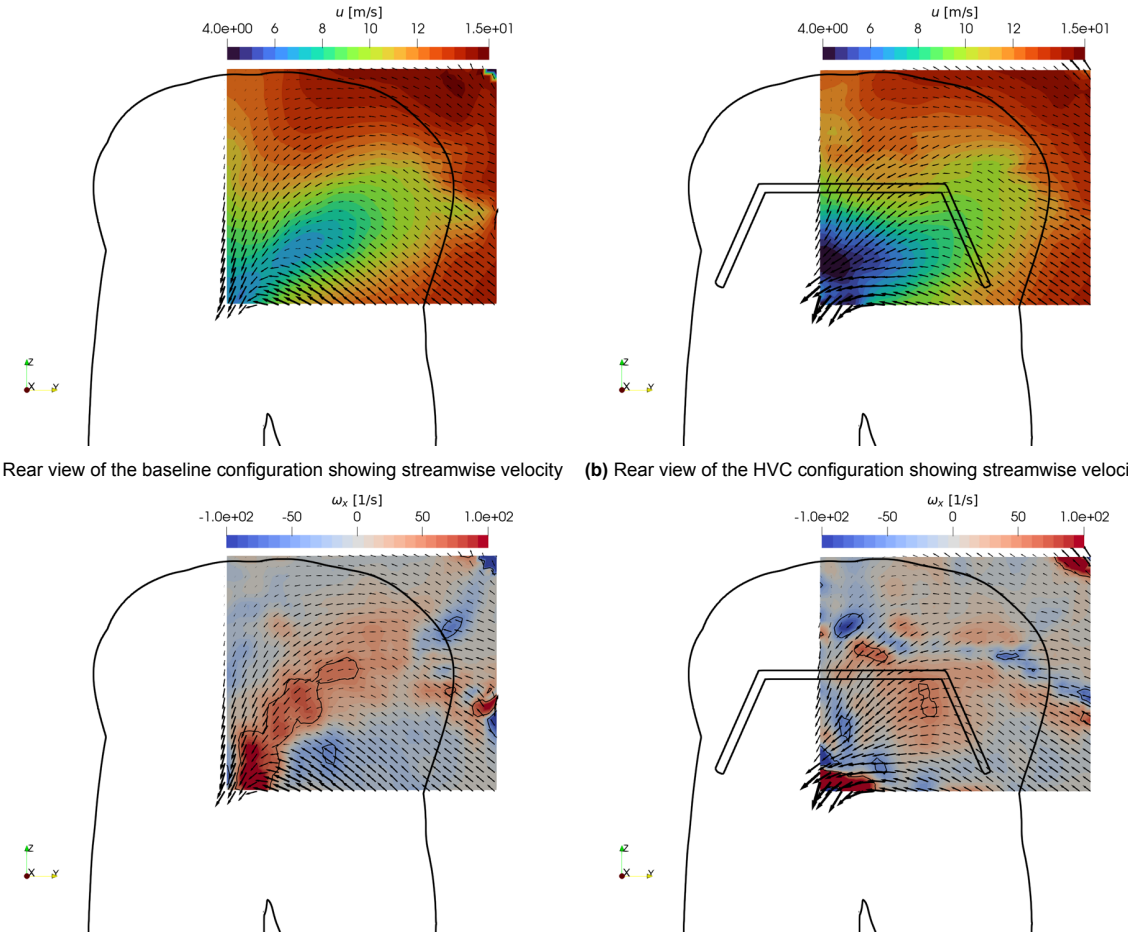

(a) Rear view of the baseline configuration showing streamwise velocity

(b) Rear view of the HVC configuration showing streamwise velocity

(c) Rear view of the baseline configuration showing streamwise vorticity and a line contour of $\omega_x = \pm 50$ [1/s]

(d) Rear view of the HVC configuration showing streamwise vorticity and a line contour of $\omega_x = \pm 50$ [1/s]

Figure 6.18: Comparison of the streamwise velocity and vorticity in a plane at the rear axis (position B) between the baseline (left) and HVC (right) configuration

simulations. The expansion of the wake and reduction of trailing streamwise vortices is in agreement with the flow mechanisms discussed by Beaudoin and Aider, 2008 and Aider et al., 2010.

To further expand on the working mechanism, the flow field in a side view is visualized. These results include the streamwise velocity and streamwise vorticity for the baseline and HVC configurations and are shown in Figure 6.19. These figures show that the wake behind the cyclist is increased as a result of the HVC. In the baseline configuration, the flow remains attached longer as a result of the downwash component created by the counter-rotating hip vortex pair. The wake behind the HVC, however, was found to recover quickly where the discrepancy with the baseline result reduces further downstream.

Figure 6.19c indicates that for the baseline configuration, the RHS hip vortex progresses further downstream compared to the result of the HVC. Furthermore, the size of this vortex is larger compared to the hip vortex found when the HVC is installed. A similar trend was discussed in section 6.1 where the numerical results indicated an increase in wake size and a reduction in hip vorticity for the HVC configuration. The numerical results showed that the decrease in vorticity was found to increase surface pressure and reduce the drag. Based on these experimental results, which indicate similar trends, it is expected that the working mechanism of the HVC is similar between the numerical and experimental results.

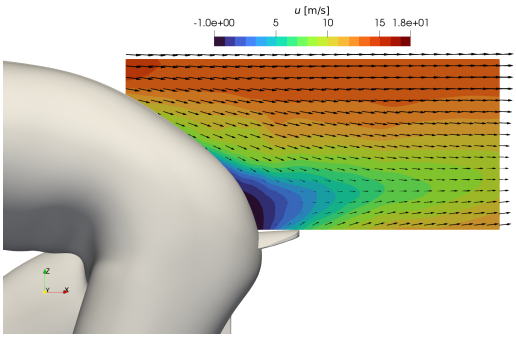

(a) LHS view of the baseline configuration showing streamwise velocity

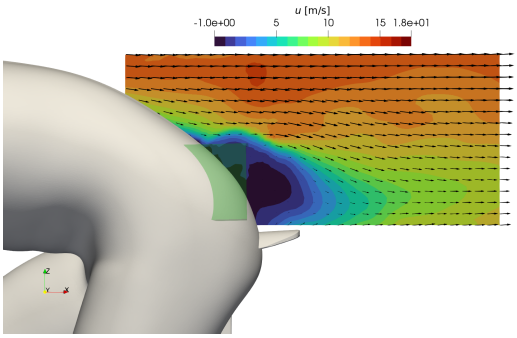

(b) LHS view of the HVC configuration showing streamwise velocity

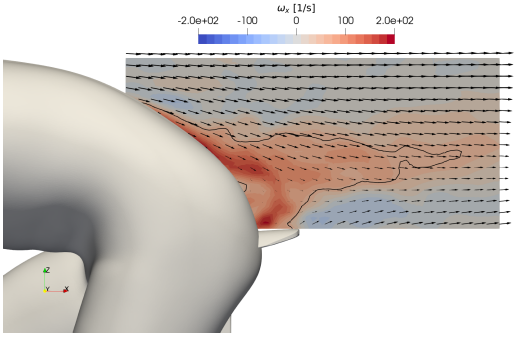

(c) LHS view of the baseline configuration showing streamwise vorticity with a line contour at ω_x = 50 [1/s]

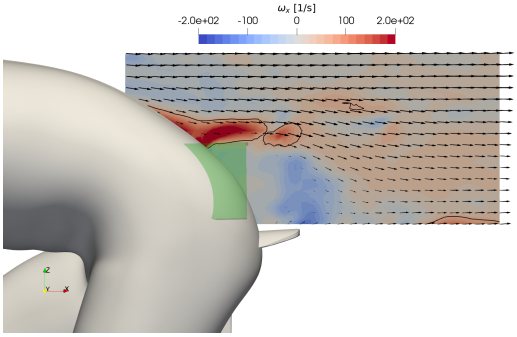

(d) LHS view of the baseline configuration showing streamwise vorticity with a line contour at ω_x = 50 [1/s]

Figure 6.19: Comparison of the streamwise velocity and vorticity between the baseline (left) and HVC (right visualized in transparent green) configuration in a plane 50 mm from the center plane (position C)

6.2.3. The flow topology of the wingsuit

The flow topology measured for the wingsuit configuration is visualized with the Q-criterion and colored by vorticity. The result is shown in Figure 6.20. Similar to the results of the baseline configuration it stands out that the flow structures appear more distributed in the wake of the cyclist. As was discussed, this is expected to be an effect of the bin size and should not affect the conclusions in the comparison of the flow field with the baseline.

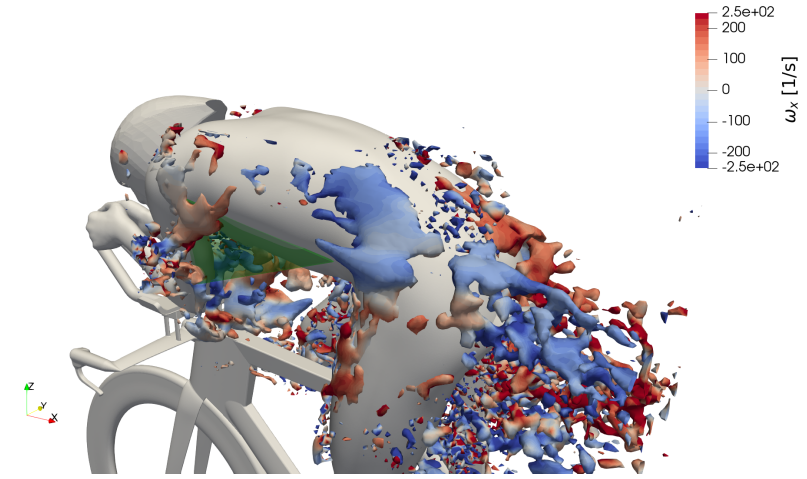

(a) LHS view

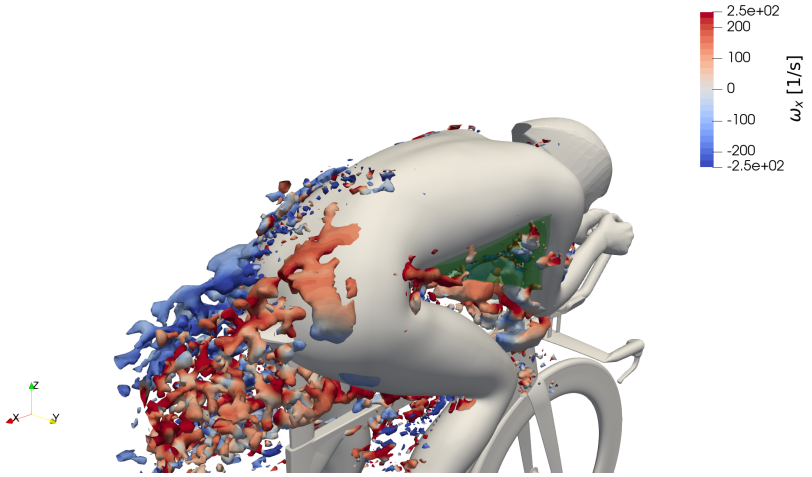

(b) RHS view

Figure 6.20: Wingsuit configuration experimental result showing Q-criterion $(Q = 4000\ [1/s^2])$ coloured by ω_x [1/s] (red counterclockwise and blue clockwise vorticity)

A few key differences stand out when comparing the flow topology with the baseline. First, it can be seen that the outboard elbow vortices have reduced in size with the introduction of the wingsuit. This effect is similar compared to the observations made in the numerical results. The second observation is that the size of the hip vortices has increased and these continue further down into the wake. This effect is comparable to the results discussed in subsection 6.1.3. Interestingly, the numerical and experimental results show similar trends in the variations of the flow topology between the wingsuit and baseline configurations.

To extend the discussion on the changing flow topology the flow field in the wake behind the upper arms is visualized with the streamwise velocity and streamwise vorticity. These results can be found in Figure 6.21.

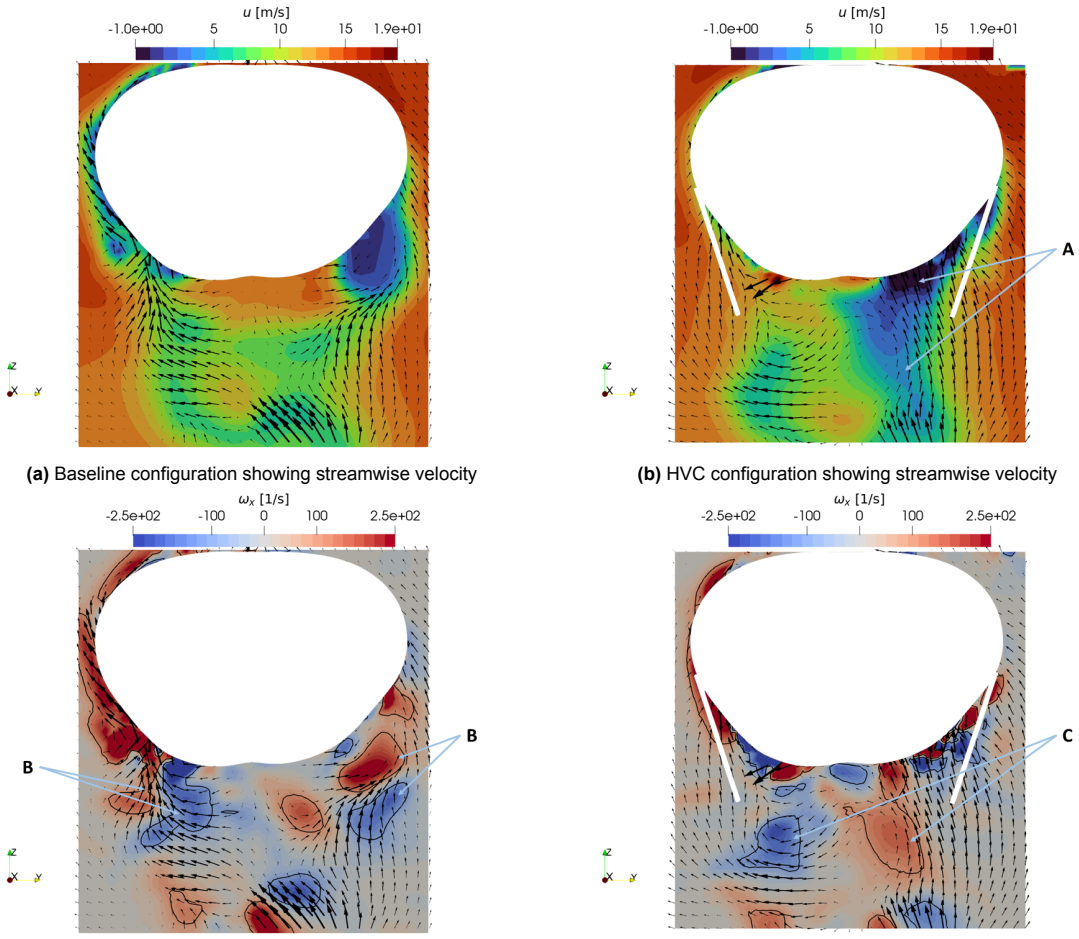

(a) Baseline configuration showing streamwise velocity

(b) HVC configuration showing streamwise velocity

(c) Baseline configuration showing streamwise vorticity with a line contour of $\omega_x = \pm 100[1/s]$

(d) Wingsuit configuration showing streamwise vorticity with a line contour of $\omega_x = \pm 100[1/s]$

Figure 6.21: Comparison of the streamwise velocity and vorticity between the baseline (left) and the wingsuit (right) configurations of a plane behind the upper arms (position A)

These flow visualizations indicate that the wake behind the RHS upper arm has increased for the wingsuit configuration (A). Comparing this against the numerical results a similar change in the flow topology was observed. More importantly, two counter-rotating vortex pairs close to the upper arms in the baseline (B) are reduced for the wingsuit configuration. Only two vortices positioned lower and closer to the centerline (C) remain present for the wingsuit configuration. What is remarkable, is the close correlation of the change in flow topology with the numerical results as was shown in Figure 6.8. A comparison of the change in the flow topology of the numerical results with the experimental results of the wingsuit configuration has been added to Appendix E. This agreement with the numerical results suggests that the reduction of streamwise vorticity behind the upper arm should also lead to a drag reduction in the experimental result.

Further downstream of the model, additional variations in the flow topology are seen. These are visualized at the location of the rear axis with the streamwise velocity and streamwise vorticity in Figure 6.22.

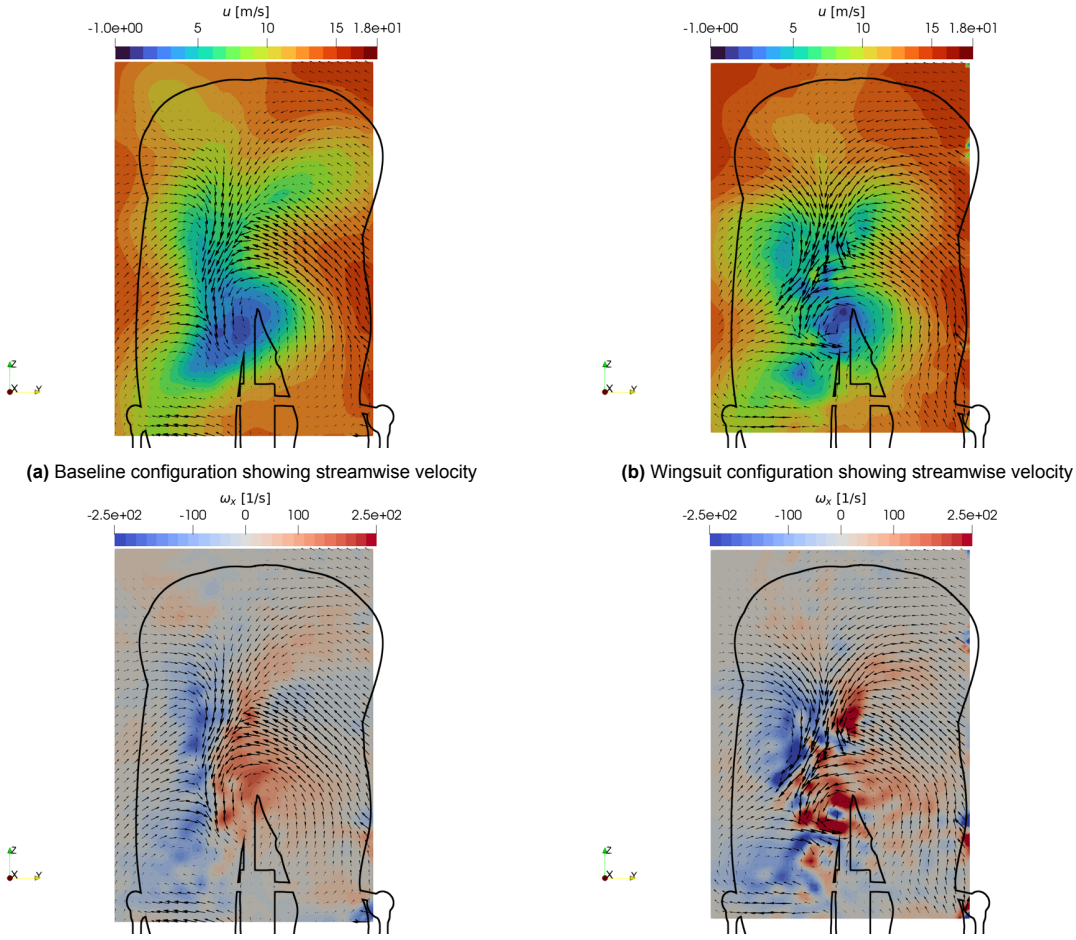

(a) Baseline configuration showing streamwise velocity

(b) Wingsuit configuration showing streamwise velocity

(c) Baseline configuration showing streamwise vorticity

(d) Wingsuit configuration showing streamwise vorticity

Figure 6.22: Comparison of the streamwise velocity and vorticity between the baseline (left) and wingsuit (right) configurations in a plane at the rear axis (position B)

The wind tunnel experiment reveals a trend similar to the outcome of the CFD simulations at this location. First, the upper part of the wake itself, visualized by the streamwise velocity for the baseline and wingsuit configuration in Figure 6.22a and Figure 6.22b respectively, has moved downwards for the wingsuit configuration. The stronger counter-rotating hip vortices increase the downwash affecting the upper part of the wake. The streamwise hip vortices are shown in Figure 6.22c and Figure 6.22d for the baseline and wingsuit configurations respectively. These figures clearly indicate the increased hip vorticity for the wingsuit configuration and indicated by the scaled arrows a larger in-plane velocity between the counter-rotating vortex pair. A similar trend is observed in the numerical results solidifying the working mechanism of the downstream effects of the wingsuit configuration.

The previously discussed observations indicate that the trends between numerical and experimental results are largely in agreement. Next, the balance results will be discussed to investigate how much these changes in the flow topology, measured in the wind tunnel, led to a reduction of the drag.

6.2.4. Force balance results

The drag force of all of the configurations that were discussed in chapter 5 was measured with the force balance. These results will be discussed next.

Overview of the drag reductions

In Figure 6.23 an overview of the drag measurements and the relative difference compared to the baseline is given. More specifically, in Figure 6.23a the drag areas of each of the configurations are shown for a range of velocities, and, in Figure 6.23b the percentage difference compared against the baseline configuration is given.

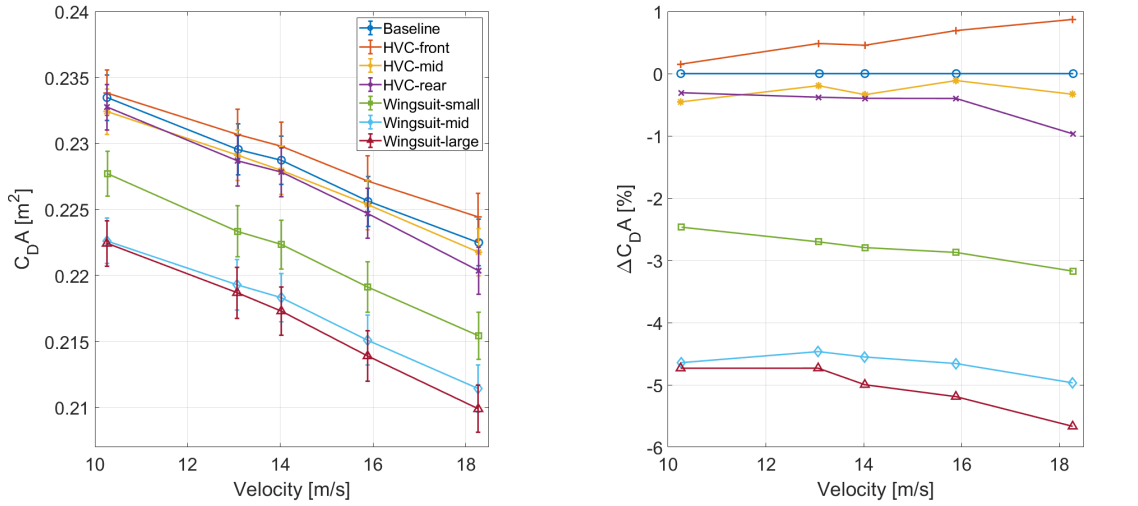

(a) Measured drag area with error bars representing the standard measurement uncertainty

(b) Drag area as percentage difference compared to the baseline

Figure 6.23: Drag measurements for the different configurations. Both graphs share the same legend

The uncertainty of the balance measurements has only been visualized in Figure 5.18 and Figure 6.23a. The balance results which will be discussed next, do share the same uncertainties as discussed in subsection 5.5.2. However, to improve the clarity of the following graphs it was decided to leave out the uncertainty bars. Finally, the drag values and percentage difference measured at 14 m/s, the velocity at which the 3D-PTV measurements were performed, have also been included in Table 6.5.

Table 6.5: $C_D A$ and $\Delta C_D A$ values measured at U_∞ = 14 m/s for the different configurations

Configuration	$C_D A$ [m^2]	$\Delta C_D A$ [%]
Baseline	0.229	0
HVC-front	0.230	+0.44
HVC-mid	0.228	-0.44
HVC-rear	0.228	-0.44
Wingsuit-small	0.222	-3.06
Wingsuit-mid	0.218	-4.80
Wingsuit-large	0.217	-5.24

Interestingly, the drag area measured for the baseline configuration falls well within the range of drag areas discussed by Spoelstra et al., 2019 who provide an analysis of different investigations researching cycling aerodynamics. This suggests that the measured drag area is within the expected range.

Hip Vortex Control

The response of the HVC is relatively small compared to the baseline configuration. Positioning the HVC further upstream results in an increase in drag whereas the other two positions result in a slightly smaller drag area. From the measured drag areas shown in Table 6.5, it can be seen that the HVC-mid and HVC-rear result in a reduction of the drag area of -0.4% suggesting that a more rearward position makes the HVC more effective. However, these results fall within the uncertainty range making it difficult

to construct any valid conclusions on the effectiveness of the HVC on the GCM in the straight-ahead condition.

The reduction in drag, shown in Table 6.5, was smaller than the result found with the numerical simulations shown in Table 6.4. There are a couple of reasons which could be causing this. First, there is a difference in the model and therefore the flow topology which could impact the effectiveness of the HVC. Second, in the numerical evaluation of the HVC, it was found that the sensitivity to the position and size was relatively large. As this model of the HVC has been designed on the numerical model of Tom Dumoulin, it could mean that it is less effective on the GCM as the flow topology and therefore the origin of hip vortices is expected to be different. However, as will be discussed later, it was found that the effectiveness of the HVC increased when it was combined with the wingsuit as well as under crosswind conditions.

Wingsuit

As Table 6.5 indicates, the wingsuit is more effective in reducing drag compared to the HVC. At 14 m/s, a drag reduction between -3.1% and -5.2% was observed depending on the size of the wingsuit. More interestingly, it was found that the difference in drag between the mid and large wingsuit is much smaller compared to the small wingsuit. Hence, we find a reduction in effectiveness from a certain size of the wingsuit when scaled from the shoulder.

From the results shown in Figure 6.23a, it becomes clear that the effectiveness of the wingsuit is only slightly affected by the velocity. Measurements were taken between 10 m/s and 18 m/s. This suggests that a wingsuit could be beneficial for a wide range of velocities. This may be important if, for example, part of a time trial stage includes a climb where the average velocity may be much lower compared to a flat section in the stage.

Effect of the visor on the measured drag

Measurements were performed for the three sizes of the wingsuit without the visor installed. The difference in visor configuration has been explained in subsection 5.2.4. The effect of removing the visor is found to vary between the different sizes of the wingsuit. The results are shown in Figure 6.24.

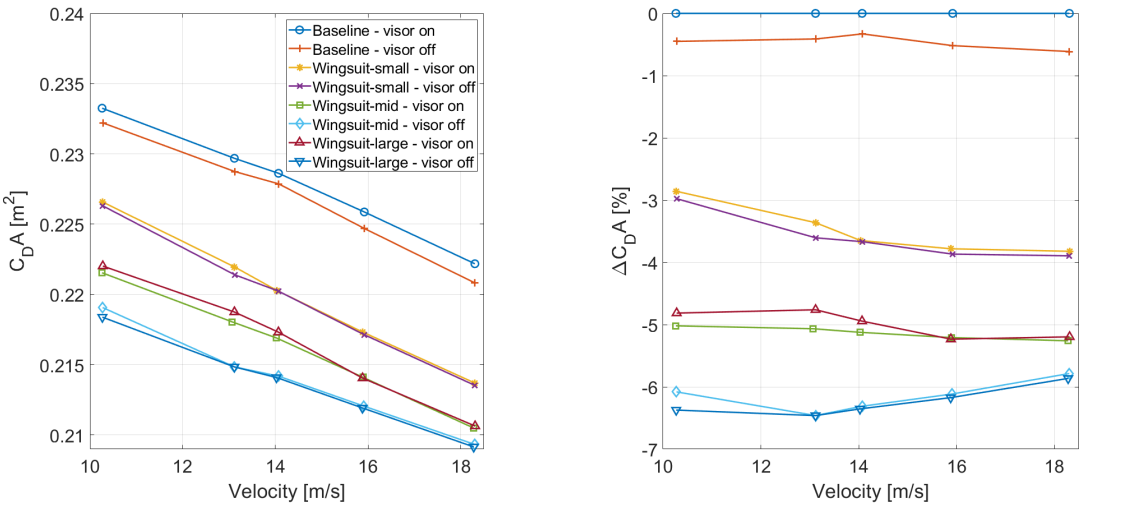

(a) Measured drag area

(b) Drag area as percentage difference compared to the baseline

Figure 6.24: Drag measurements showing the difference for the baseline configuration and wingsuits running with and without the visor installed. Both figures share the same legend

Figure 6.24b shows a small drag reduction for the visor-off condition on the baseline configuration.

However, these results fall within the uncertainty range challenging any conclusions made on the aerodynamic effect of removing the visor for the baseline configuration. Furthermore, the drag response was found to be too small for the HVC configurations as well and is therefore not included in Figure 6.24. Additionally, the wingsuit-small was found to be unresponsive to the visor-off condition compared to having the visor installed. However, when running the medium and large wingsuits the effectiveness of both configurations increases by nearly 1% point. This means at 14 m/s a total drag reduction of more than -6% compared to the baseline with the visor is observed.

The drag reduction of the wingsuit-mid configuration was found to correlate well with the numerical results which, as was shown in Table 6.4, also resulted in a -6% drag reduction for the similarly sized wingsuit. Furthermore, the numerical model of Tom Dumoulin was also simulated without a visor. It is expected that the visor changes the flow topology between the arms and therefore has an effect on the drag of the wingsuit. However, at this moment no information on the flow field is available for both the visor-on and visor-off configurations making it difficult to comment on the working mechanisms.

Combination of the HVC and wingsuit

To investigate the maximum observed drag saving, combinations of the HVC and wingsuit were studied. When combining the HVC-mid and the wingsuit-mid more than -7% in drag savings is measured at 14 m/s as can be seen in Figure 6.25. For these measurements, it was decided to remove the visor as the wingsuit was found to be more effective without this installed.

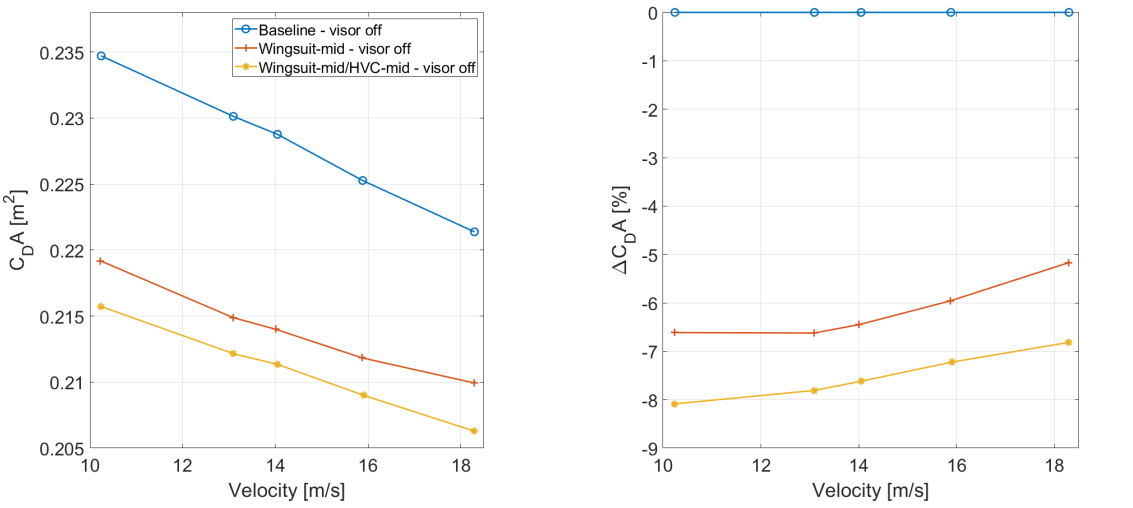

(a) Measured drag area

(b) Drag area as percentage difference compared to the baseline

Figure 6.25: Drag measurements showing the difference for the baseline configuration with the combination of the HVC with the wingsuit. Both figures share the same legend

What stands out is the increased effectiveness of the HVC when combining this with the wingsuit. Table 6.5 shows that the HVC on its own is only responsible for a marginal reduction in drag compared to the baseline which falls within the uncertainty range. However, compared to the wingsuit configuration the drag area reduces with a full 1% point after the HVC is added. The improved effectiveness is expected to be related to the increased hip vorticity for the wingsuit configuration observed in both the numerical and experimental results. The reduction of these larger structures with the HVC is expected to have a larger impact on the drag. This could be a verification of the discussed flow mechanisms, where it becomes more profitable to reduce hip vorticity as they gain strength. More interestingly, Spoelstra et al., 2019 mention that the hip vortices of cyclists increase in strength for the upright position suggesting that the HVC could be more effective for a cyclist in the upright position (Figure 2.2a).

Lycra wingsuit

In an attempt to further realize the wingsuit as a drag reduction method in TT stages, a model made from lycra was also tested in the wind tunnel. The experimental setup of the lycra wingsuit was discussed in subsection 5.2.6. Lycra is often used as a base material for cycling jerseys and shorts. The medium-sized wingsuit was replicated in size with the lycra wingsuit when it was put under tension. The measured drag area can be found in Figure 6.26.

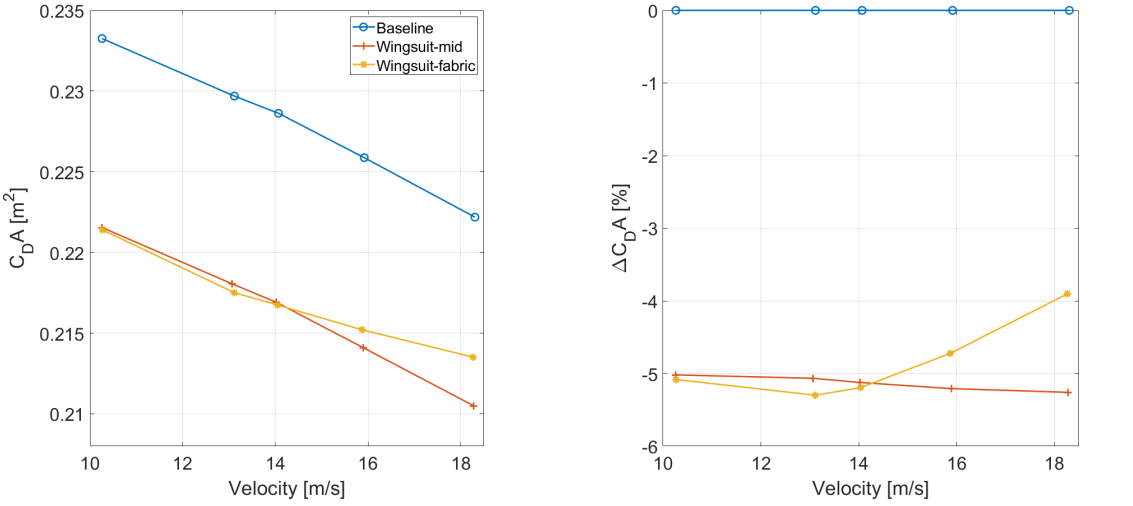

(a) Measured drag area

(b) Drag area as percentage difference compared to the baseline

Figure 6.26: Drag measurements showing the difference between the baseline configuration and the mid wingsuit made from a solid material and lycra. All configurations are with the visor installed. Both figures share the same legend

The results show that the drag reduction compared to the baseline is very similar to the results obtained with the medium-sized wingsuit made from a solid material. However, above 15 m/s the effectiveness of the lycra wingsuit starts to reduce compared to the solid wingsuit. During the experiment, at these larger velocities the trailing edge started to vibrate. This slight increase in drag between the lycra and the solid wingsuit is likely due to these trailing edge vibrations at higher velocities. Further research on the integration of the wingsuit in a cycling jersey and further stretching of the fabric should help minimize the trailing edge vibrations which should increase the effectiveness.

6.2.5. Effect of crosswind

Since the objective is to find drag reductions that can be used in practice the effectiveness for a range of crosswind angles was measured. Three configurations were tested including the baseline configuration, HVC-mid, and wingsuit-mid. The respective drag reduction methods were chosen based on their effectiveness in the straight-ahead condition and were also examined with 3D-PTV. An overview of the force area in the bike's direction of travel can be found in Figure 6.27. The reason to keep both the HVC and wingsuit configurations with their respective baseline in different figures is that these have both been measured in different measurement sessions. Hence, small differences have been observed between the two baselines. Comparing the results of the HVC and wingsuit to the baseline from the same session is expected to be more accurate as was discussed in subsection 5.4.1.

These results show that both the baseline, HVC, and wingsuit configurations show an asymmetric response, which is due to the asymmetric leg position. Furthermore, we find that the HVC can reduce the drag more effectively at larger crosswind angles. However, to understand the reason behind this improved effectiveness more information on the flow topology is required.

Compared to the HVC, the reduction in drag area was found to be slightly larger for the wingsuit for

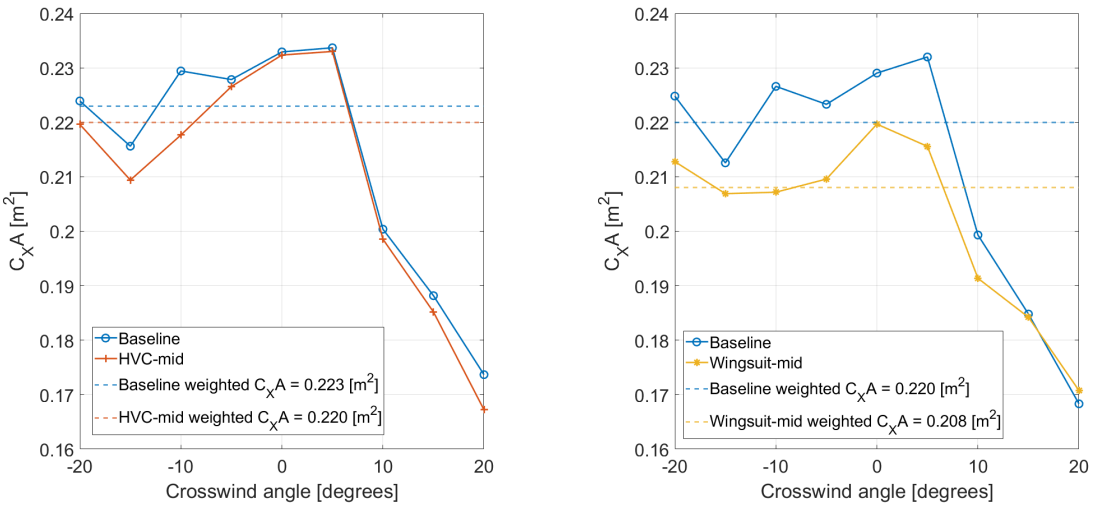

(a) HVC configuration compared to the baseline

(b) Wingsuit configuration compared to the baseline

Figure 6.27: Drag measurements for the wingsuit and HVC configuration at $U_\infty = 14$ m/s for crosswind conditions. The weighted drag area for each configuration has been included in the graphs

a range of crosswind conditions as is shown in Figure 6.28. The results show that both the HVC and wingsuit are effective in reducing the drag for a range of crosswind angles similar to what CFD had suggested. More interestingly, when considering the weighted drag area of the HVC we find a drag reduction of -1.35% which is larger than the reduction observed for just the straight-ahead condition. The reduction in weighted drag area for the wingsuit-mid was -5.45%.

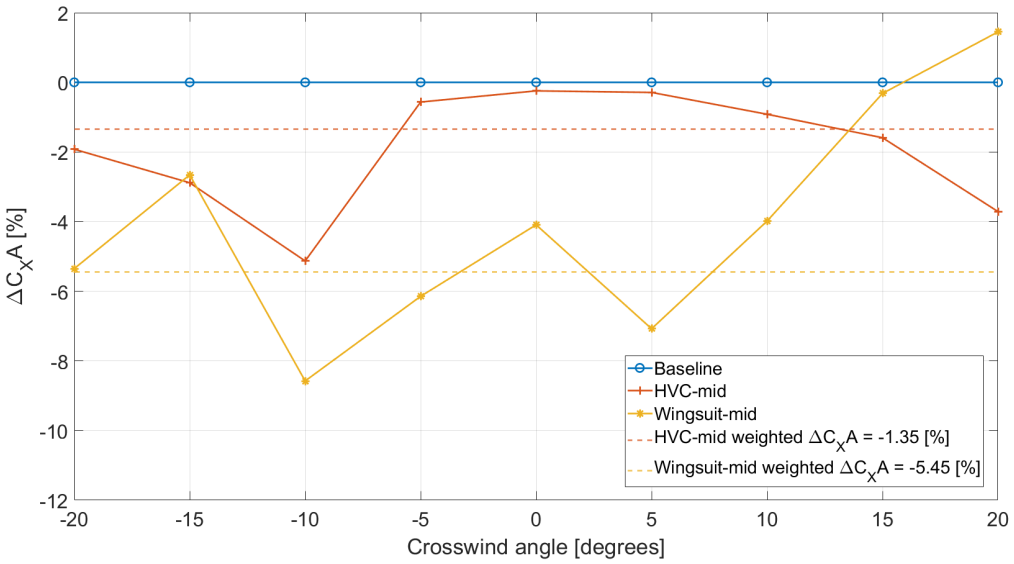

Figure 6.28: Relative difference in drag area for each configuration compared to its respective baseline at $U_\infty = 14$ m/s. The relative weighted drag reductions have been included in the graph

The weighted drag areas for the HVC and wingsuit are expected to be a more realistic representation of the expected drag reduction as explained by Barry, 2018 compared to the discussed results in the straight-ahead condition. The weighted drag areas are summarized in Table 6.6.

For the different configurations, the major variations observed in the flow topology have been discussed.

Table 6.6: Weighted $\Delta C_X A$ compared against the baseline

Configuration	Weighted $\Delta C_X A$ [%]
Baseline	0
HVC	-1.35
Wingsuit	-5.45

A few of the discrepancies in the flow topology stand out. To conclude this chapter, three observations on the manipulation of the flow topology between the numerical and experimental results are summarized which are expected to be the main contributors to the drag reductions.

1. The HVC is successful in promoting separation on the lower back of the cyclist and reducing the presence of counter-rotating hip vortices. This leads to an increase in the surface pressure on the lower back of the cyclist and a reduction of the drag.
2. The wingsuit is effective in reducing counter-rotating vortex pairs emanating from the upper arms. The numerical results revealed a pressure increase on the surface of the upper arms resulting in a drag reduction.
3. The downstream effect of the wingsuit results in a stronger counter-rotating hip vortex pair. However, the HVC is more effective in reducing these stronger vortices suggesting a positive relation between the hip vortex strength and the effectiveness of the HVC.

Finally, the effect of the measured drag reductions in the context of a TT stage in the Tour de France is not inconsequential. For example, for the HVC and wingsuit configurations a -1.35% and -5.45% reduction in weighted drag area would result in finishing a 40 km TT stage 13 and 53 seconds earlier respectively following the example discussed in Appendix A. This result indicates the potential of the manipulation of the 3D flow topology in the wake of a cyclist to achieve a drag reduction.

7

Conclusions and Recommendations

In the introduction, an example illustrated the significance of a few percentages of drag reduction for a cyclist in a time trial position. The previous chapter examined the potential of the HVC and wingsuit and showed how these can contribute to achieving a drag reduction. The following chapter discusses the conclusions and recommendations for these results. Conclusions for both drag reduction methods are provided together with conclusions on the methodology of the development process. The chapter concludes with recommendations and an outlook on future research.

7.1. Conclusions

The following section focuses on the conclusions following from the results discussed in the previous chapter. A broader perspective on the aerodynamic effect of the HVC and wingsuit is given.

7.1.1. Cyclist drag reduction through the manipulation of the 3D flow topology

Both the HVC and wingsuit are effective in achieving a reduction in drag through the manipulation of the local flow topology. The weighted drag area, evaluated experimentally, of the HVC configuration compared to the baseline is reduced by -1.35%. Furthermore, the weighted drag area of the wingsuit configuration compared to the baseline is reduced by -5.45%. As explained, a cyclist would finish a 40 km time trial stage 13 and 53 seconds earlier while wearing the HVC and wingsuit respectively. A 53-second time reduction is the difference between the first and fifth place in the 20th stage of the 2022 Tour de France.

HVC

The objective of this thesis is to investigate the potential of achieving a drag reduction through the manipulation of the near-body 3D flow topology. The results indicate that careful manipulation of the streamwise vortices can contribute to a reduction of the drag. By positioning the HVC on the curved back of a cyclist, the generation of the hip vortices is reduced. Numerical simulations suggest that the reduction of the trailing hip vortices and increase in wake result in an increase in surface pressure on the lower back of the cyclist. This is expected to contribute to the drag reduction. This mechanism is analogous to the results of Beaudoin and Aider, 2008 and Aider et al., 2010 who discuss the manipulation of the 3D flow topology in the wake of an Ahmed body.

Both the numerical and experimental results suggest that the strength of the hip vortices can be reduced by separating the flow on the lower back of the cyclist. Furthermore, the numerical results have indi-

cated that the position of the wake evolves more symmetrical making this comparable to the observed flow topology for the symmetric leg position as discussed by Crouch et al., 2014.

The experimental results indicate that by combining the HVC with the wingsuit, the effectiveness of the HVC is increased. Both the numerical and experimental results suggest that the wingsuit affects the hip vortices, indicating that their strength increases. It is expected that the increased hip vorticity, as a result of the wingsuit, makes the HVC more effective. This poses an interesting opportunity which has yet to be tested. Other bike positions, where the cyclist is positioned more upright, have been found to generate stronger hip vortices (Spoelstra et al., 2019). Hence, this suggests that the HVC may also be effective for those bike positions for which a stronger counter-rotating hip vortex pair exists.

Wingsuit

The wingsuit is more effective in reducing the drag compared to the HVC, which is suggested both numerically and experimentally. Furthermore, a larger wingsuit is more effective up to a certain size after which the increased effectiveness reduces. The flow topology around the upper arms changes with the wingsuit installed. The outboard vortices reduce in strength considerably, the inboard vortices reduce in strength as well and move further inboard and, the wake of the upper arms slightly increases. The numerical results show a reduction in circulation behind the upper arms and a wake deficit analysis indicates that the drag reduction is related mainly to a decrease in the pressure deficit compared with the baseline. As a result, on the upper arms, a large pressure increase is observed in the numerical simulations responsible for the majority of the drag reduction.

A non-rigid version of the wingsuit, fabricated from lycra, was tested in the wind tunnel. This material, commonly used as a material for cycling clothes, is found to be as effective as the solid wingsuit up to 15 m/s. For a higher freestream velocity, the trailing edge starts vibrating resulting in a small reduction in effectiveness. However, this experiment indicates that a wingsuit, when installed under enough tension, can easily be incorporated into existing cycling jerseys.

Drag reductions through the reduction of streamwise vorticity

The numerical results of the wingsuit configuration provide us with evidence that the trailing streamwise vortices of the upper arms have a strong effect on the local pressure distribution. By overlaying the position of the vortices emanating from the upper arms with the pressure contours an agreement between the low-pressure regions and vortex cores is observed. Furthermore, the wake deficit analysis indicated that the reduction of the pressure deficit is the largest contributor to the drag reduction while correlating with a reduction in circulation. More generally, as Aider et al., 2010 suggested, it is beneficial to reduce the amount of longitudinal vorticity while keeping the wake size to a minimum to reduce the drag of bluff bodies.

The work presented in this thesis suggests, however, that the expansion of the wake and reduction of counter-rotating vortex pairs can be traded and must be balanced to reduce the drag. It was shown that careful expansion of the wake can reduce streamwise vorticity and contribute to a drag reduction. If done successfully, the reduction of streamwise vortices can outweigh the drag contribution of the expanded wake and result in a net reduction of the drag. Furthermore, as Aider et al., 2010 highlighted, if these vortices are counter-rotating an additional contribution to the drag is expected because of the local pressure reduction as a result of the stream of in-plane velocity in between the vortex pair. This strengthens the reasoning to reduce counter-rotating vortex pairs in the wake of bluff bodies and therefore their prominent contribution to the total drag.

Achieving drag reductions for bluff bodies, like a cyclist, is a complex problem. The flow field must be carefully mapped to evaluate the 3D flow topology. Then, streamwise vortices - especially counter-rotating vortex pairs - should be minimized by reducing the formation at their origin as was done with the HVC. Vortices emanating from the upper arms can be reduced with a wingsuit resulting in a local pressure increase and a noticeable drag reduction. After all, combining the wingsuit and HVC has been shown to be the most effective in reducing drag as the systems complement each other.

7.1.2. Effect on the drag of the clip-on visor on the KASK Mistral time trial helmet

The results have shown that the clip-on visor on the KASK Mistral TT helmet has a negative effect on both the baseline configuration as well as the larger wingsuit configurations. For the baseline configuration with the visor installed, the drag area increases by a couple of tenths of a percent depending on the velocity. However, as was mentioned before, this result falls within the uncertainty range challenging any valid conclusion.

Nonetheless, with the wingsuit installed, it was found that operating the helmet without the visor results in a drag reduction of over a full percent point compared to having the visor installed. At this stage, it is difficult to comment on the working mechanism because of the absence of flow field information between the two configurations.

7.1.3. Coupling of CFD and 3D PTV for aerodynamic development

The proposed methodology for the development of drag reduction methods and the evaluation of the aerodynamic mechanisms are found to become more effective through the use of both numerical and experimental simulations. Although both have limitations in their accuracy, each contributes to the overall understanding of the workings of the drag reduction method.

The numerical simulations provide a complete overview of the flow field. For the initial development of the drag reduction methods, this is important to understand the reasons for the observed variations in drag. Furthermore, CFD provides a method to quickly evaluate many variations of the HVC and wingsuit. Moreover, before testing these designs in the wind tunnel the numerical simulations had already indicated what areas of the flow field are expected to change. Since experimental resources are generally limited, it is more effective to investigate only the parts of the volume that are expected to change and contribute to the research objective.

To verify the effectiveness and working mechanisms of the drag reductions an experimental study is preferred together with a visualization of the 3D flow field. However, instead of testing a broad range of designs, only the most promising were manufactured as a wind tunnel model. The entire development of the drag reduction methods would not have been practical to be realized with just a wind tunnel examination as it is too expensive and time-consuming to operate. Nonetheless, the experimental simulations provide the required certainty to verify the effectiveness of the proposed drag-reduction methods solidifying the conclusions made.

7.2. Recommendations and outlook

The recommendations and future outlook are discussed next. Recommendations on the continuation of the research on the 3D flow topology in cycling are provided. The presented drag reductions are currently illegal by the UCI regulations. However, other sports such as triathlon allow for more complex bike designs and have fewer regulations on the suit design. Hence, a discussion is presented on the possibilities of the presented drag reductions in other sports.

7.2.1. Further research on the 3D flow topology of a cyclist

As was concluded, the reduction of the streamwise vortices behind the upper arms and lower back has been found an effective method to reduce the drag of a cyclist. For this thesis, the manipulation of the upper arm, elbow, and hip vortices has been studied. However, the complex flow topology of a cyclist has many more structures which, when reduced, may also contribute to a reduction in drag. It is therefore recommended to investigate the effect of, for example, the trailing vortices of the helmet, bike, and moving legs to investigate other areas where further reductions can be achieved.

Among these flow structures, other bike positions have shown a variation in the wake topology com-

pared to the presented results of the time trial position. Hence, it is recommended to also evaluate the potential of the presented drag reduction methods for other bike positions like the handlebar position. An increased hip vorticity resulted in an increase in the effectiveness of the HVC. Hence, compared to the time trial position this would suggest that the handlebar position could also benefit from the reduction of the hip vortices using for example the HVC.

7.2.2. Leg positions and on-site experiments

The results discussed so far, focus on the effectiveness of the drag reductions in the high-drag position. Hence, the effectiveness of the HVC and wingsuit for the low-drag position is still to be evaluated. Nonetheless, Crouch et al., 2014 describe the presence of hip vortices and vortices emanating from upper arms for the low drag position as well. Therefore, it is expected that although the effectiveness of both drag reduction methods for the low-drag position may vary, the working mechanisms should remain equivalent.

Nonetheless, to extend the understanding of the workings of the drag reduction methods it is recommended to investigate the HVC and wingsuit for a pedaling cyclist in a numerical study (Griffith et al., 2019) or in an on-site environment using PIV measurements (Spoelstra et al., 2019). Both methods allow for the evaluation of the flow field to different degrees. The latter will provide more certainty in the realization of the drag reductions in a real-life environment.

7.2.3. Legalistation and integration of the drag reduction methods

At this moment, both the HVC and wingsuit would be regarded as illegal in an official competition regulated by the UCI. However, a couple of changes could be made that perhaps could help with the legalization of these methods in the future. The HVC's working mechanism focuses on promoting separation on the lower back of the cyclist. As Aider et al., 2010 have shown, instead of using a spoiler to achieve this, vortex generators can effectively reduce the streamwise vortices and drag. Perhaps it is possible to replicate this effect on the lower back of the cyclist being integrated into the cycling jersey.

A wingsuit made from lycra was investigated and was found to be effective in reducing drag. The arm position of a TT cyclist allows for such a design to be integrated into existing cyclist jerseys or skinsuits. Important is that the fabric is put under the right amount of tension when the cyclist is in the TT position to keep the trailing edge from vibrating. This configuration would, however, be illegal in competitions regulated by the UCI. Nonetheless, these results could perhaps be an invitation to a discussion on the relaxation of current suit regulations allowing the continuation of innovation in the cycling sport.

Finally, triathlon allows for more freedom in the application of aerodynamic optimization compared to regular cycling competitions where the bike must be UCI-legal. Examples include the use of more aerodynamic bike frames and the placement of bottle cages behind the saddle. Furthermore, where the UCI obligates a cyclist to wear a jersey that follows the cyclist's body, in triathlon similar regulations are not defined. Hence, this should allow an athlete to compete with a wingsuit.

7.2.4. Drag reductions in other sports

On a final note, cycling is not the only sport where an athlete would benefit from a drag reduction. Like cycling, streamwise counter-rotating vortices are reported in the wake of, for example, speed skaters (Terra et al., 2023). Analogous to cycling, in speed skating the aerodynamic drag can be up to 80% of the total resistance (Gibertini and Grassi, 2008). The wake topology is, however, expected to vary much more compared to cycling because of the changing posture of a speed skater. Nonetheless, promoting separation at the locations of the origin of these vortices could result in the reduction of the drag. As the margins between first and second place are often small already a slight reduction in drag could benefit an athlete in becoming a world champion.

Bibliography

Agüera, N., Cafiero, G., Astarita, T., & Discetti, S. (2016). Ensemble 3d ptv for high resolution turbulent statistics. *Measurement Science and Technology*, *27*. https://doi.org/10.1088/0957-0233/27/12/124011

Aider, J. L., Beaudoin, J. F., & Wesfreid, J. E. (2010). Drag and lift reduction of a 3d bluff-body using active vortex generators. *Experiments in Fluids*, *48*, 771–789. https://doi.org/10.1007/s00348-009-0770-y

Alons, H. (2008). *Ojf external balance* [NLR-CR-2008-695]. Dutch Aerospace Laboratory.

Barry, N. (2018). A new method for analysing the effect of environmental wind on real world aerodynamic performance in cycling, 211. https://doi.org/10.3390/proceedings2060211

Barry, N., Burton, D., Sheridan, J., Thompson, M., & Brown, N. A. (2016). Flow field interactions between two tandem cyclists. *Experiments in Fluids*, *57*. https://doi.org/10.1007/s00348-016-2273-y

Beaudoin, J. F., & Aider, J. L. (2008). Drag and lift reduction of a 3d bluff body using flaps. *Experiments in Fluids*, *44*, 491–501. https://doi.org/10.1007/s00348-007-0392-1

Blocken, B., van Druenen, T., Toparlar, Y., & Andrianne, T. (2019). Cfd analysis of an exceptional cyclist sprint position. *Sports Engineering*, *22*. https://doi.org/10.1007/s12283-019-0304-7

Bosbach, J., Kühn, M., & Wagner, C. (2009). Large scale particle image velocimetry with helium filled soap bubbles. *Experiments in Fluids*, *46*. https://doi.org/10.1007/s00348-008-0579-0

Burrus, C. S., Barreto, J. A., & Selesnick, I. W. (1994). Iterative reweighted least-squares design of fir filters. *IEEE Transactions on Signal Processing*, *42*(11), 2926–2936.

Caridi, G. C. A., Ragni, D., Sciacchitano, A., & Scarano, F. (2016). Hfsb-seeding for large-scale tomographic piv in wind tunnels. *Experiments in Fluids*, *57*. https://doi.org/10.1007/s00348-016-2277-7

Crouch, T. N., Burton, D., Brown, N. A., Thompson, M. C., & Sheridan, J. (2014). Flow topology in the wake of a cyclist and its effect on aerodynamic drag. *Journal of Fluid Mechanics*, *748*. https://doi.org/10.1017/jfm.2013.678

Crouch, T. N., Burton, D., Thompson, M. C., Brown, N. A., & Sheridan, J. (2016). Dynamic leg-motion and its effect on the aerodynamic performance of cyclists. *Journal of Fluids and Structures*, *65*. https://doi.org/10.1016/j.jfluidstructs.2016.05.007

Defraeye, T., Blocken, B., Koninckx, E., Hespel, P., & Carmeliet, J. (2010). Computational fluid dynamics analysis of cyclist aerodynamics: Performance of different turbulence-modelling and boundary-layer modelling approaches. *Journal of Biomechanics*, *43*, 2281–2287. https://doi.org/10.1016/j.jbiomech.2010.04.038

Elsinga, G. E., Scarano, F., Wieneke, B., & Oudheusden, B. W. V. (2006). Tomographic particle image velocimetry. *Experiments in Fluids*, *41*. https://doi.org/10.1007/s00348-006-0212-z

Giaquinta, D. (2018). *The flow topology of the ahmed body in cross-wind an experimental investigation by means of robotic volumetric piv*.

Gibertini, G., & Grassi, D. (2008). *Cycling aerodynamics*. https://doi.org/10.1007/978-3-211-89297-8_3

Grappe, F., Candau, R., Belli, A., & Rouillon, J. D. (1997). Aerodynamic drag in field cycling with special reference to the obree's position. *Ergonomics*, *40*. https://doi.org/10.1080/001401397187388

Griffith, M. D., Crouch, T., Thompson, M. C., Burton, D., Sheridan, J., & Brown, N. A. (2014). Computational fluid dynamics study of the effect of leg position on cyclist aerodynamic drag. *Journal of Fluids Engineering, Transactions of the ASME*, *136*. https://doi.org/10.1115/1.4027428

Griffith, M. D., Crouch, T. N., Burton, D., Sheridan, J., Brown, N. A., & Thompson, M. C. (2019). A numerical model for the time-dependent wake of a pedalling cyclist. *Proceedings of the Institution of Mechanical Engineers, Part P: Journal of Sports Engineering and Technology*, *233*. https://doi.org/10.1177/1754337119858434

Horn, B. K. P. (1987). Closed-form solution of absolute orientation using unit quaternions. *Josa a*, *4*(4), 629–642.

Hucho, W.-H., & Sovran, G. (1993). *Aerodynamics of road vehicles*. www.annualreviews.org

Hwang, B. G., Lee, S., Lee, E. J., Kim, J. J., Kim, M., You, D., & Lee, S. J. (2016). Reduction of drag in heavy vehicles with two different types of advanced side skirts. *Journal of Wind Engineering and Industrial Aerodynamics*, *155*, 36–46. https://doi.org/10.1016/j.jweia.2016.04.009

Javadi, A. (2022). Aerodynamic study of the pedalling of a cyclist with a transitional hybrid rans–les turbulence model. *Flow, Turbulence and Combustion*, *108*, 717–738. https://doi.org/10.1007/s10494-021-00297-4

Jeong, J., & Hussain, F. (1995). On the identification of a vortex. *Journal of Fluid Mechanics*, *285*, 69–94. https://doi.org/10.1017/S0022112095000462

Jux, C., Sciacchitano, A., & Scarano, F. (2020). Flow pressure evaluation on generic surfaces by robotic volumetric ptv. *Measurement Science and Technology*, *31*. https://doi.org/10.1088/1361-6501/ab8f46

Jux, C. (2017). *Robotic volumetric particle tracking velocimetry by coaxial imaging and illumination*.

Jux, C., Sciacchitano, A., Schneiders, J. F., & Scarano, F. (2018). Robotic volumetric piv of a full-scale cyclist. *Experiments in Fluids*, *59*. https://doi.org/10.1007/s00348-018-2524-1

Kyle, C. R., & Burke, E. (1984). Improving the racing bicycle. *Mechanical Engineering*, *106*.

Lignarolo, L. E., Ragni, D., Krishnaswami, C., Chen, Q., Ferreira, C. J. S., & van Bussel, G. J. (2014). Experimental analysis of the wake of a horizontal-axis wind-turbine model. *Renewable Energy*, *70*, 31–46. https://doi.org/10.1016/j.renene.2014.01.020

Lukes, R. A., Chin, S. B., & Haake, S. J. (2005). The understanding and development of cycling aerodynamics. *Sports engineering*, *8*, 59–74.

Menter, F. R., Kuntz, M., & Langtry, R. (2003). Ten years of industrial experience with the sst turbulence model. *Turbulence, heat and mass transfer*, *4*(1), 625–632.

Mercker, E., & Wiedemann, J. (1996). On the correction of interference effects in open jet wind tunnels. *SAE transactions*, 795–809.

Raffel, M., Willert, C. E., Scarano, F., Kähler, C. J., Wereley, S. T., & Kompenhans, J. (2018). *Particle image velocimetry a practical guide third edition* (3th ed.). Springer.

Scarano, F. (2013a). *Tomographic piv: Principles and practice*. https://doi.org/10.1088/0957-0233/24/1/012001

Scarano, F. (2013b). *Experimental aerodynamics* [1 edition, course reader, Flow Measurement Techniques (AE4-180)]. Delft University of Technology.

Scarano, F., Jux, C., & Sciacchitano, A. (2021). Recent advancements towards large-scale flow diagnostics by robotic piv. *Fluid Dynamics Research*, *53*. https://doi.org/10.1088/1873-7005/abe034

Schanz, D., Gesemann, S., & Schröder, A. (2016). Shake-the-box: Lagrangian particle tracking at high particle image densities. *Experiments in Fluids*, *57*. https://doi.org/10.1007/s00348-016-2157-1

Schanz, D., Gesemann, S., Schröder, A., Wieneke, B., & Novara, M. (2013). Non-uniform optical transfer functions in particle imaging: Calibration and application to tomographic reconstruction. *Measurement Science and Technology*, *24*. https://doi.org/10.1088/0957-0233/24/2/024009

Schneiders, J. F., Scarano, F., Jux, C., & Sciacchitano, A. (2018). Coaxial volumetric velocimetry. *Measurement Science and Technology*, *29*. https://doi.org/10.1088/1361-6501/aab07d

Sciacchitano & Giaquinta. (2019). Investigation of the ahmed body cross-wind flow topology by robotic volumetric piv, 311–320. https://doi.org/10.18726/2019_3

Soloff, S. M., Adrian, R. J., & Liu, Z.-C. (1997). Distortion compensation for generalized stereoscopic particle image velocimetry. *Measurement science and technology*, *8*(12), 1441.

Spoelstra, A., de Martino Norante, L., Terra, W., Sciacchitano, A., & Scarano, F. (2019). On-site cycling drag analysis with the ring of fire. *Experiments in Fluids*, *60*. https://doi.org/10.1007/s00348-019-2737-y

Spoelstra, A., Mahalingesh, N., & Sciacchitano, A. (2020). Drafting effect in cycling: On-site aerodynamic investigation by the 'ring of fire', 113. https://doi.org/10.3390/proceedings2020049113

Szodrai, F. (2020). *Quantitative analysis of drag reduction methods for blunt shaped automobiles*. https://doi.org/10.3390/app10124313

Terra, W., Sciacchitano, A., & Scarano, F. (2016a). Drag analysis from piv data in speed sports. *Procedia Engineering*, *147*, 50–55. https://doi.org/10.1016/j.proeng.2016.06.188

Terra, W., Sciacchitano, A., & Scarano, F. (2016b). *Evaluation of aerodynamic drag of a full-scale cyclist model by large-scale tomographic-piv*. APA.

Terra, W., Sciacchitano, A., & Scarano, F. (2020). Cyclist reynolds number effects and drag crisis distribution. *Journal of Wind Engineering and Industrial Aerodynamics*, *200*. https://doi.org/10.1016/j.jweia.2020.104143

Terra, W., Sciacchitano, A., & Shah, Y. H. (2019). Aerodynamic drag determination of a full-scale cyclist mannequin from large-scale ptv measurements. *Experiments in Fluids*, *60*. https://doi.org/10.1007/s00348-019-2677-6

Terra, W., Spoelstra, A., & Sciacchitano, A. (2023). Aerodynamic benefits of drafting in speed skating: Estimates from in-field skater's wakes and wind tunnel measurements. *Journal of Wind Engineering and Industrial Aerodynamics*, *233*. https://doi.org/10.1016/j.jweia.2023.105329

Vino, G., Watkins, S., Mousley, P., Watmuff, J., & Prasad, S. (2005). Flow structures in the near-wake of the ahmed model. *Journal of Fluids and Structures*, *20*, 673–695. https://doi.org/10.1016/j.jfluidstructs.2005.03.006

Vloemans, S. (2022). *Cyclist mannequin for aerodynamic research*.

Wieneke, B. (2008). Volume self-calibration for 3d particle image velocimetry. *Experiments in Fluids*, *45*. https://doi.org/10.1007/s00348-008-0521-5

Wieneke, B. (2013). Iterative reconstruction of volumetric particle distribution. *Measurement Science and Technology*, *24*. https://doi.org/10.1088/0957-0233/24/2/024008

A

Appendix: Time Effects of a Drag Reduction in Cycling

To provide more context on the benefits of aerodynamic efficiency in cycling the following example is provided. For the second time-trial stage in the 2022 Tour de France, a 40.7 km distance had to be covered. The winner, Wout van Aert, managed to achieve an average speed of 50 km/h [1]. To demonstrate how a 2% reduction in drag can change the outcome of the race we will use van Aert's average velocity as an example. For this example, we will assume that the total power (P_T) provided by the cyclist remains constant given a reduction in drag area. From this, we can then compute the reduced time required to complete the TT stage.

To compute P_{aero} Equation A.1 is used. Here, D is the drag force (as defined in Equation 2.1), and U is the average velocity from the TT stage.

$$P_{\text{aero}} = D \cdot U \tag{A.1}$$

The total power is defined as $P_T = P_f + P_{\text{aero}}$ where P_f is the power used to overcome the rolling resistance and mechanical losses. For now, we assume that the dependence of P_f with the velocity is very small. Hence, when we assume P_T to remain constant for a reduction in the drag we find that P_{aero} has to be constant.

We use Equation A.1 and Equation 2.1 to set up a power balance to compute the new velocity (U_2) when the drag area is reduced by 2%. The result is shown in Equation A.2.

$$\begin{aligned} P_{\text{aero}} &= \frac{1}{2}\rho U_1^2 C_D A \cdot U_1 = \frac{1}{2}\rho U_2^2 0.98 C_D A \cdot U_2 \\ &= U_1^3 = U_2^3 0.98 \end{aligned} \tag{A.2}$$

From this analysis we can compute U_2 resulting in $U_2 = U_1/\sqrt[3]{0.98}$. When we use the average velocity of $U_1 = 50.0$ km/h we find that $U_2 = 50.34$ km/h. This increase in average speed results in finishing the stage 20 seconds earlier.

[1] https://www.procyclingstats.com/race/tour-de-france/2022/stage-20

B

Appendix: HVC and Wingsuit Dimensions

The following appendix will provide the dimensions of the HVC and the wingsuit. First, the dimensions of the HVC are shown. Then, the dimensions of the dimensions of the wingsuit are provided.

B.1. HVC dimensions

An overview of the definitions of the dimensions of the HVC mid can be found in Figure B.1. The corresponding dimensions are shown in Table B.1.

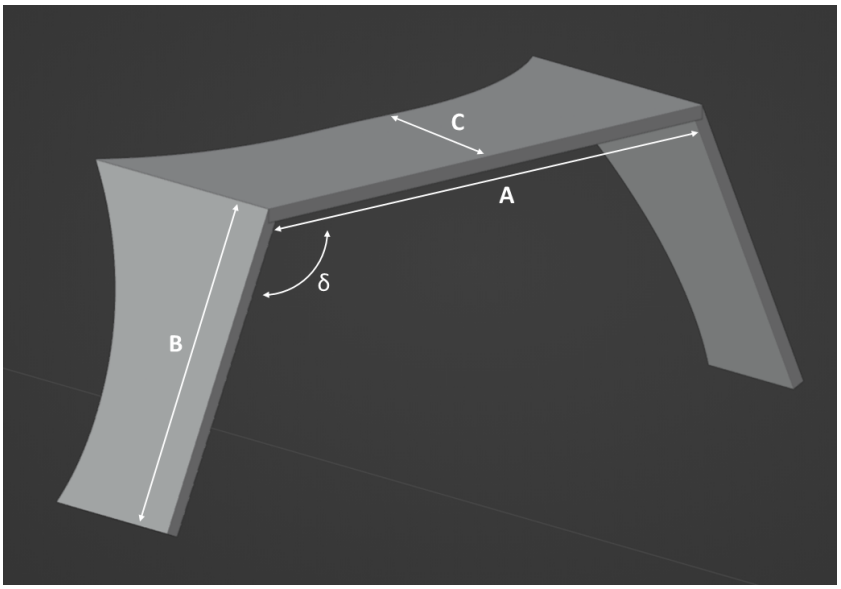

Figure B.1: Definitions of the dimensions for the HVC

The definition of the streamwise position of the trailing edge for each HVC can be seen in Figure B.2.

The corresponding lengths can be found in Table B.1.

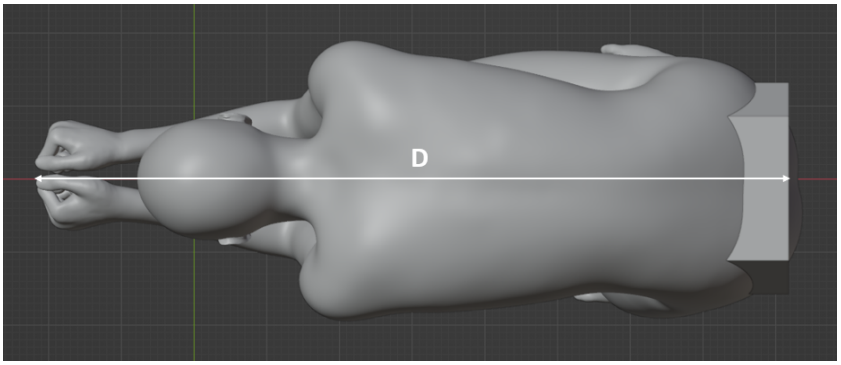

Figure B.2: Definition of the streamwise position of the trailing edge of the HVC

Table B.1: Dimensions of the HVC mid

Name	Symbol	Dimension	Unit
Width horizontal plate	A	20	[cm]
Width angled plate	B	11	[cm]
Length middle of horizontal plate	C	6	[cm]
Streamwise position HVC	D	0.98/1.03/1.09 (front/mid/rear)	[m]
Angle between plates	δ	114	[°]

B.2. Wingsuit dimensions

An overview of the definitions of the dimensions of the wingsuit is given in Figure B.3.

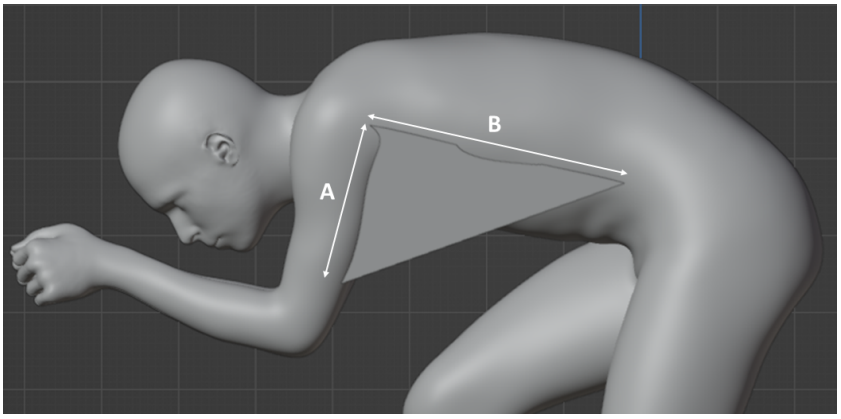

Figure B.3: Definitions of dimensions of the wingsuit

The dimensions for all three wingsuits can be found in Table B.2.

Table B.2: Dimensions of the wingsuit

Name	Symbol	Wingsuit small	Wingsuit mid	Wingsuit Large	Unit
Height	A	16	20	26	[cm]
Length	B	28	33	36	[cm]

C

Appendix: Addendum Numerical Results

This appendix provides additional flow field results. Comparisons between the different configurations and the baseline of the flow field topology are provided. The same comparison of the flow topology for a crosswind condition is also highlighted.

C.1. Comparison of the 3D flow topology

The following section shows a comparison of the flow field visualized by the Q-criterion and colored with the streamwise vorticity. Both the HVC and wingsuit results are compared against the flow field of the baseline configuration. The main differences between the configurations are discussed in chapter 6.

C.1.1. Comparison of flow the flow topology of the baseline with the HVC

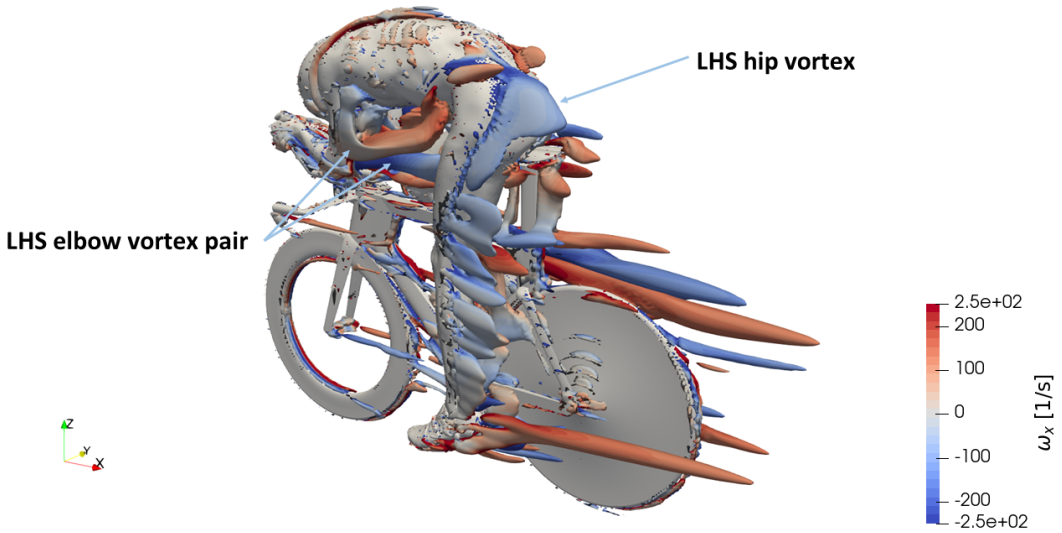

(a) LHS view of the baseline configuration

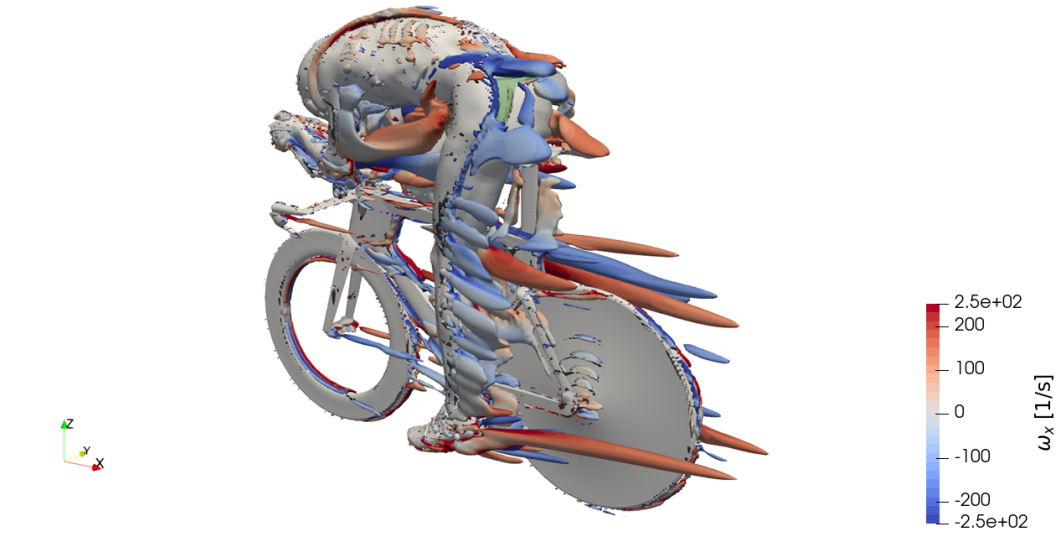

(b) LHS view of the HVC configuration (in transparent green)

Figure C.1: CFD result showing Q-criterion ($Q = 4000\ [1/s^2]$) coloured by ω_x [1/s] (red counterclockwise and blue clockwise vorticity)

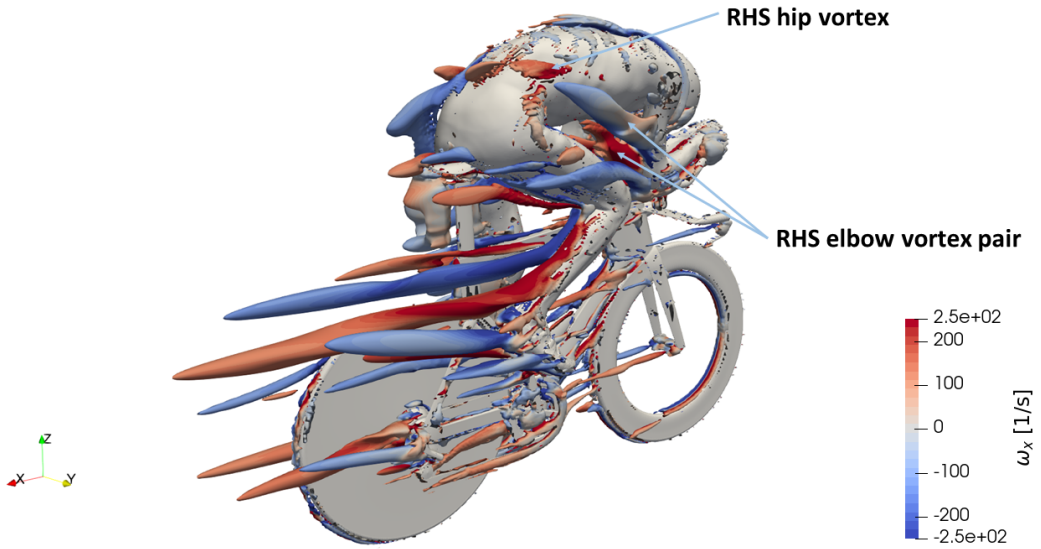

(a) RHS view of the baseline configuration

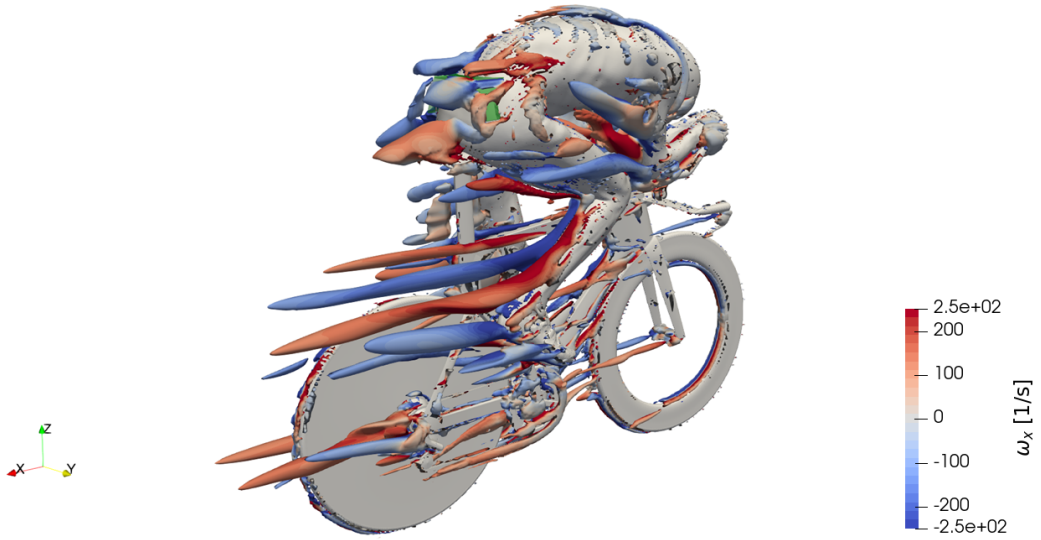

(b) RHS view of the HVC configuration (in transparent green)

Figure C.2: CFD result showing Q-criterion ($Q = 4000\ [1/s^2]$) coloured by ω_x [1/s] (red counterclockwise and blue clockwise vorticity)

C.1.2. Comparison of the flow topology of the baseline with the wingsuit

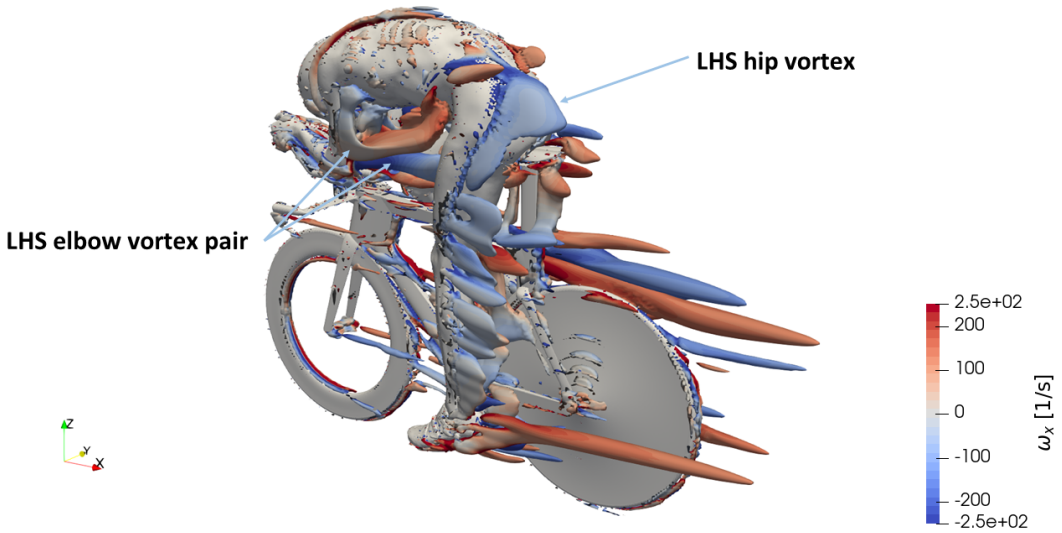

(a) LHS view of the baseline configuration

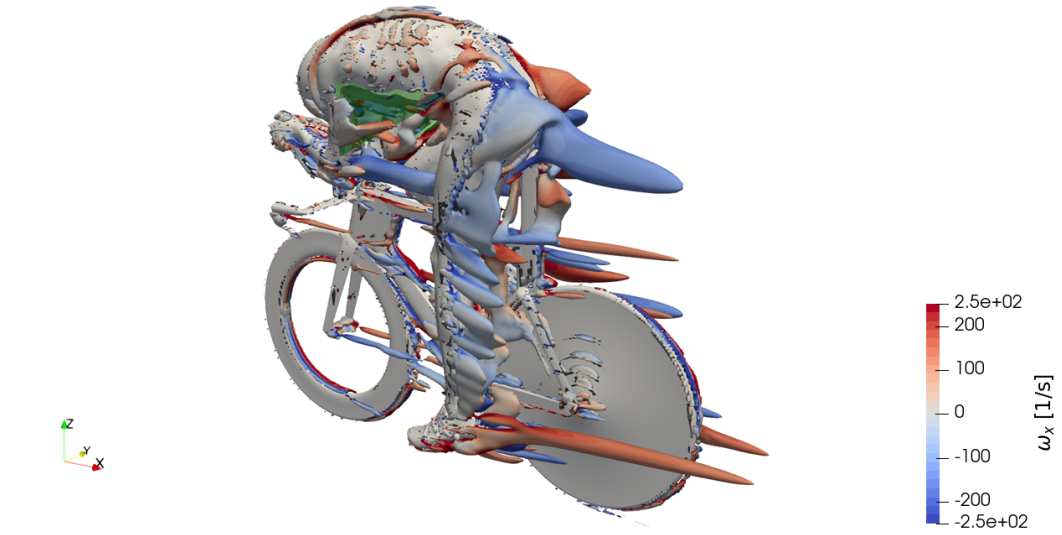

(b) LHS view of the wingsuit configuration (in transparent green)

Figure C.3: CFD result showing Q-criterion ($Q = 4000\ [1/s^2]$) coloured by ω_x [1/s] (red counterclockwise and blue clockwise vorticity)

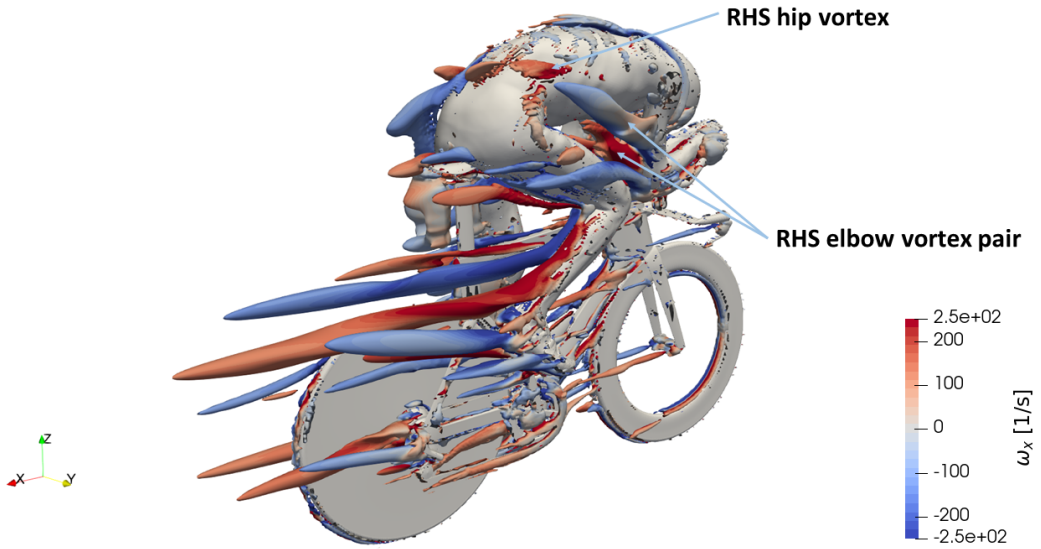

(a) RHS view of the baseline configuration

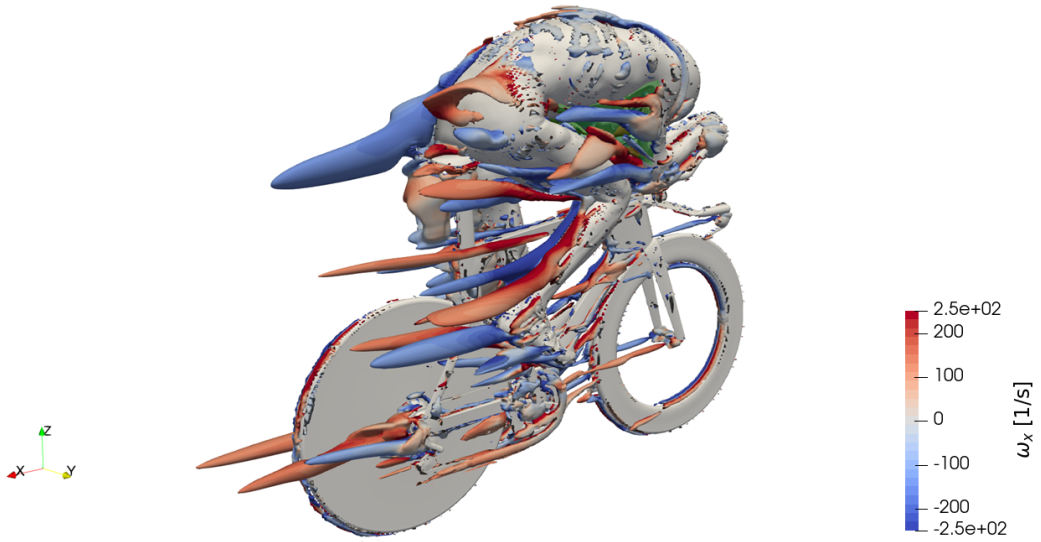

(b) RHS view of the wingsuit configuration (in transparent green)

Figure C.4: CFD result showing Q-criterion ($Q = 4000\ [1/s^2]$) coloured by ω_x [1/s] (red counterclockwise and blue clockwise vorticity)

C.2. Crosswind

More results of each configuration for the crosswind conditions are provided. Figure C.5 shows an overview of the side force coefficient and indicates that for both the HVC and wingsuit configurations the side force only slightly increases. Hence, it is expected that the cyclist will not experience any large changes in the lateral stability.

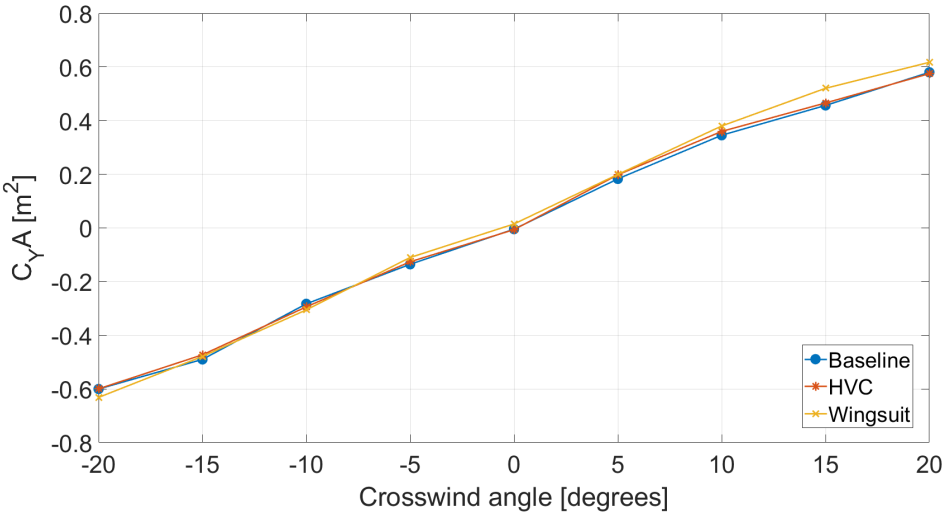

(a) Side force coefficient

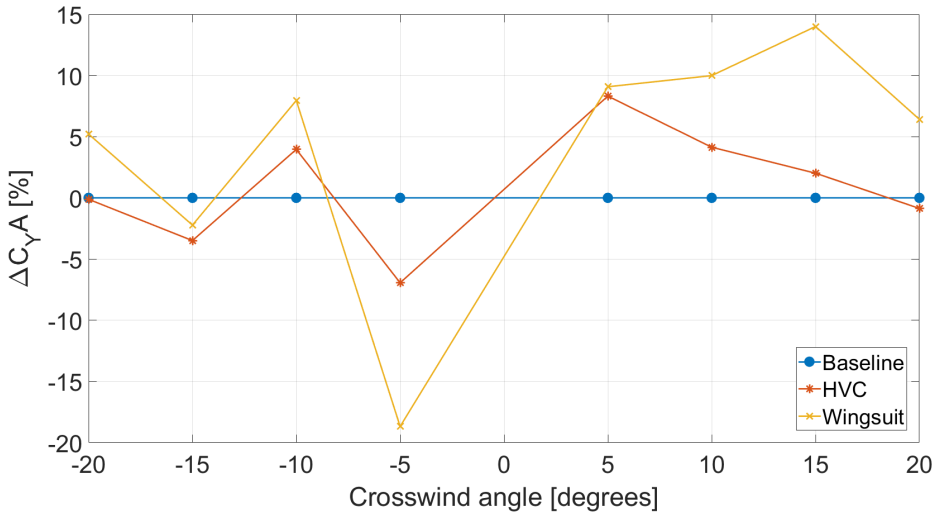

(b) Delta side force coefficient compared against the baseline. The result for 0 degrees crosswind has been left out to improve the clarity of the graph

Figure C.5: Comparison of the side force coefficient measured in CFD

Figure C.6, Figure C.7 and Figure C.8 show the flow topology for the baseline, HVC and wingsuit configurations at -15° crosswind respectively. The differences in the flow topology between the configurations show similar trends as have been discussed in chapter 6 for the straight-ahead condition. However, as no additional information on the flow topology for a cyclist in crosswind is available no further conclusions will be made on the variations in the flow topology. It is recommended to further investigate the flow topology for crosswind conditions to validate the results.

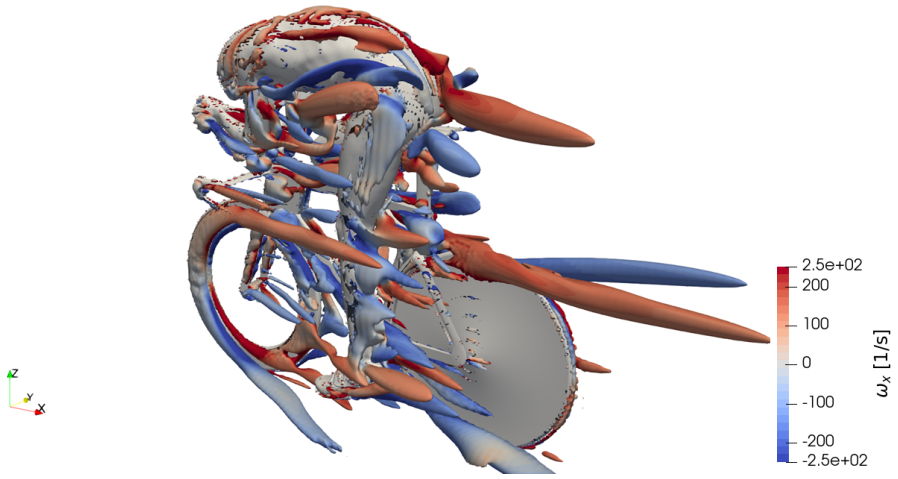

(a) Baseline configuration

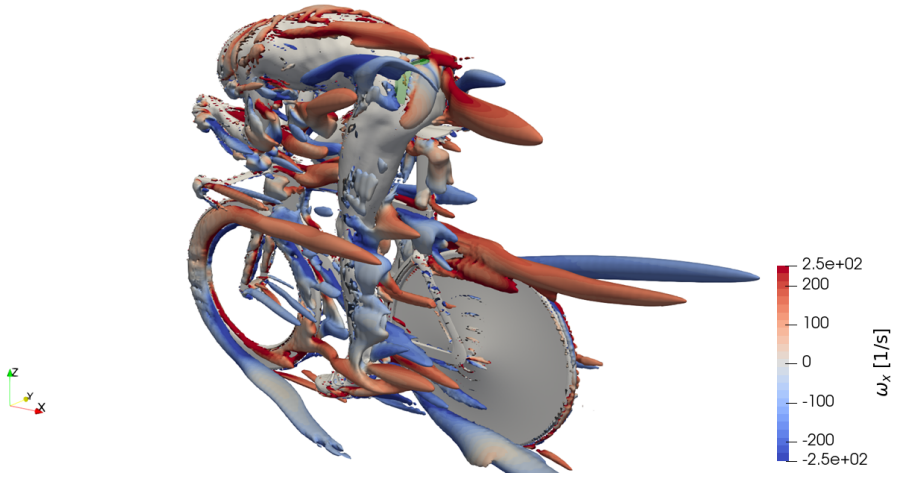

(b) HVC (in transparent green) configuration

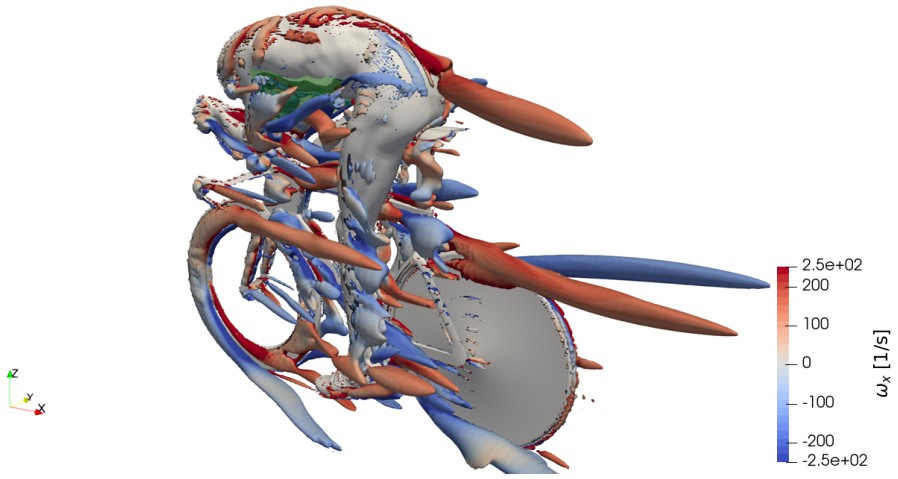

(c) Wingsuit (in transparent green) configuration

Figure C.6: Comparison of the flow topology at -15° crosswind showing Q-criterion ($Q = 4000\ [1/s^2]$) coloured by ω_x [1/s] (red counterclockwise and blue clockwise vorticity)

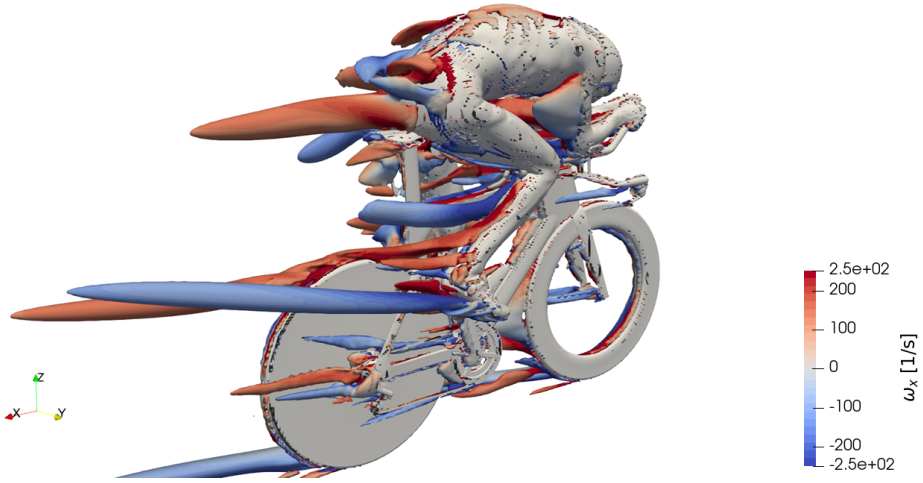

(a) Baseline configuration

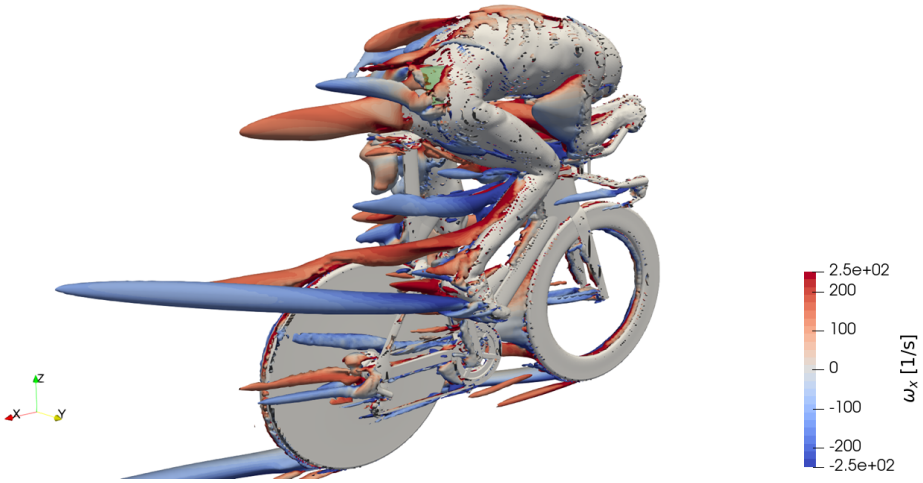

(b) HVC (in transparent green) configuration

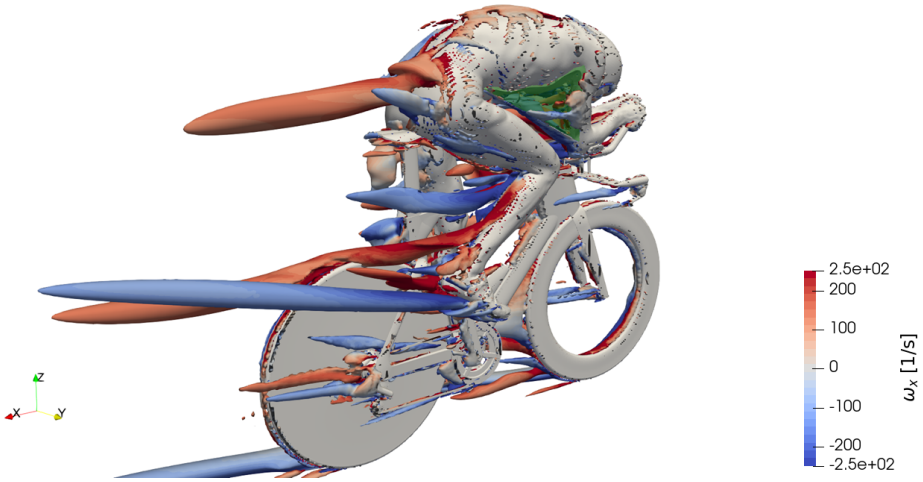

(c) Wingsuit (in transparent green) configuration

Figure C.7: Comparison of the flow topology at -15° crosswind showing Q-criterion ($Q = 4000\ [1/s^2]$) coloured by ω_x [1/s] (red counterclockwise and blue clockwise vorticity)

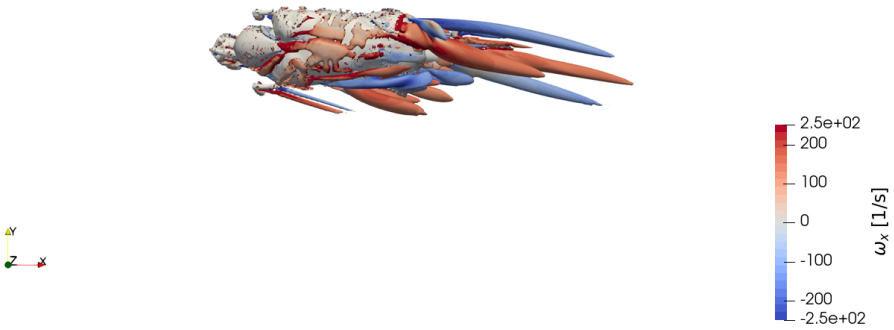

(a) Baseline configuration

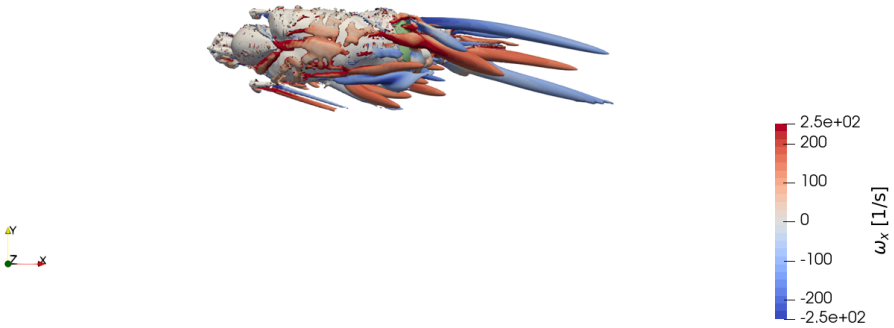

(b) HVC (in transparent green) configuration

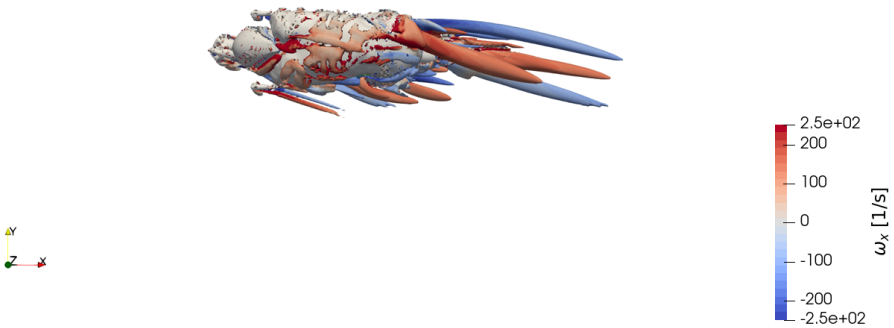

(c) Wingsuit (in transparent green) configuration

Figure C.8: Comparison of the flow topology at -15° crosswind showing Q-criterion ($Q = 4000\ [1/s^2]$) coloured by ω_x [1/s] (red counterclockwise and blue clockwise vorticity)

D

Appendix: Addendum Experimental Results

This appendix provides additional results of the experimental simulation. The side force coefficient is shown below which is measured against a baseline from the same wind tunnel session. Similar as to the numerical results no large variations in the side force have been measured and are therefore expected to not cause any large lateral instabilities.

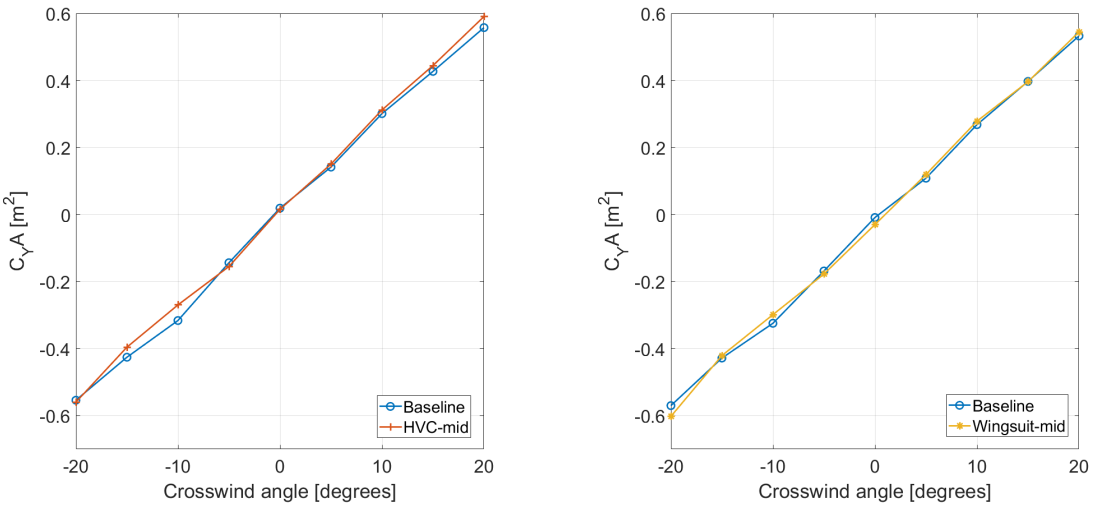

(a) HVC configuration compared to the baseline

(b) Wingsuit configuration compared to the baseline

Figure D.1: Side force measurements for the wingsuit and HVC configuration at $u_\infty = 14$ m/s for crosswind conditions

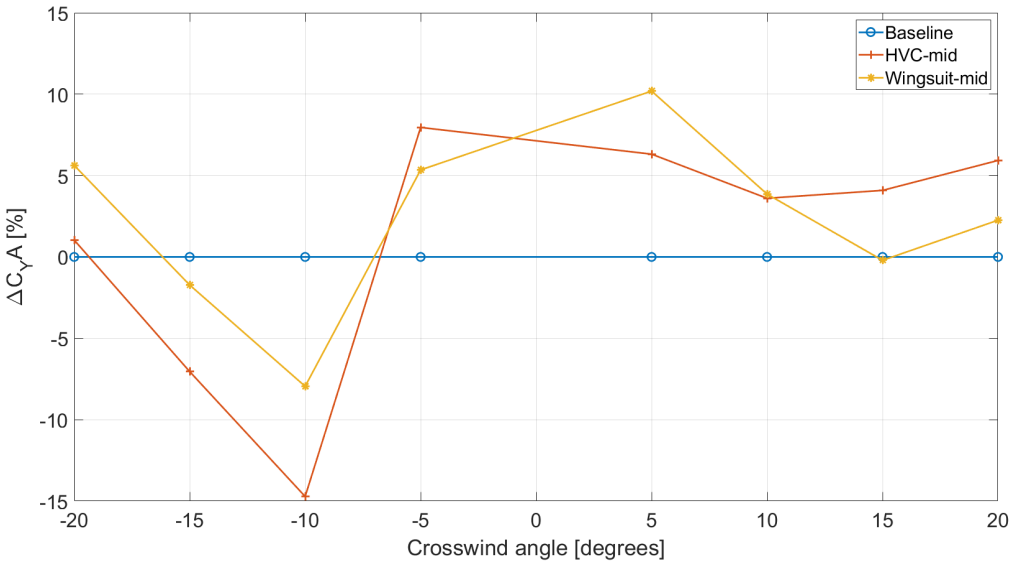

Figure D.2: Relative difference in side force compared with the baseline measured in the wind tunnel. The result for 0 degrees crosswind has been left out to improve the clarity of the graph

E

Appendix: Comparison of the Trends Between the Numerical and Experimental Simulations

The following appendix shows variations in the flow topology between different configurations and compares these flow field discrepancies between the numerical and experimental results. The results below only compare the wingsuit configuration with the baseline configuration because of the smaller data set of the HVC.

E.1. Wingsuit

The results in Figure E.1 show the trends in the variation of the flow topology between the numerical and experimental results. In the baseline configuration, two vortex pairs emanating from the upper arms were observed in both the numerical and experimental results (A). The wingsuit configuration shows a reduction of the strength of both vortex pairs and indicates that the inboard vortex is still present (B). A similar trend between the numerical and experimental results is observed strengthening the physicality of the working mechanism.

In Figure E.2 a comparison between the numerical and experimental results of the streamwise velocity at the rear axis is shown. The results indicate that both the numerical and experimental results indicate a similar trend where the height of the wake is shifted down in the wingsuit configuration. This is expected to be an effect of the increased hip vorticity producing a stronger downwash component. The similarity in trends between both visualization methods solidifies the physicality of the underlying mechanism.

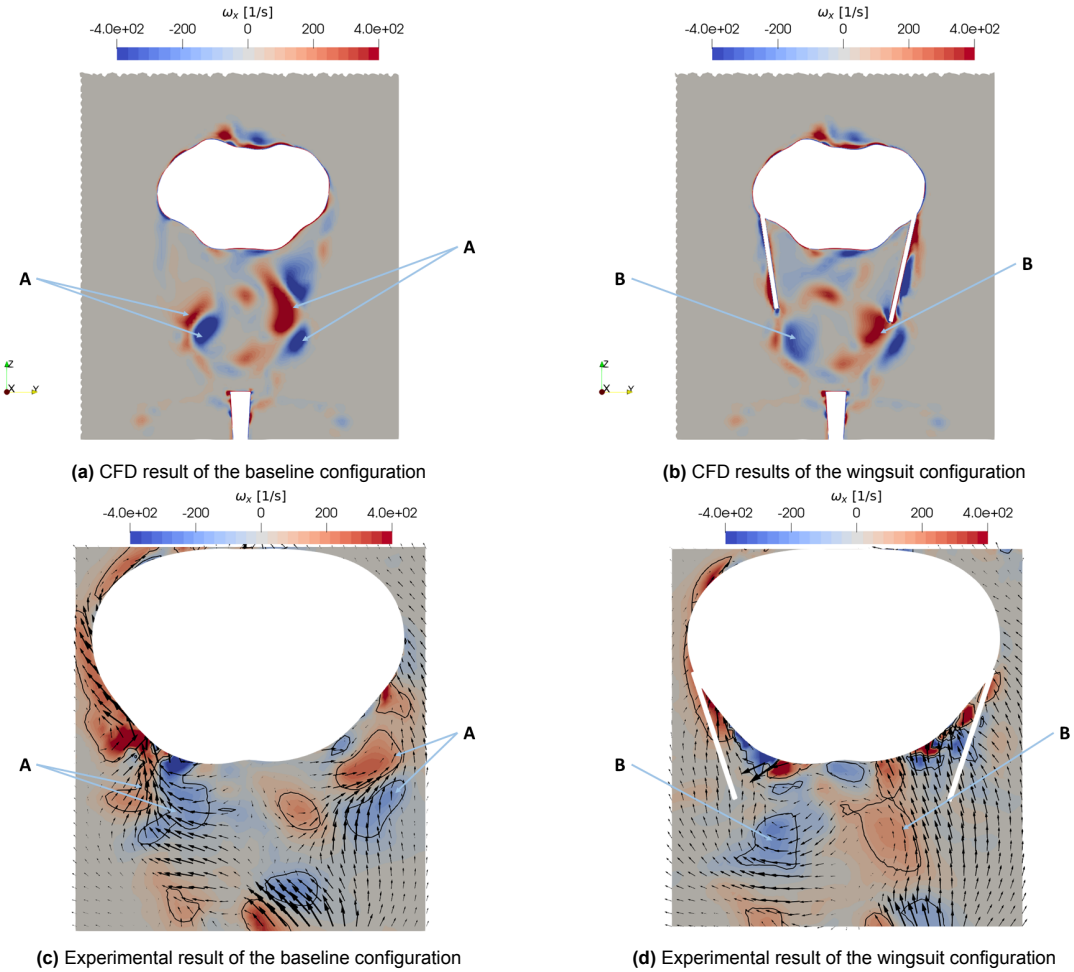

(a) CFD result of the baseline configuration

(b) CFD results of the wingsuit configuration

(c) Experimental result of the baseline configuration

(d) Experimental result of the wingsuit configuration

Figure E.1: Comparison of the streamwise vorticity between the baseline (left) and wingsuit (right) configurations in a plane behind the upper arms. A line contour of $\omega_x = 100$ [1/s] is included in the experimental results (bottom)

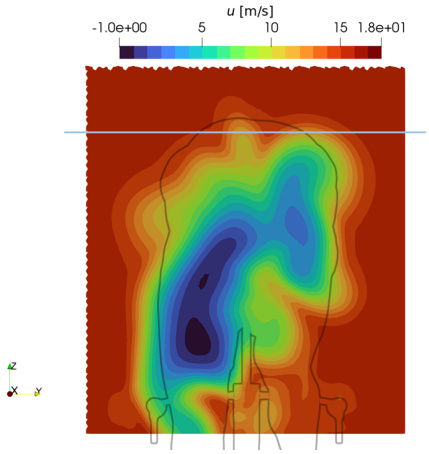

(a) CFD result of the baseline configuration

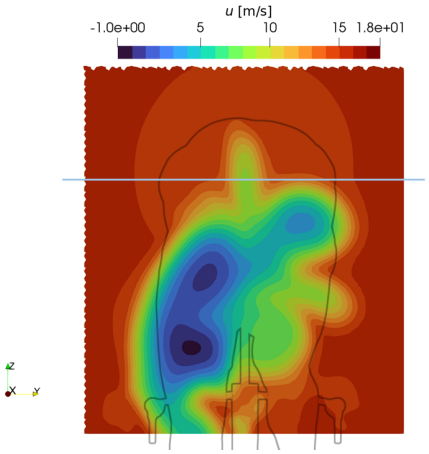

(b) CFD results of the wingsuit configuration

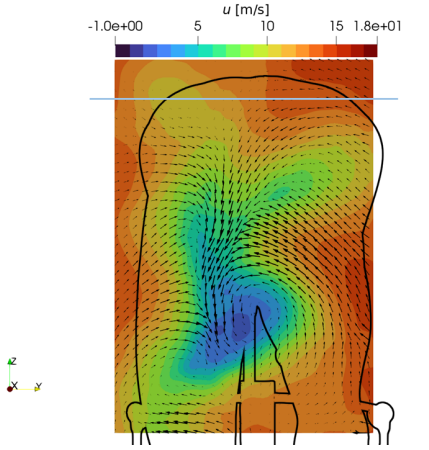

(c) Experimental result of the baseline configuration

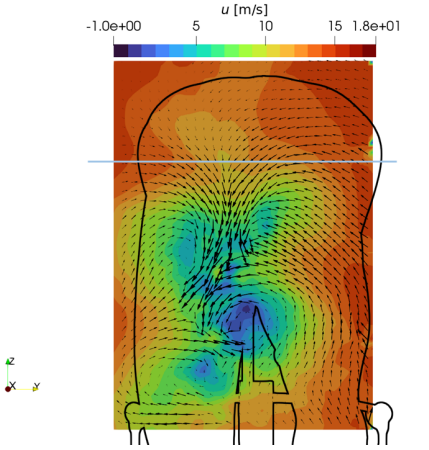

(d) Experimental result of the wingsuit configuration

Figure E.2: Comparison of the streamwise velocity between the baseline (left) and wingsuit (right) configurations in a plane at the rear axis. A horizontal line indicating the height of the top of the wake has been added showing the trend between both configurations